Hybrid Materials Based on Carbon Nanotubes and Graphene: Synthesis, Interfacial Processes, and Applications in Chemical Sensing

by

Mengning Ding

B.S., Nanjing University, 2007

Submitted to the Graduate Faculty of the

Kenneth P. Dietrich School of Arts and Sciences

in partial fulfillment of the requirements for the degree of

Doctor of Philosophy in Chemistry

University of Pittsburgh

2013

UNIVERSITY OF PITTSBURGH

KENNETH P. DIETRICH ARTS AND SCIENCES

This dissertation was presented

by

Mengning Ding

It was defended on

June 6th, 2013

and approved by

Alexander Star, Associate Professor, Department of Chemistry

Nathaniel L. Rosi, Associate Professor, Department of Chemistry

David H. Waldeck, Professor, Department Chair, Department of Chemistry

David W. Greve, Professor, Department of Electrical and Computer Engineering, CMU

Dissertation Advisor: Alexander Star, Associate Professor, Department of Chemistry

Reproduced with permissions from:

Ding, M.; Tang, Y.; Gou, P.; Reber, M. J.; Star, A. *Adv. Mater.* **2011**, *23*, 536-540.

Ding, M.; Star, A. *MRS Proceedings* **2012**, *1408*, mrsf11-1408-bb05-17.

Ding, M.; Sorescu, D. C.; Kotchey, G. P.; Star, A. *J. Am. Chem. Soc.* **2012**, *134*, 3472-3479.

Ding, M.; Star, A. *Angew. Chem. Int. Ed.* **2012**, *51*, 7637-7638.

Ding, M.; Tang. Y.; Star, A. *J. Phys. Chem. Lett.* **2013**, *4*, 147-160.

Ding, M.; Star, A. *ACS Appl. Mater. Interfaces* **2013**, *5*, 1928-1936.

Ding, M.; Sorescu, D. C.; Star, A. *J. Am. Chem. Soc.* **2013**, *135*, 9015-9022.

Hybrid Nanomaterials Based on Carbon Nanotubes and Graphene: Synthesis, Interfacial Processes, and Applications in Chemical Sensing

Mengning Ding, PhD

University of Pittsburgh, 2013

Development of hybrid nanostructures based on two or more building blocks can significantly expand the complexity and functionality of nanomaterials. For the specific objective of advanced sensing materials, single-walled carbon nanotubes and graphene have been recognized as ideal platforms, because of their unique physical and chemical properties. Other functional building blocks include polymers, metal and metal oxide nanostructures, and each of them has the potential to offer unique advances in the hybrid systems. In any case of constructing hybrid nanostructures, challenges exist in the controlling of composition, morphology and structure of different nanoscale building blocks, as well as the precise placement of these building blocks in the final assembly. Both objectives require systematical exploration of the synthetic conditions. Furthermore, there has been an increasing recognition of the fundamental importance of interface within the nanohybrid systems, which also requires detailed investigation.

We have successfully developed several innovative synthetic strategies to regulate the assembly of nanoscale building blocks and to control the morphology of the hybrid systems based on graphitic carbon nanomaterials. We demonstrate the importance of surface chemistry of each building block in these approaches. Moreover, interfacial processes in the hybrid system have been carefully investigated to elucidate their impacts on the functions of the hybrid products.

Specifically, we explored the synthesis and characterization of hybrid nanomaterials based on single-walled carbon nanotubes and graphene, with other building blocks including conducting polymers, metal, metal oxide and ceramic nanostructures. We demonstrated the development of core/shell morphology for polyaniline and titanium dioxide functionalized single-walled carbon nanotubes, and we showed a bottom-up synthesis of metal nanostructures that involves directed assembly and nanowelding of metal nanoparticles on the graphitic surfaces. Through electrical, electrochemical and spectroscopic characterizations, we further investigated their surface chemistry, interfacial interaction/processes, as well as their fundamental influence on the performance of the hybrid systems. We showed improved or even synergic properties for each hybrid system. Their chemical sensitivities, material stabilities, and charge separation efficiency were superior to individual components. These properties hold great promise in the real-world sensor applications, and can potentially benefit other research fields such as catalysis and green energy.

TABLE OF CONTENTS

LIST OF TABLES

LIST OF FIGURES

PREFACE

I would like to express my sincere gratitude towards my research advisor, Dr. Alexander Star, who has continuously motivated me to improve and challenge myself to overcome my limitations. Throughout my graduate studies, Dr. Star has truly inspired me to become an innovative, independent and patient researcher, and he taught me never to take anything for granted. I would also like to thank my other committee members, Dr. Rosi, Dr. Waldeck, and Dr. Greve, for being ideal role models as innovative, knowledgeable and respected scientists. My appreciation also goes to my collaborators (especially Dr. Sorescu) and colleagues in this group, who not only offered great help to my research, but also created an enjoyable working environment. Special thanks to my parents, who have always been supportive of my graduate study, and to my friends, who have made my graduate life colorful. Finally, to the love of my life, my wife, Si, thank you for your kindness, your support, and for always being there for me. Meeting you was the greatest experience of my graduate life, and our marriage is my biggest achievement I have ever made.

1.0 INTRODUCTION

Increasing compositional and structural complexity of materials has been recognized as one of the most important strategies in the field of material chemistry, for the expanded material functionality that could benefit a wide scope of applications. Specific to nanomaterials, this principle has led to considerable research efforts in the development of novel hybrid/functional nanostructures, which increases the impact of nanotechnology on semiconductor electronics,[1] medicine,[2-4] catalysis,[5-6] energy generation/storage[7-10] and sensors.[4, 11-14]

The simplest scenario of increasing the nanomaterial complexity is to combine two or more distinct constituents into a material system at the nanoscale level. Due to the numerous possibilities of the employment of different building blocks and strategies for their assembly, this approach has resulted in different complex material systems. Three designations are most frequently found in current literature. A term “hybrid materials” (also designated as “hybrid nanomaterials” or “nanohybrids” in the field of nanomaterials) is generally used to describe a combination of two components at nanoscale level, of which one is inorganic while the other is organic in nature.[4, 9, 15-17] “Nanocomposite materials” is another term frequently used in the literature. It usually refers to specific multiphase materials constructed from a bulk matrix mixed with discrete nanoscale phases that differ in compositions and properties, such as bulk polymers or glasses reinforced with nanoscale constituents (nanoparticles, nanofibers, etc.).[18-23] However, in a broader sense, “nanocomposite” term can also be used to indicate a combination of any two

nanomaterials with distinct phases, including nanomaterials functionalized with nanoscale polymer phases[13, 24] or the nanosize inorganic-inorganic composite materials.[25-26] The third typically used designation is “nanoscale heterostructures” (or “nano-heterostructures”). This expression comes from the heterostructures or heterojunctions from the traditional device physics and engineering and has been mostly restricted in the field of inorganic semiconductor nanomaterials for device applications.[27-29] It should be noted that, due to the historical employment of the original terms (i.e., hybrid, composite, heterostructure) and relatively recent emergence of complex nanomaterial systems, the above mentioned designations have not been perfectly and clearly categorized, and could overlap with each other.

Besides the traditional organic (including macromolecular) and inorganic (such as metal or metal oxide) materials and their corresponding nanostructures, graphitic carbon nanomaterials (CNMs) such as carbon nanotubes (CNTs) and graphene have emerged as another important type of building blocks for the construction of hybrid or composite nanomaterial systems, due to their unique chemical structures, properties and potential applications. Although the allotropes of carbon are generally considered as inorganic compounds, both organic and inorganic functionalized graphitic nanostructures were commonly categorized as hybrid materials,[10, 14, 30] which will also be the designation used in the following discussions. As mentioned above, the term of “nanocomposite” (in a broadest sense) also includes carbon nanomaterials hybridized with either organic or inorganic motifs, we choose not to use this designation here in order to avoid including the composite materials with graphitic carbon nanomaterials dispersed in another bulk phase.[18, 22, 31-33]

In any case of constructing the hybrid nanostructures, challenge usually lies in the control of composition, morphology and structure of different nanoscale building blocks, as well as the

precise placement of these building blocks in the final assembly. Both objectives require systematic exploration of the synthetic conditions. In addition, the surface chemistry of each building block, which consequently determines the interface condition of the hybrid system, is also important to these processes. The hybrid interface and related interfacial interaction have received increasing research attentions as they have significant influence on the property and function of the hybrid material. This has therefore become an important topic in physical chemistry of hybrid systems. As the outcome of these fundamental aspects, the resulting hybrid nanomaterials have demonstrated tremendous potential in various practical applications including nano-electronics, nano-medicine, catalysis, green energy and nano-sensors.

In this work, we specifically explore the synthesis and characterization of hybrid nanomaterial systems based on graphitic carbon nanostructures, including single-walled carbon nanotubes (SWNTs) and graphene, as well as other building blocks, including conducting polymers, metal, metal oxide and ceramic nanostructures. We demonstrate the development of novel chemical approaches for the synthesis/assembly of different building blocks, investigation of their surface chemistry and interfacial interaction/processes, as well as their applications in chemical sensing, breath diagnostics, and energy applications.

1.1 GRAPHITIC CARBON NANOMATERIALS

Carbon has long been known for its various allotropes that differ in their chemical structure and material properties, from sp^3 hybridized diamond to sp^2 graphite. The family of carbon allotropes has been further enriched with the emergence of nanoscience and nanotechnology, as zero-

dimensional (0-D) fullerene,[34] one-dimensional (1-D) carbon nanotubes[35-37] and two-dimensional (2-D) graphene[38-39] have been subsequently discovered and characterized.

Fullerenes, carbon nanotubes and graphene are all comprised from sp^2 hybridized carbon atoms and are therefore designated as graphitic carbon nanomaterials (Figure 1-1).[40] These nanoscale carbon allotropes have unique chemical structures which further lead to physical properties that are distinct from bulk graphitic materials and that are superior to graphite for particular applications. These include their electrical, mechanical and optical properties. Because of their unique and advanced properties, the employment of graphitic carbon nanomaterials has enabled or improved a variety of practical applications (reinforced polymer material, nano-electronic, photovoltaic, etc.), making them representative landmarks in the fields of nanoscience and nanotechnology.

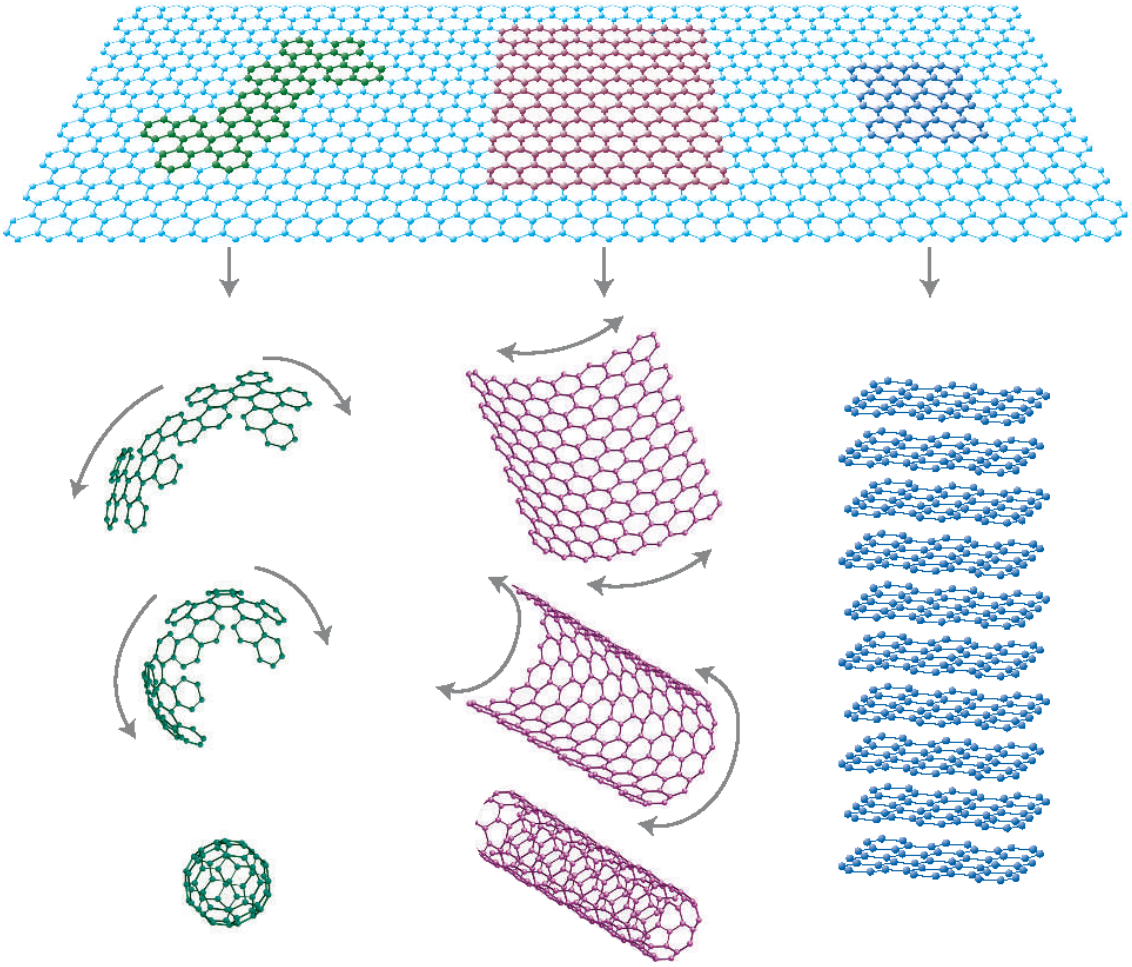

Figure 1-1. Building blocks for all graphitic forms. Construction of zero-dimensional (0-D) fullerene, one-dimensional (1-D) carbon nanotube and three-dimensional (3-D) graphite from the two-dimensional (2-D) graphene (a single layer of graphite) as the building block. Reprinted with permission from reference [40]. Copyright 2007 Nature Publishing Group.

1.1.1 Carbon Nanotubes.

A carbon nanotube (CNT) is a molecular tube made up of sp^2 hybridized carbon atoms in the hexagonal honeycomb lattice,[41] which can be visualized as a cylindrical roll-up of one or a few graphene sheets (Figure 1-1). It was first reported by Iijima in 1991,[35] where the observation of "nanometer-size, needle-like tubes of carbon" was claimed and later referred as the "helical microtubules of graphitic carbon". This material was later designated as carbon nanotubes. The CNTs discovered in 1991 were multi-walled carbon nanotubes (MWNTs), which contain several coaxial packed cylindrical graphene sheets. Another important type of carbon nanotube that contains only one graphitic wall, single-walled carbon nanotubes (SWNTs), was reported independently by Iijima[36] and an IBM research group[37] in 1993. Currently the large scale synthesis of CNTs can be easily achieved through arc discharge or chemical vapor deposition (CVD), and industrial production and commercialization of CNTs have also been realized.

CNTs possess a wide range of superior properties due to their unique structures.[41] Because of the graphitic lattice along the tube axis, CNTs maintain most of the in-plane properties of graphite such as high conductivity, excellent axial strength and stiffness, chemical stability along with some unusual properties such as the chirality-dependent electronic structures. In addition, due to their nanometer diameters CNTs demonstrate unique advanced properties such as high surface area and large flexibility, which could enable many interesting applications from nanotech body armor to space elevators.

SWNTs have more interesting and unique properties compared to MWNTs. Specifically, they have optical and electronic properties that are highly dependent on their diameter and chirality, due to the multiple possibilities to roll up the graphene sheet. This process can be characterized by roll-up vectors (or Hamada factor) $\boldsymbol{C}_h = n\boldsymbol{a_1} + m\boldsymbol{a_2}$ (n, m), where $\boldsymbol{a_1}$ and $\boldsymbol{a_2}$ are unit

vectors for the honeycomb lattice of the graphene sheet and n and m are characteristic integers,[42-44] as illustrated in Figure 1-2a. With different SWNTs exhibiting either zero or small band gap (i.e., metallic for n-m=3k, where k is an integer), or large band gap (i.e., semiconducting for n-m≠3k).[43] Figure 1-2b shows the energy versus density of state (DOS) diagram for a demonstrative metallic (7,7)- and semiconducting (11,3)-SWNT, as calculated from tight binding theory.[45] The unique electronic structure of SWNTs is governed by the electron confinement in their radial direction, with several sharp energy spikes (known as van Hove singularities) in their density of states (DOS).[46] In the case of metallic SWNTs (met-SWNTs), there is a finite allowed state between the valence band (VB, shaded) and conduction band (CB, empty) in the DOS. As for semiconducting SWNTs (sem-SWNTs), a clear gap represents a forbidden energy state region between the conduction and valence bands.[44] Electron transitions between these singularities result in characteristic absorption spectra in the ultraviolet (UV), visible, and near-infrared (NIR) regions, and UV−vis−NIR absorption spectroscopy has been found as a valuable tool for the characterization of SWNTs and related nanohybrid systems, where both suspended samples and solid state thin films could be studied.[30] Furthermore, compared with Si-based semiconductors, sem-SWNTs are direct band-gap materials and therefore ideal for the employment of both electronic and optoelectronic technologies spontaneously.[47] Without specific control of the synthetic conditions or additional separation, as-synthesized carbon nanotubes usually exist as a mixture of two-thirds of semiconducting and one-third of metallic, which is in accordance with zero-folding scheme.[48]

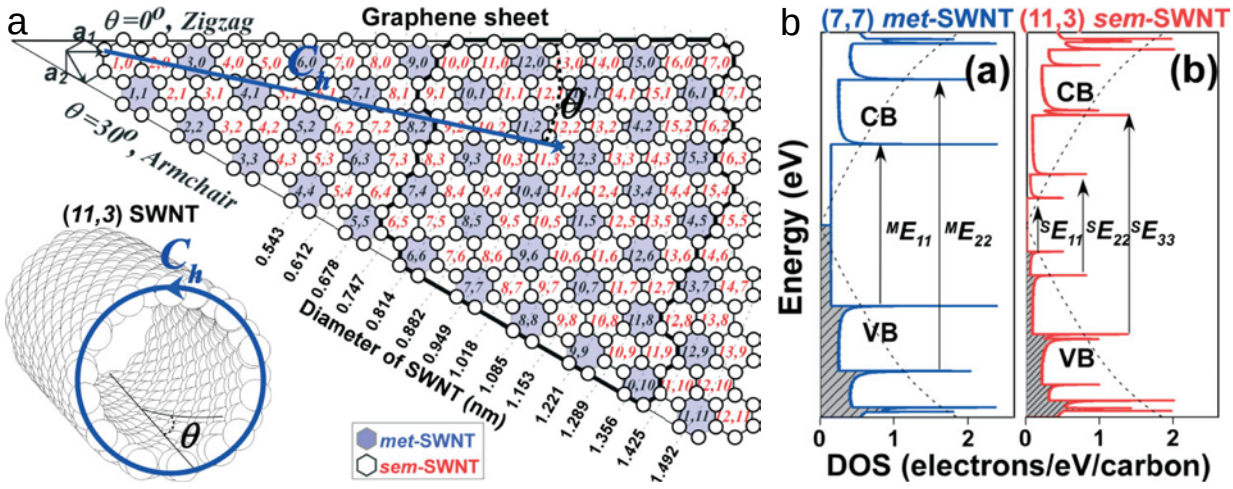

Figure 1-2. Chirality dependent electrical structure of SWNTs. (a) Illustrative map for the roll up of a graphene sheet into SWNTs with different chiralities and diameters. Hamada vector (n,m) and electrical properties (metallic or semiconducting) of SWNTs are demonstrated. Bottom left inset depicts a (11,3) nanotube. (b) Illustration of the density of states (DOS) versus energy for a representative (7,7) met- and a (11,3) sem-SWNT. The conduction band (CB), valence band (VB) and possible electron transitions are demonstrated. Reprinted with permission from reference [44]. Copyright 2007 Wiley-VCH.

1.1.2 Graphene.

Graphene can be simply described as a single atomic layer of bulk graphite (Figure 1-1). The theoretical studies of graphene have been conducted for several decades,[49-50] and the electronic structure of graphene has been constantly used as a theoretical model to discuss the electrical properties of other graphitic materials (such as SWNTs). Despite early attempts to trace graphene materials back to the 1970s,[51-52] the first successful isolation of monolayer graphene was only reported in 2004, when mechanical exfoliation of graphite was conducted using a simple "scotch tape" approach.[38-39] Later on the production of epitaxial graphene was realized through the high temperature decomposition of single crystalline silicon carbide (SiC),[53-55] on a relatively larger

scale. Chemical vapor deposition (CVD) on a metal surfaces[56-60] and chemical exfoliations of graphite[61-64] have also been extensively investigated for the large scale production of graphene, however the latter method has constantly generated defected and functionalized graphitic sheets that are normally designated as graphene oxide (GO).[61] Because of the tremendous research outcomes and broad fundamental understandings that have already been achieved with CNTs, the physics[65-68] and chemistry[61-62, 69-72] of graphene and related materials have been rapidly and comprehensively studied since their discovery.

1.2 HYBRID NANOMATERIALS ASSEMBLED FROM GRAPHITIC AND OTHER BUILDING BLOCKS

Based on the scaffold of graphitic carbon nanomaterials including carbon nanotubes (CNTs) and graphene (or sometimes graphite oxides), a number of different nanomaterials and nanostructures have been employed as building blocks to further construct complex hybrid material systems. Typical types of nanoscale building blocks include organic macromolecular (polymer) nanostructures and inorganic (metal, metal oxide or other semiconductor) nanostructures.

1.2.1 Polymer Functionalized Carbon Nanomaterials.

CNT composites with organic polymers have been studied for nearly two decades. Shortly after the discovery of CNTs in 1991, the first polymeric nanocomposites using dispersed carbon nanotubes as additives were reported in 1994.[73] Later on the addition of carbon nanomaterials (CNMs) into bulk polymer matrix has become an important approach for the development of

reinforced polymer composites (or designated as nanocomposites).[18, 22, 31-33] As for the aspect of keeping the nanoscale dimensions for both CNMs and polymers, another approach of combining graphitic CNMs and polymer materials was to employ CNMs as scaffolds and constructing hybrid systems through polymer functionalization. Efforts to develop polymer functionalized CNTs were based on two different synthetic approaches: covalent functionalization ("grafting to" and "grafting from" CNTs sidewalls carried out by organic synthetic methods)[74-75] and non-covalent functionalization (through mechanical mixing/wrapping, drop-casting, dip-coating, etc.).[76-77]

Among many types of polymers that have been employed as functional motifs with CNMs, conjugated polymers (or conducting polymers, CP) have attracted the most research attention, due to their unique electrical properties that can be coupled with SWNTs or graphene and find applications in the field of nanoelectronics. For modifications of CNTs with conducting polymers (e.g., polyaniline, polypyrrole, polythiophene etc.), most successful examples were firstly carried out through electrochemical polymerization,[74, 78-79] mainly because of i) the high conductivity of CNTs which could therefore function as a working electrode for the electro-polymerization and ii) their poor solubility in water that limited the solution phase synthesis (therefore CNTs devices were fabricated before polymerization). Later on the *in situ* polymerization of conducting polymers in the presence of CNTs were also reported in the literature.[80-81] As the polymerization of conducting polymers was usually carried out in aqueous solution through an oxidative polymerization mechanism, such *in situ* synthesis often required the use of surface functionalized CNTs for a better suspension, which creates significant difficulties in preserving their electronic properties (especially for SWNTs). On the other hand, noncovalent interactions between conjugated polymers and CNTs were realized as an alternative

approach to synthesize SWNT-CP composite materials while the graphitic lattice of SWNTs retained its pristine nature.[82-84] Up until now all these synthetic approaches for the development of conducting polymers functionalized CNTs (with emphasis on SWNTs most recently) or graphene have been extensively explored, as well summarized in several review articles.[74-75, 77, 85] One challenge remains for the synthesis of such hybrid materials is how to control the structure, morphology, and interfacial conditions of the SWNT-CP nanostructures at the nanoscale or even atomic level. One example will be demonstrated in Chapter 2.

1.2.2 Metal Functionalized Carbon Nanomaterials.

Similar to organic polymers that have been used to functionalize CNMs, development of hybrid nanostructures based on CNMs and inorganic motifs has also attracted significant interest in the literature. One specific difference of using inorganic materials to build hybrid structures is that they have different nanostructures themselves (e.g., metal nanoparticles and nanowires) and can therefore enrich the possible combinations of the graphitic and inorganic building blocks. Nanoscale inorganic building blocks that have been most frequently employed include metal nanostructures, metal oxide nanostructures, and other semiconductor nanostructures (such as quantum dots). A brief introduction to metal functionalized CNMs is given in this section and the metal oxide functionalized CNMs will be discussed in the next section.

The metal nanoparticle-decorated carbon nanotubes were first reported in 1994.[86] At that time, the low solubility of raw CNTs significantly limited their functionalization with metal nanoparticles.[87] With the rapid progress in the chemistry and processing of CNTs, development of CNT-metal nanoparticle hybrids has been boosted since the 2000s.[30, 88-92] Such hybrid systems

have been found advantageous in many applications such as i) catalysis because of the high surface area of both building blocks and extremely reactive surface of metal nanocrystals, and ii) chemical sensing, where the high electrical conductivity of SWNTs as well as the selective chemical activity of the metal functionalization play important roles.[30] Similarly, graphene-metal hybrid structures have also been extensively reported.[85, 93]

Synthetic approaches developed for the graphitic-metal hybrid nanostructures can be divided into two categories based on the preparation of metal nanostructures. The first category includes the cases where metal nanoparticles were synthesized prior to their attachment to the CNMs; and the second category encompasses various synthetic methods where metal nanoparticles (or other metal nanostructures) were formed *in situ* on the graphitic surfaces of CNMs, including aggregation of metal atoms, thermal, chemical or electrochemical reduction of metal ions and welding of metal nanostructures. These synthetic strategies of graphitic-metal hybrid nano-assemblies have been summarized in great details.[97-101] There has been a recent shift of focus to the importance of metal-graphitic interfaces that significantly impact the assembly, interaction and properties of the hybrid systems,[14] and their synthetic approaches have also been categorized based on the formation of different interfacial conditions.[30] The interfaces between metal nanoparticles and graphitic surface within the hybrid nanomaterials and their influence will be further introduced in Section 1.3, and our specific work of constructing a metal nanowire-SWNT hybrid nanomaterial where a novel self-assembly and nanowelding process was mediated by the control of interfacial conditions, will be demonstrated in Chapter 3.

1.2.3 Metal Oxide Functionalized Carbon Nanomaterials.

Metal oxides are another important and valuable type of inorganic building blocks that have contributed to a large part of the CNM-based nanohybrids family. Similar to the synthetic strategies of CNM-metal hybrid nanostructures, the preparation of CNM-metal oxide hybrid nanostructures could be categorized as *ex situ* and *in situ* approaches.[92] While an *ex situ* approach is relatively less employed due to the more difficult synthesis of well-defined nanocrystalline metal oxides, this type of hybrid nanomaterial was mostly prepared through hydrolysis based chemistry, such as sol-gel process, hydrothermal reaction, atomic layer deposition (ALD) and chemical vapor deposition (CVD), as summarized in several review articles.[85, 92-93] The importance of the CNM-metal oxide hybrid nanomaterials lies in the wide scope of their applications in photovoltaics,[7, 94] energy conversion/storage,[10, 95] and photocatalysis.[96-97] The incorporation of graphitic CNMs has also been demonstrated to often have significant enhancement on the performance of these hybrid nanomaterial systems.

In many cases the interfacial charge transfer between the metal oxide motifs and CNMs in the hybrid systems plays an essential role for the enhancement of the material performance. Therefore it is fundamentally important to develop a convenient and straightforward method to characterize the efficiency of such interaction. In Chapter 4, our work[98] on the synthesis of CNM-TiO_2 hybrid nanostructures with controlled interfacial conditions will be presented. Utilizing the electrical behavior of SWNTs, we demonstrate the successful probing and systematic investigation of the interfacial electronic coupling, charge separation, and photocatalytic activities.

1.3 HYBRID INTERFACE AND INTERFACIAL PROCESS

Interfaces are instantly generated during the construction of hybrid nanomaterials with more than two types of building blocks. There has been an increasing recognition of the fundamental importance of surface chemistry and interface details within these systems, as they generally act as key factors to achieve the precise placement of organic/inorganic building blocks with fine controlled morphology and advanced functions.

1.3.1 Four Types of Graphitic-Metal Interfaces

Among different nanohybrid systems discussed here (graphitic-polymer, graphitic-metal and graphitic-metal oxide), the graphitic-metal interface is most complicated because distinct surface functionalities on both the metal and the graphitic surfaces should be considered. Therefore, different types of graphitic-metal interfaces are discussed here in detail, and interfaces in the other two hybrid systems can be understood by analogy. The interfaces in a CNM-metal hybrid nanostructure can be divided into four categories, based on different surface functionalities on graphitic surfaces (pristine or non-pristine), which appear to be most influential on the system. The four categories are illustrated in Figure 1-3.[30] For the clarity of discussion on this topic, examples for all the synthetic approaches mentioned in the following section will not be exclusively listed (see section 1.2 for this purpose).

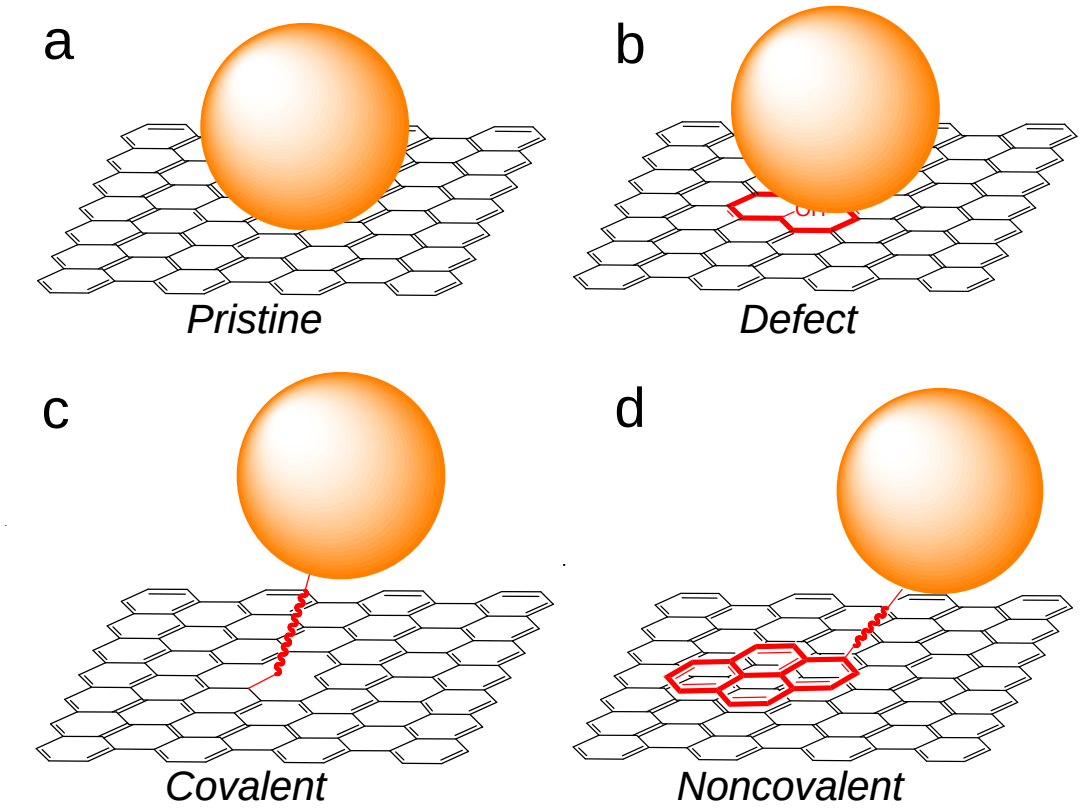

Figure 1-3. Schematic illustrations of four different types of graphitic-metal interfaces. (a) The pristine interface where metal nanoparticles and pristine graphitic surfaces are in direct contact. (b) Metal-defect interface where atoms of metal nanoparticles are bonded to the defect sites of the graphitic surfaces. (c) Covalent interface where covalent bonding between organic linkers and the graphitic surfaces are formed. (d) Noncovalent interface where organic linkers are attached to the graphitic surface through noncovalent interactions. Reprinted with permission from reference [30]. Copyright 2013 American Chemical Society.

The pristine interface is defined by the direct physical contact between pristine metal and graphitic surfaces, as illustrated in Figure 1-3a. Such a concise scenario has usually been achieved in the method where two criteria were matched: i) the metal nanostructures were formed directly on the graphitic surfaces without the employment of any chemical reducing agent or other surfactant, as those typically result in adsorbed molecules on the nanoparticle surface for their stabilization; and ii) the graphitic template was used without any oxidative treatment or surfactant adsorption. Methods for the direct formation of metal nanoparticles (MNPs) on pristine CNT surfaces include direct reduction by SWNTs, galvanic reduction, electro-deposition, and other solvent-free methods such as thermal decomposition and H_2 reduction, thermal and electron beam evaporation, or sputtering coating, as summarized in detail elsewhere.[30] For graphene-based hybrid system, fewer examples of pristine interfaces were reported, as high-quality pristine graphene could only be prepared in limited synthetic approaches.

As compared to pristine metal-graphitic interfaces, non-pristine interfaces have been demonstrated more frequently in the literature where a covalent functionalization approach was involved for the synthesis of CNM-metal hybrid nanostructures. Covalent interfaces could be firstly originated from either graphitic defect sites, such as non-hexagonal rings, edges and vacancies, or oxygenated defects sites (Figure 1-3b). Nitrogen doping is another special method to functionalize the graphitic CNMs with natural defect sites at the nitrogen functional center.

Further reactions with functional groups on the graphitic surfaces could also be applied to generate a covalent linkage between the graphitic and metal surfaces (Figure 1-3c). Other than reactions from defected graphitic surfaces, a covalent interface could also be accomplished by

covalently attaching organic linkers to the pristine graphitic surfaces, through specific organic reactions such as Bingel reaction, photoinitiated carbine addition, and azide photochemistry.

Another type of interface reported in many CNM-metal nanohyrbid materials has a "quasi-pristine" nature. In this system, organic linker molecules were employed for the assembly of MNPs on the surface of CNMs but the interactions between organic linkers and graphitic surfaces were noncovalent, as illustrated in Figure 1-3d. In this scenario graphitic surfaces maintained their pristine structures while there is a molecular layer between the metal and graphitic surfaces. The CNM-metal nanohybirds with a noncovalent interface have attracted increasing attention because of the nondestructive nature of the noncovalent functionalization. This approach has the advantage of preserving the unique optical, electrical, and other physical properties of carbon nanomaterials, while resulting in higher functional densities which in turn led to higher loading of MNPs on the graphitic surfaces, as compared with covalent functionalization. Because of the aromatic structure of graphitic surfaces, most of the applied noncovalent interactions included their hydrophobic interactions with molecular surfactants, wrapping by macromolecules or biomolecules, and π-π stacking with aromatic molecules. The relatively weaker interactions at the noncovalent metal-graphitic or linker-graphitic interfaces have also resulted in some unique surface phenomena that lead to additional advances in the assembly of metal nanocrystals on graphitic surfaces. For example, the use of CNTs for templating the nanocrystal assembly and the bottom-up construction of complex metal nanostructures (such as nanowires) were successfully achieved in the presence of noncovalent interfaces, while similar covalent interfaces were proved to be less effective for this purpose.[14] This specific work will be demonstrated in Chapter 3.

1.3.2 Characterization Methods for Hybrid Interfaces and Interfacial Processes.

To obtain a comprehensive understanding on the interface structure as well as interfacial interactions in the nanohybrid systems, appropriate characterization methods are necessary. The effective characterization of interfaces in the hybrid nanomaterial systems, however, is relatively difficult compared with the more straightforward characterization of the overall hybrid morphology. To date, limited examples of the successful characterization of interfaces have been demonstrated using microscopic technologies (AC-HRTEM, AFM, STM), electrochemical approaches, spectroscopic methods (FTIR, XRD, XPS, UV-vis-NIR, Raman), and electrical measurements, as discussed in the related literature.[30] Among these characterization methods, spectroscopic and electrical measurements utilizing the optical and electrical properties of CNMs (more specifically, SWNTs) have been found to provide most complementary information on the CNM-based hybrid interfaces, based on their sensitivities towards any interfacial charge transfer processes. Therefore, these two characterizations have been recognized as the most promising approaches for the corresponding investigation. The electrical properties of SWNTs and graphene will be briefly introduced in section 1.4. The employment of the optical and electrical characteristics of SWNTs, for a wide scope of fundamental studies and practical applications, will be demonstrated throughout the Chapters 2, 3, and 4.

1.4 ELECTRICAL PROPERTIES AND ELECTRONIC DEVICES BASED ON CARBON NANOMATERIALS AND THEIR HYBRIDS

The numerous unique properties of carbon nanomaterials (especially SWNTs and graphene) have been extensively explored over the last two decades. Among many of their interesting properties, the electrical characteristics of either SWNTs or graphene are arguably most significant and important for scientists and engineers in the field of nanotechnology. The worldwide interests in these materials originate from the continuous desire to overcome the fundamental limitations of traditional Si-based electronic device fabrication and to keep the current trend of miniaturizing the device dimensions and improving the device performance. In addition to the potential applications as circuit materials, the broad exploration of their electrical properties has also led to other promising applications, such as biological and chemical sensors. The organic or inorganic functionalization of SWNTs or graphene also have a significant impact on the electrical behavior of the resulting hybrid nanomaterials, which are often found to be beneficial in certain practical applications.

1.4.1 Electrical Properties and Electronic Devices based on SWNTs.

The theoretical model of the electronic band structure of SWNTs has been briefly discussed in section 1.1.1. The actual electrical properties of MWNTs,[99] sem-SWNTs,[100] met-SWNTs,[101] as well as different junctions between them,[102] have been experimentally studied by many research groups. Many investigations have rapidly established their overall electrical properties, which were systematically summarized in a number of well-written reviews articles.[65, 103-105] One interesting and practically important phenomenon should be emphasized here, that is undopped

semiconducting SWNTs are supposed to be intrinsic semiconductors (Figure 1-2b), however under ambient conditions, they usually appear to have a standard p-type semiconductor behavior (that is, they conduct holes instead of electrons).[106-107] This suggests a partial depletion of electron densities in the valence band of sem-SWNTs. It was established that such a hole-doping of sem-SWNTs results from molecular oxygen adsorption onto the SWNTs surfaces, as the removal of oxygen molecules in vacuum leads back to the intrinsic semiconductor behavior of sem-SWNTs.[106]

The realization of the electrical properties of SWNTs relies on the fabrication of electronic devices. The relatively long length of carbon nanotubes, usually from 100 nm to larger than several μm, makes it easier to fabricate electronic devices out of them using conventional CMOS technology. However, the fine control of the suspension, separation, and alignment of individual SWNTs remains challenging for the large-scale and high density fabrication of sem-SWNT-based devices, with ongoing progress on the related topics.[108-110]

Two basic schemes have been generally employed for the use of SWNTs in an electric circuit. One is to place SWNTs between two metal electrodes and measure their resistance (R; ohms, Ω) or conductance (G; Siemens, S). The conducting motif can be either an individual nanotube[99-102] or a random network of carbon nanotubes,[111] as shown in Figure 1-4a and b. The latter approach of using random arrays of SWNTs has several advantages such as ease of fabrication, high current capacity, low noise levels, small device-to-device variations and compatibility with thin-film technology,[111-113] and has therefore been used for many practical applications such as chemical sensors.[114] Without specific indication, random networks of SWNTs and their hybrid structures are used in Chapter 2, 3, and 4.

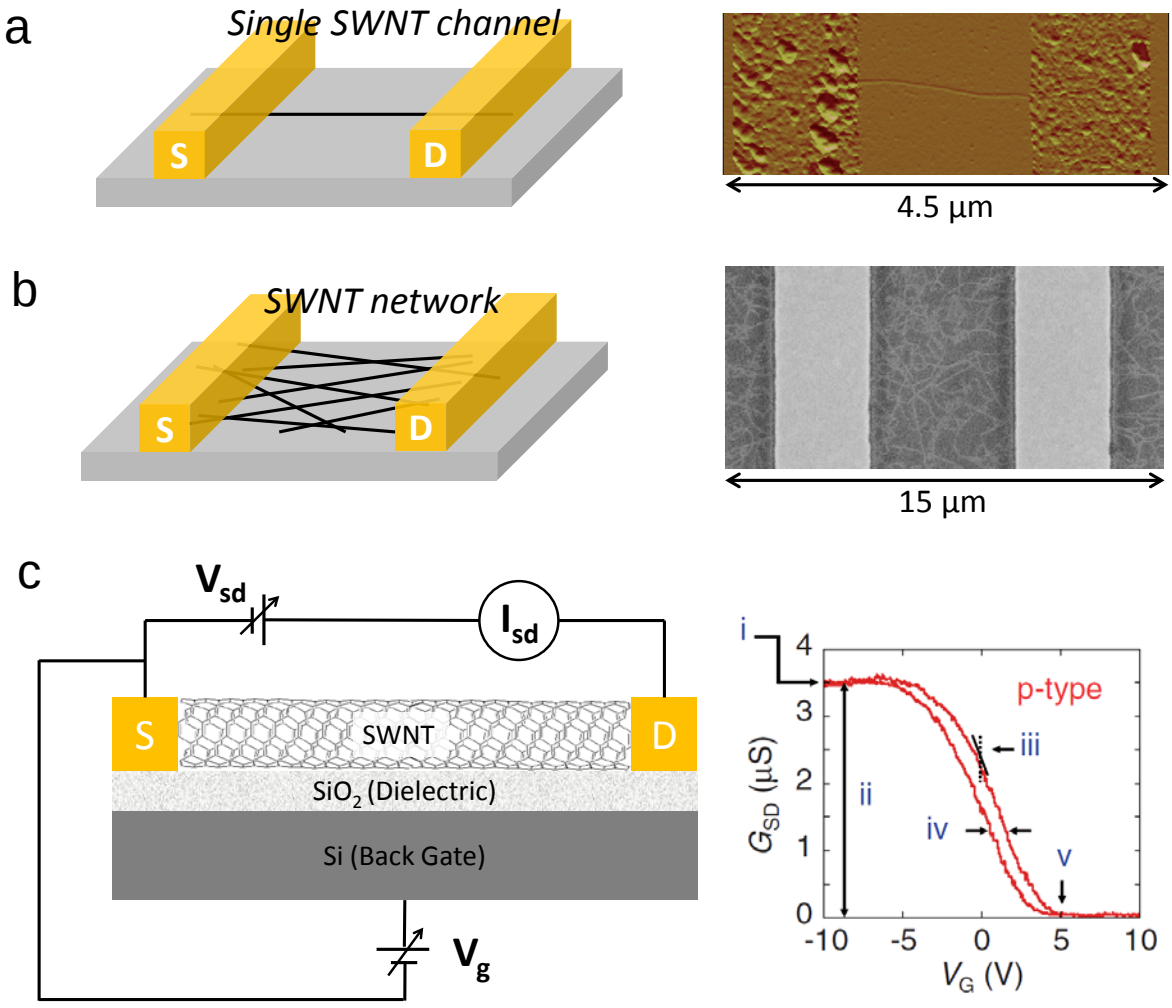

Figure 1-4. Schematic illustration of different device configurations based on single-walled carbon nanotubes (SWNTs). (a) Illustration of a typical resistor based on individual SWNT (black line) bridging two gold electrodes as source (S) and drain (D), with a typical atomic force microscopy (AFM) image of such device on the right. (b) Illustration of a typical resistor based on random network of SWNTs with a scanning electron microscopy (SEM) image on the right. (c) Illustration of a field-effect transistor (FET) device based on SWNTs. Right panel shows a typical transistor characteristic, monitoring the device conductance (G) during the gate voltage (V_g) sweep from -10 V to 10 V, i) maximum conductance, ii) modulation, iii) transconductance, iv) hysteresis, v) threshold voltage. All right panels in (a), (b) and (c) are adapted with permission from reference [115]. Copyright 2007 Wiley-VCH.

A potential barrier is formed at the interface between carbon nanotubes and metal electrodes when p-type semiconducting SWNTs are placed in contact with the electrodes. This phenomenon is commonly known as the "Schottky barrier", which is usually formed at metal-semiconductor junction. The Schottky barrier at metal electrode-carbon nanotube interfaces was first reported by the Hongjie Dai Group in 2000 (although the term "Schottky barrier" was not used in that report)[116] and later systematic work by researchers at IBM established the Schottky barrier between SWNTs and metals (e.g., Ti).[117] The band diagram describing the formation of a Schottky barrier between p-type SWNT and metal electrodes is shown in Figure 1-5. As the formation of Schottky barrier often causes additional resistance and reduces device performance,[117] efforts have been generally made to diminish the barrier during the device fabrication. An easy way is to choose a proper metal with a similar Fermi level compared to that of SWNTs. As a result, Au and Pd electrodes are most frequently used in the SWNTs devices due to their similar work functions (Au ~ 5.0 and Pd ~ 5.1 eV) with p-type SWNT (~5 eV).[118-119]

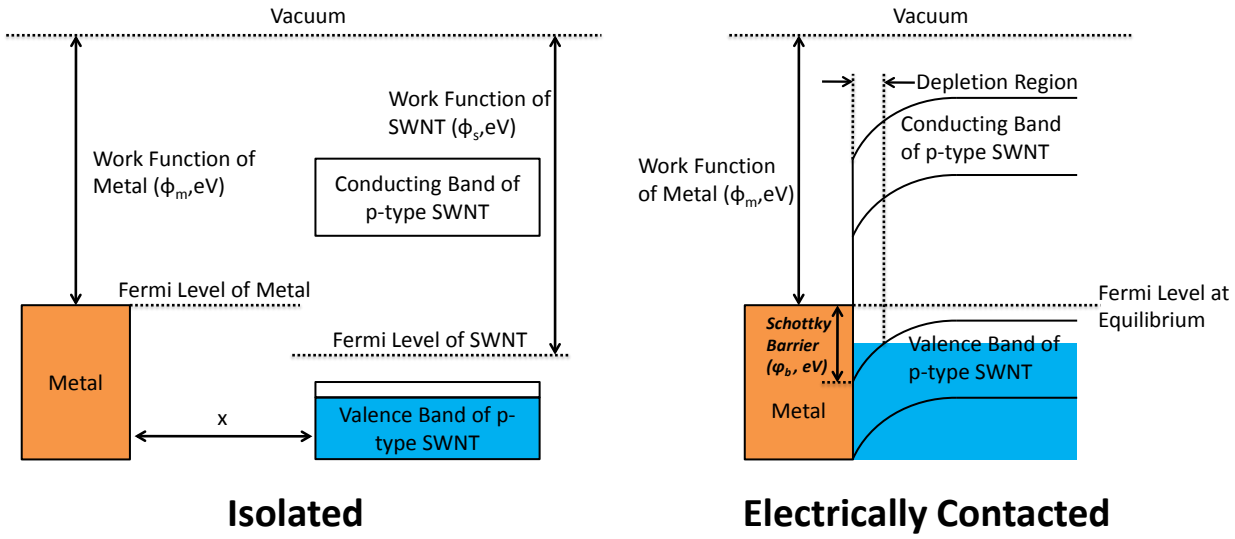

Figure 1-5. Formation of the Schottky barrier between p-type SWNTs and metal electrode: SWNT is separated from the metal electrode at the first place, with a work function (which is, energy needed to move an electron from the Fermi energy level into vacuum) φ_s larger than that of the metal φ_m. When the SWNT comes into electrical contact with metal electrode, the mismatched Fermi levels start to equilibrate. Electrons in metal with higher energy will be donated into the SWNT valence band and bend them towards a higher energy level, such an electron donating process stops when the two Fermi levels reach to equilibrium. The bending of the SWNT bands results in a charge depletion region with a thickness of several nm in the SWNT near its surface, causing a Schottky Barrier which inhibits the transport of holes from p-type SWNT to metal electrode.[120]

The Schottky barrier between the conducting channel and bulk metal electrode of SWNT-based devices is also an early indication that the metal-graphitic interface could become an important factor that determines the overall performance of the nano-devices and nanomaterials. Indeed the "nano Schottky barriers" between metal nanoparticles and SWNTs in the hybrid nanostructures have been observed,[121] and we will demonstrate the advantage of such barriers in the case of chemical sensing in Chapter 3.[14]

Besides the electric resistor, a three-terminal device configuration called a "Field-Effect Transistor (FET)" has also been widely used. As illustrated in Figure 1-4c, the basic FET structure involves two metal electrodes designated as "source" and "drain" connected by a semiconducting channel (in this case, sem-SWNTs) and a third electrode, the "gate," which is separated from the channel by a thin insulator film.[103] For a typical FET transistor device, its conductance (or resistance) can be modulated by the application of a certain gate voltage (V_g). Typical operation of a FET device includes monitoring the change of source-drain current (I_{sd}) as a function of the scanning V_g under a particular bias voltage (V_{sd}), and the device output is called a transistor characteristic (I-V_g or G-V_g curve). In an ideal case, the semiconducting channel remains insulating ("off state") with zero gate voltage and becomes conductive ("on state") with electric field placed on the gate. For a p-type (n-type) FET, when a negative (positive) charge is placed on the gate and the applied voltage V_g exceeds a certain threshold, V_{th}, then a hole (electron) current flows through it. The first demonstration of using semiconducting carbon nanotubes as field-effect transistors (CNTFET) was published in 1998 by Dekker and co-workers[100] as well as researchers at IBM.[122] A typical CNTFET characteristic is shown in Figure 1-4c.

1.4.2 Electrical Properties and Electronic Devices based on Graphene.

Similar to carbon nanotubes, the most intensive research has been directed to the electrical properties of graphene ever since their first isolation in 2004.[38, 40, 65, 123] In addition, graphene has received arguably even more attention because of its fundamental importance to many issues in condensed matter physics. Before the successful realization of single-layer graphene, the classic 2-D materials (atomic monolayer crystals) were predicted to be thermodynamically unstable when free standing.[40]

Graphene can be described as a zero-band gap semiconductor, with its cone-shaped conduction and valence bands meeting at the K points of the Brillouin zone, as illustrated in Figure 1-6a. It has the highest charge carrier mobilities (μ, up to 200 000 $cm^2/V{\cdot}s$)[124] compared with any of the existing materials (met-SWNT has the same order or magnitude, see Figure 1-6b for details). Moreover, such a high level of μ remains high even at the highest carrier concentrations (n, $>10^{12}$ cm^{-2}) either induced by electrical or chemical doping. This feature indicates a ballistic transport of charge carriers in graphene on the submicrometer scale at room temperature (currently up to ~0.3 μm at 300 K).[40]

Graphene exhibits superior conducting properties similar to carbon nanotubes, and is potentially easier for large-scale, high-quality, and reproducible device fabrication and more compatible with the current lithography-based technologies. Therefore, graphene has been recognized as the best possible material for metallic transistor applications.[38, 40] However, for the transistor purpose, graphene is not the ideal choice as it remains conductive even under intrinsic conditions (i.e., in case of zero gate voltage) because of the zero band gap, which leads to a limited on/off ratio of its FET device.[38, 40, 124] For a semiconductor behavior of the graphene-

based device, several approaches have been developed to open the band gap. One method is through the quantum confinement in narrow graphene nanoribbons (<10 nm),[125-126] which mimics the structure of 1-D sem-SWNTs, as shown in Figure 1-6c and d; another involves the generation of holey graphene structures,[127-128] which mimics the structure of an array of SWNT networks (Figure 1-6e).

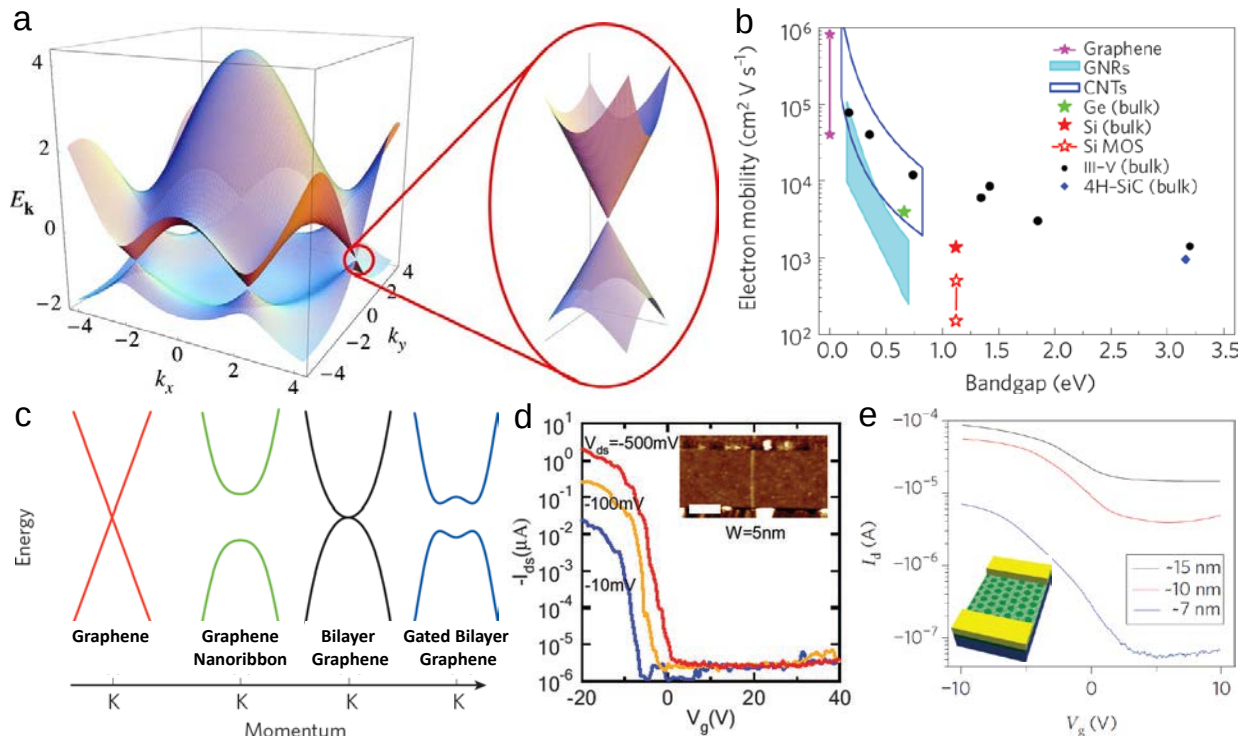

Figure 1-6. Graphene based electronics. (a) Electronic dispersion in the graphene lattice. Right is a zoom in of the energy bands near the Dirac point. Reprinted with permission from reference [123]. Copyright 2009 American Physical Society. (b) Summary of the electron mobilities of different materials. III-V semiconductors include InSb, InAs, $In_{0.53}Ga_{0.47}As$, InP, GaAs, $In_{0.49}Ga_{0.51}P$, and GaN, from left to right, respectively. Data shown for graphene nanoribbons (GNRs) and carbon nanotubes (CNTs) are from simulation. Reprinted with permission from reference [124]. Copyright 2010 Nature Publishing Group. (c) Schematic illustration of bandgap opening of graphene. Adapted with permission from reference [124]. Copyright 2010 Nature Publishing Group. (d) Typical FET characteristics of a graphene nanoribbon with the width of 5 nm. Inset depicts an atomic force microscopy (AFM) image of such device. Reprinted with permission from reference [126]. Copyright 2008 American Association for the Advancement of Science. (e) Typical FET characteristics of graphene nanomesh (with estimated neck width of ~7, 10 and 15 nm) devices. Inset depicts the schematic illustration of such device. Adapted with permission from reference [127]. Copyright 2010 Nature Publishing Group.

1.5 CARBON NANOMATERIAL BASED CHEMICAL SENSORS

Another structural uniqueness of SWNTs and graphene is that they are both entirely composed of surface atoms. This feature not only leads to a large surface-to-volume ratio but also results in the electrical characteristics that are extremely sensitive towards any disturbance in their surrounding environment. Combined with other of their above-mentioned superior properties, SWNTs and graphene represent an ideal sensing platform for chemical detection of gases and vapors in air, as well as molecules, ions and biomolecules in solution.[44, 114-115, 129-130] Here we mainly focus on the uses of SWNT and graphene as chemical gas/vapor sensors. The most convenient and frequently used sensing scheme is to monitor the conductance/resistance of SWNT or graphene in a resistor configuration. The change of their conductance upon exposure to the analyte molecules can be read as the signal. Such a configuration with conductance that is sensitive to its chemical environment, also designated as chemiresistor, is illustrated in Figure 1-7 a and b. While other device configurations such as FET,[129-130] capacitor[114] or electrochemical cells[44] have also been successfully developed for chemical sensing, the chemiresistor is by far the simplest setup for such purpose, and has the best potential for its future commercialization as low-cost, low-power, and easy to use sensor devices.

1.5.1 Single-Walled Carbon Nanotubes Based Chemical Sensors.

Numerous studies have shown that the electrical behavior of sem-SWNTs is extremely sensitive to the charge transfer and chemical doping effects induced by a variety of adsorbed molecules.[44, 107, 131] Specifically, when oxidative (or reductive) molecules are adsorbed on the p-type sem-SWNTs, they will withdraw (or donate) electrons from (or to) SWNTs, thus partially depleting

(or adding) the electron density in the valence band of sem-SWNTs (for example, every adsorbed NO_2 molecule withdraws ca. 0.1 electrons from sem-SWNTs).[44] This results in an increase (or decrease) in the number of conducting holes in p-type sem-SWNTs and a decrease (or increase) of their electrical conductance/resistance, which can be a signal for chemical sensing. Such a chemical doping/charge transfer process has been proposed as the sensing mechanism for the SWNT-based sensors since their first report in 2000.[107] However, there was a debate over the actual sensing mechanism using sem-SWNTs in the early 2000s, as either bulk chemical doping or modulation of the Schottky barriers between SWNTs and metal electrodes could result in the considerable change in the device conductance.[132] While both mechanisms have been supported by experimental evidence, the contact barrier effect has become less essential as the random arrays of SWNTs were more frequently used as the conducting channels in the fabrication of chemiresistors. In this configuration, the dominant role of charge transfer effect has been constantly confirmed by the combination of electrical and spectroscopic characterizations.[30, 47] SWNT-based chemiresistors have been demonstrated for the successful detection of a large number of chemical gases/vapors, which have been well-summarized in many review articles.[129-130]

Two problems exist for the real-world applications of SWNT-based chemical sensors. One is that the response of sem-SWNTs relies on their chemical doping, which means it is difficult to achieve high sensitivity towards chemicals with weak doping ability. Second, as bare SWNTs devices can be sensitive to many different chemicals through non-specific binding, the requirement of sensor selectivity needs to be addressed for many specific applications. As a general strategy for the solution, functionalization of SWNTs with an additional recognition layer has been employed to achieve both the desired sensitivity and selectivity for specific

chemical sensing. Polymers, metals, metal oxides and biomolecules have all been explored as the functional motifs.[129-130] While early efforts have been mostly focused on the direct functionalization of a pre-fabricated SWNTs device, recent research has been shifted to the development of novel hybrid nanomaterials based on SWNTs specifically for chemical sensing.[13-14, 30, 98] Examples on this topic are demonstrated in detail through Chapters 2, 3 and 4.

1.5.2 Graphene Based Chemical Sensors.

Successful development of SWNT-based chemical sensors has inspired similar research on graphene. The chemical sensitivity of graphene was first reported in 2007[133] and the field of graphene sensors has been growing ever since.[132, 134-135] Although detection of single molecule adsorption was achieved with the Hall geometry,[133] it has come to the general conclusion that graphene has a lower chemical sensitivity as compared to the SWNTs when both used as chemiresistors. Two major disadvantages of graphene-based devices contribute to their limited sensitivity. First, as graphene is a semi-metallic material with a zero band gap (section 1.4.2), thermal promotion of charge carriers results in a poor transistor behavior at room temperature.[134] For a maximum sensitivity towards the chemical doping effect, the use of a semiconductor is preferred. The second limitation comes from the 2-D structure of graphene.[30, 129, 136] Specifically, 1-D nanostructures such as SWNTs experience a significant change in their electrical conductivities as the charge depletion depth (Debye length) from an adsorbed molecule is comparable to their cross-sectional radius, while a similar depletion region only contributes to a small portion of the conducting surface of 2-D graphene, as illustrated in Figure 1-7c. The break of symmetry and opening of the band gap of graphene can serve as the solution to overcome both limitations. As mentioned in section 1.4.2, 1-D graphene nanoribons (GNRs) and holey reduced

graphene oxide (hRGO) have been developed for this purpose, and some have been applied for chemical sensing applications.[128, 137] Although it is still too early to predict the future outcome of graphene-based sensors at this early stage, the development of novel chemical sensing materials was mainly focused on SWNT-based hybrid nanostructures in Chapters 2, 3 and 4 due to many advantages of SWNTs as the sensing platform.

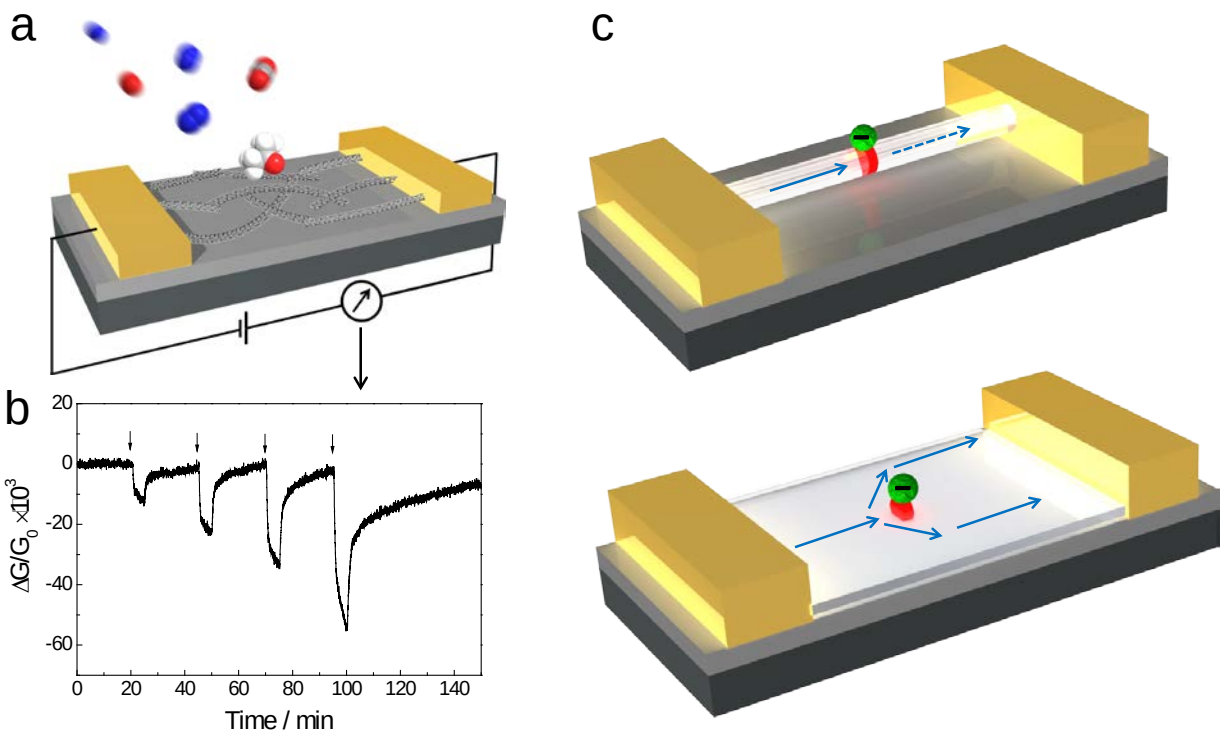

Figure 1-7. Illustration of typical chemiresistors and their interactions with analyte molecules. (a) Schematic cartoon of a chemiresistor composed of SWNTs network upon exposure to gas molecules. (b) A typical conductance (G) response of SWNTs chemiresistor upon exposure to acetone vapors. (c) Schematic illustration of electronic interactions between 1-D (top) and 2-D (bottom) sensing platforms and analyte molecules. The red regions indicate the depletion layer induced by charged analytes (green spheres).

2.0 POLYANILINE COATED SINGLE-WALLED CARBON NANOTUBES FOR CHEMICAL SENSING

2.1 CHAPTER PREFACE

Materials contained in this chapter were published as a research article in *Advanced Materials* and a MRS proceeding; figures used in this chapter have been reprinted with permission from: i) *Adv. Mater.* **2011**, *23*, 536-540 (listed as reference 13 in bibliography section). Copyright 2011 Wiley-VCH. ii) *MRS Proceedings* **2012**, *1408*, mrsf11-1408-bb05-17 (listed as reference 138 in bibliography section). Copyright 2011 Materials Research Society.

List of Authors: Mengning Ding, Yifan Tang, Pingping Gou, Michael J. Reber and Alexander Star.

Author Contributions: DMN and AS designed the experiments and wrote the manuscript, DMN performed the experimental work, YT participated in the electrochemical characterization, PG performed AFM characterization and MJR participated in the sensor measurement.

2.2 INTRODUCTION

Among the numerous macromolecular materials that have been employed to functionalize SWNTs, polyaniline (PAni) appeared to be extremely attractive for the purpose of chemical sensing, because of their advantages as sensing materials themselves.[139] PAni demonstrates sensitivity towards many different analytes due to possible transformations between its different chemical forms, as illustrated in Figure 2-1. Moreover, its 1-D nanostructures, polyaniline nanofibers (PAni NFs), enables sensor films with high porosity that results in excellent sensitivity and response time.[140-142] It is therefore of great interest to explore whether the combination of these two 1-D nanomaterials (i.e., SWNT/PAni hybrid nanomaterials) will provide any combined, or even additional advantages for the development of novel sensors. CNT/PAni hybrid materials were mostly prepared by either *in situ* polymerization of aniline in CNT suspensions,[81, 143-145] or by electropolymerization on CNT electrodes.[79, 146] The resulting CNT/PAni demonstrated better thermal stability and higher sensitivity to ammonia.[143, 145] However, there is still a lack of systematic exploration on the morphology control of the SWNT/PAni hybrid systems, their influence on the chemical sensitivity of hybrid materials, and the exact nature of interactions between SWNT and PAni remain elusive. We have reported[13, 138] the synthesis and chemical sensitivities of different SWNT-PAni composites, including SWNT-PAni mixture, SWNT-PAni nanoparticles, and SWNT/PAni core/shell nanocomposite. We demonstrate that, with fine control of the composite morphology at nanoscale, advanced sensor performance could be achieved. The electronic interactions between SWNT and PAni were further investigated using a combination of electrochemistry, optical spectroscopy, and electrical

transport measurements in order to elucidate the mechanistic aspects of the composite properties and chemical sensing.

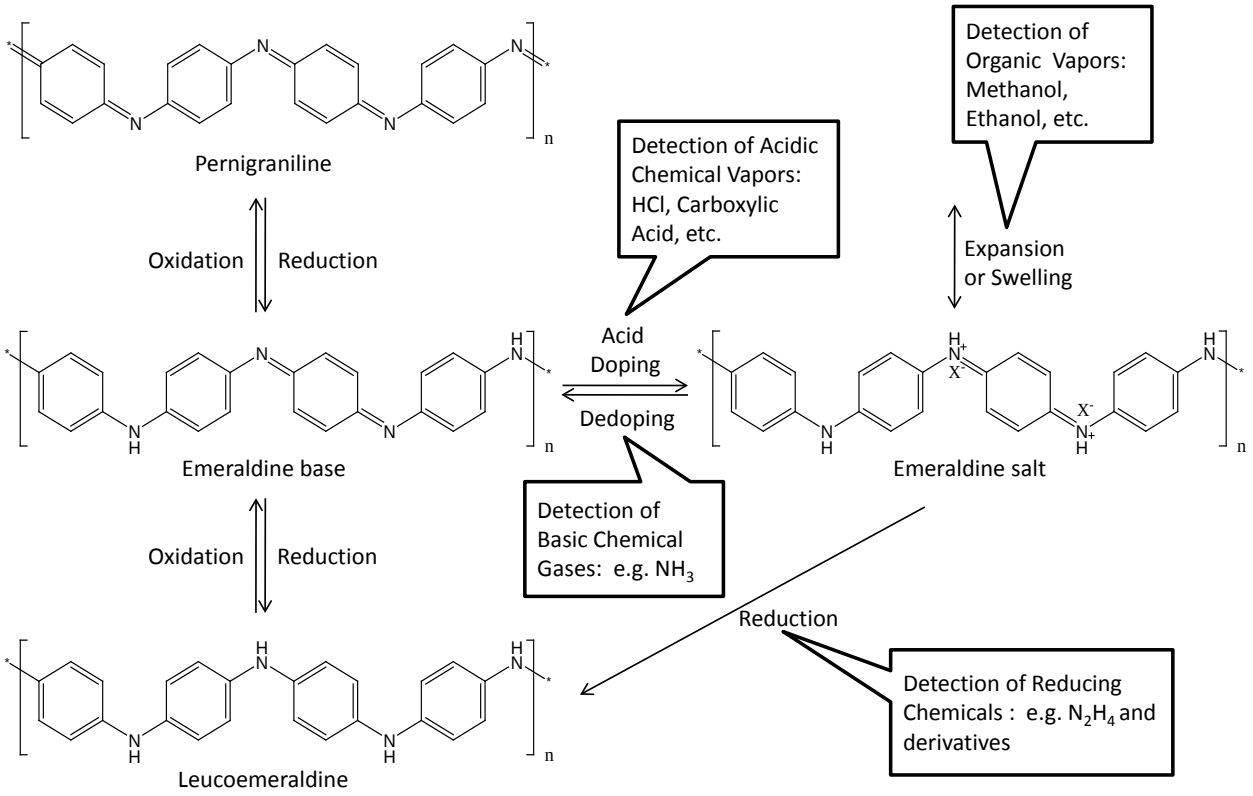

Figure 2-1. Different chemical structures of polyaniline (PAni) and its applications in chemical gas/vapor detection. PAni can exist in different doping levels and oxidation states, with a huge difference in their electrical properties. Such difference gives PAni significant sensitivities to acid/base analytes, as well as redox molecules like N_2H_4. In addition, PAni chains will experience an expansion or swelling upon exposure to certain organic vapors due to the interactions between their backbone nitrogen atoms and organic molecules. Such volume change will also result in a dramatic change in PAni conductance, making it a good sensor for organic vapors.

2.3 EXPERIMENTAL SECTION

Materials: Pristine single-walled carbon nanotubes (SWNTs) were obtained from Carbon Solution Inc. 1-Pyrenesulfonic acid hydrate (1-PSA, $C_{16}H_{10}O_3S \cdot xH_2O$), aniline ($C_6H_5NH_2$), ammonium persulfate ($(NH_4)_2S_2O_8$, ≥98%) and all organic solvents were purchased from Sigma Aldrich and used as received. 40-pin ceramic sidebraze (CERDIP) packages (cavity .310 × .310) were procured from Global Chip Materials, LLC.

Synthesis of Polyaniline nanofibers (PAni NFs): were synthesized using a rapid-mixing method described previously.[140] Briefly, an aqueous solution of aniline (1.5 mmol) in 1M HCl (10 mL) and an aqueous solution of ammonium persulfate (0.4 mmol) were mixed together followed by vigorous stirring for 40 min. The final product was separated by centrifugation and washed with DI water, and then suspended into 20 mL of DI water. HCl or NaOH solutions (1 M) were used to adjust pH values of the suspensions from pH=2 to pH=11.

Synthesis of SWNTs-PAni bulk mixtures: Aniline (0.1 mmol) was added into a DMF (10 mL, containing 1M HCl) solution of pristine SWNTs (0.25 mg). A DMF solution of ammonium persulfate (0.05 mmol) was then poured into aniline and SWNTs suspension followed by vigorous stirring for 30 min. The final product was separated by centrifugation and washed with DMF for several times, and then was suspended in 20 mL of DMF.

Synthesis of SWNT-PAni nanoparticles: Aniline (0.1 mmol) was added into a DMF (10 mL) solution of pristine SWNTs (0.25 mg). A DMF solution of ammonium persulfate (0.05 mmol) was then poured into aniline and SWNTs suspension followed by vigorous stirring for 30 min. The final product was separated by centrifugation and washed with DMF for several times, and then was suspended in 20 mL of DMF.

Synthesis of SWNT-COOH-PAni: Aniline (0.1 mmol) was added into a DMF (10 mL) suspension of carboxylated SWNTs (0.25 mg), which were prepared following the reported procedure.[147] A DMF solution of ammonium persulfate (0.05 mmol) was then poured into aniline and SWNTs solution followed by vigorous stirring for 30 min. The final product was separated by centrifugation and washed with DMF for several times, and then was suspended in 20 mL of DMF.

Synthesis of SWNT/PAni, (in situ aniline polymerization in aqueous suspension of SWNT-PSA complex): Aniline (0.1 mmol) was added into an aqueous (10 mL) suspension of PSA-functionalized SWNTs. An aqueous solution of ammonium persulfate (0.1 mmol) was then poured into the aniline and SWNT-PSA solution followed by vigorous stirring for 0.5-3 hours. The final product was isolated by filtration and washed with DI water and ethanol for several times, and then resuspended in 20 mL of THF or DI water.

General Characterizations: All the synthesized materials were characterized by transmission electron microscopy (TEM, FEI Morgagni), operating at an acceleration voltage of 80 keV. FT-IR spectra were obtained as thin films (NaCl plates) on an Avatar 380 Nicolet FT-IR spectrometer. Thermogravimetric analysis (TGA) was performed using TGA Q500 thermal analysis system.

Electrochemical Measurement: Typically, a sample of SWNT/PAni, pristine SWNTs or PAni NFs (2 mg) was dispersed in a solvent mixture of ethanol (2 mL) and Nafion 117 solution (5wt %, Sigma Aldrich) (10 μL). The working electrode was prepared by drop-casting a Nafion-impregnated sample (20 μL) on to a glassy carbon (GC) electrode (CHI 104, GC area 0.0707 cm^2, total area 0.196 cm^2). Cyclic Voltammetry (CV) was performed using an electrochemical analyzer CHI 604C (CH Instruments, Austin, TX). The electrolyte used was a 0.5 M H_2SO_4

aqueous solution; Pt wire (CHI 115) and Ag/AgCl (3M KCl, CHI 111) electrodes were used as the counter and reference electrodes, respectively.

Spectroscopic Measurement: All the UV-vis-NIR absorption spectra studies were carried out on a Perkin-Elmer Lambda 900 UV-vis-NIR spectrophotometer. In the case of thin film measurements, an Iwata HP-BC Plus airbrush was used to make the thin films. Specifically, all the thin films used in the spectroscopic study were created by spraying a DMF suspension of SWNTs by airbrush onto a 1"×1" quartz plate previously heated to 180°C. A custom-built Teflon gas flow chamber was used to ensure the gas exposure during spectroscopic measurements.

Sensor Device Fabrication: Si wafers with a 300 nm thermal oxide layer and interdigitated gold electrodes were purchased from MEMS and Nanotechnology Exchange. The devices were fabricated by drop-casting either aqueous suspension (10 μL) of the PAni NFs, or DMF/THF suspensions (70 μL) of SWNT/PAni composites onto the Si chips. The Si chips were connected to the 40 CERDIP Packages with Au wires and allowed to dry in ambient.

Gas Sensing Measurements: Gas sensing measurements were carried out on a custom-built system where the electrical conductance of up to 4 chips (16 data output at most) can be measured using Keithley Dual SourceMeter 2602 and Keithley Switching Matrix 708A. The test board was controlled by a Zephyr Measurement Software (an open source, Java-based data acquisition and measurement program available for download at http://zephyr.sourceforge.net). A custom-built Teflon gas flow chamber was used to control the gas/vapor environment for the sensors during the test, as demonstrated inFigure 2-2. Analyte vapors of different concentrations were generated, by mixing saturated vapors with dry N_2, and were passed through the gas chamber containing the device.

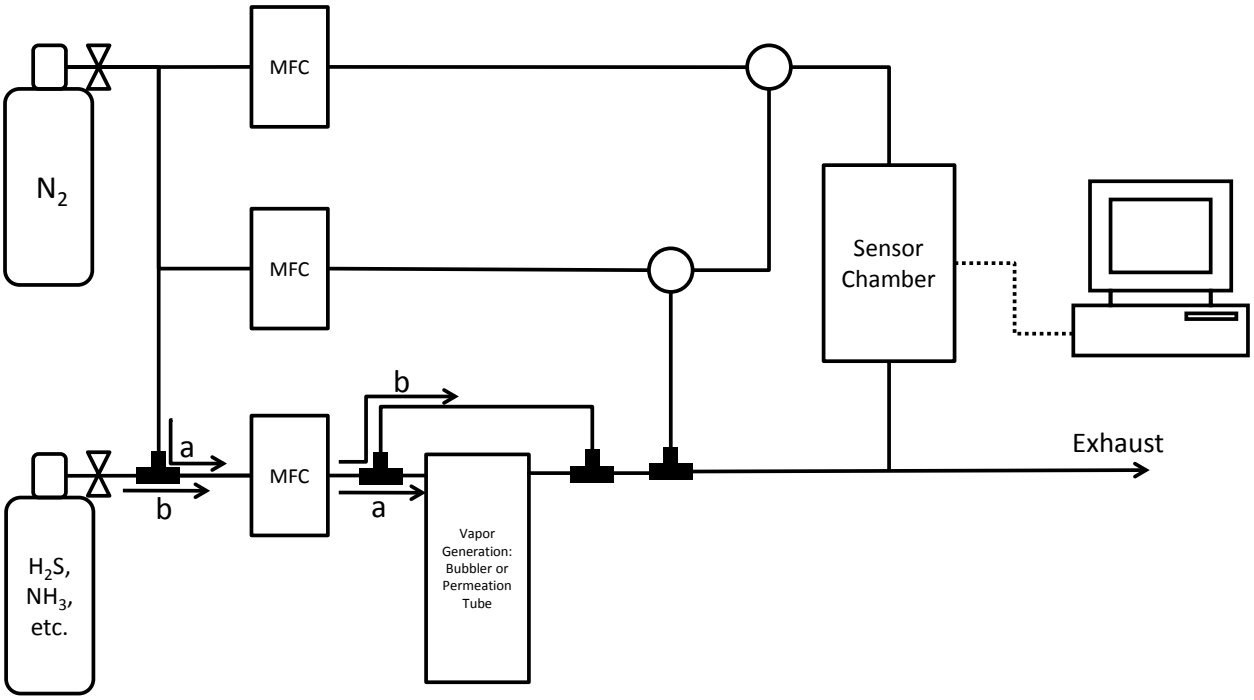

Figure 2-2. Schematic illustration of the gas/vapor generation and detection system. (a) Different saturated vapors of analytes (acetone, acetic acid, etc.) were created by bubbling dry N_2 through liquid analytes at a relatively low flow rate (usually 10-40 sccm, controlled by mass flow controller, MFC), different concentrations of chemical vapors were generated by diluting such saturated vapors with dry N_2 at controlled flow rates. A two stage mixing chamber was needed when large amount of N_2 (compared to saturated vapors) was used. (b) Gaseous mixtures containing different analytes (NH_3, H_2S, etc.) with different concentrations were generated by diluting gaseous analytes with dry N_2 at controlled flow rates. Alternative gas flow directions (a) and (b) were controlled by three way valves.

2.4 RESULTS AND DISCUSSION

2.4.1 Morphology Control of the SWNT/PAni Hybrid Nanostructures

1-D core/shell morphology is a preferred morphology for the potential sensor applications of hybrid nanomaterials. For this purpose, a non-covalent functional approach was employed together with *in situ* polymerization of aniline in the SWNTs suspension (Figure 2-3a). Pristine SWNTs were functionalized with 1-pyrenesulfonic acid (PSA) prior to the polymerization (Figure 2-4). Noncovalent functionalization of SWNTs with PSA was carried out for two reasons: first, similar to other pyrene derivatives,[77, 148] PSA generates a stable aqueous suspension of SWNTs for *in situ* polymerization of aniline while preserving their graphitic lattice and unique electronic properties; second, aniline monomers can complex with the sulfonic groups of PSA thus directing the growth of PAni from the side walls of SWNTs resulting in uniform polymer coating. It should be noted that other surfactants such as sodium dodecyl sulfate (SDS) has been recently used for synthesis of SWNT/PAni composite as a template for monomer assembly and polymerization.[144]

Transmission electron microscopy (TEM) and atomic force microscopy (AFM) of SWNT@PAni reveals that SWNTs were functionalized with a uniform PAni coating, as shown in Figure 2-3b, (also see Figure 2-5). The PAni coating was further confirmed by Fourier transform infraRed spectroscopy (FTIR, Figure 2-3c), where SWNT@PAni composite showed typical absorption peaks at 1512, 1585 and 3263 cm^{-1}. These bands are associated with stretching of benzenoid and quinoid rings as well as N-H stretching of benzenoid amine groups of PAni,

respectively. Thermogravimetric analysis (TGA, Figure 2-3d) confirmed the ratio of PAni to SWNTs is about 1:1 (wt), as SWNT@PAni showed 50% mass loss from 200 to 800 °C in nitrogen. This loss can be attributed to the decomposition of PAni, as pristine SWNTs remain stable in this temperature range (Figure 2-3d).

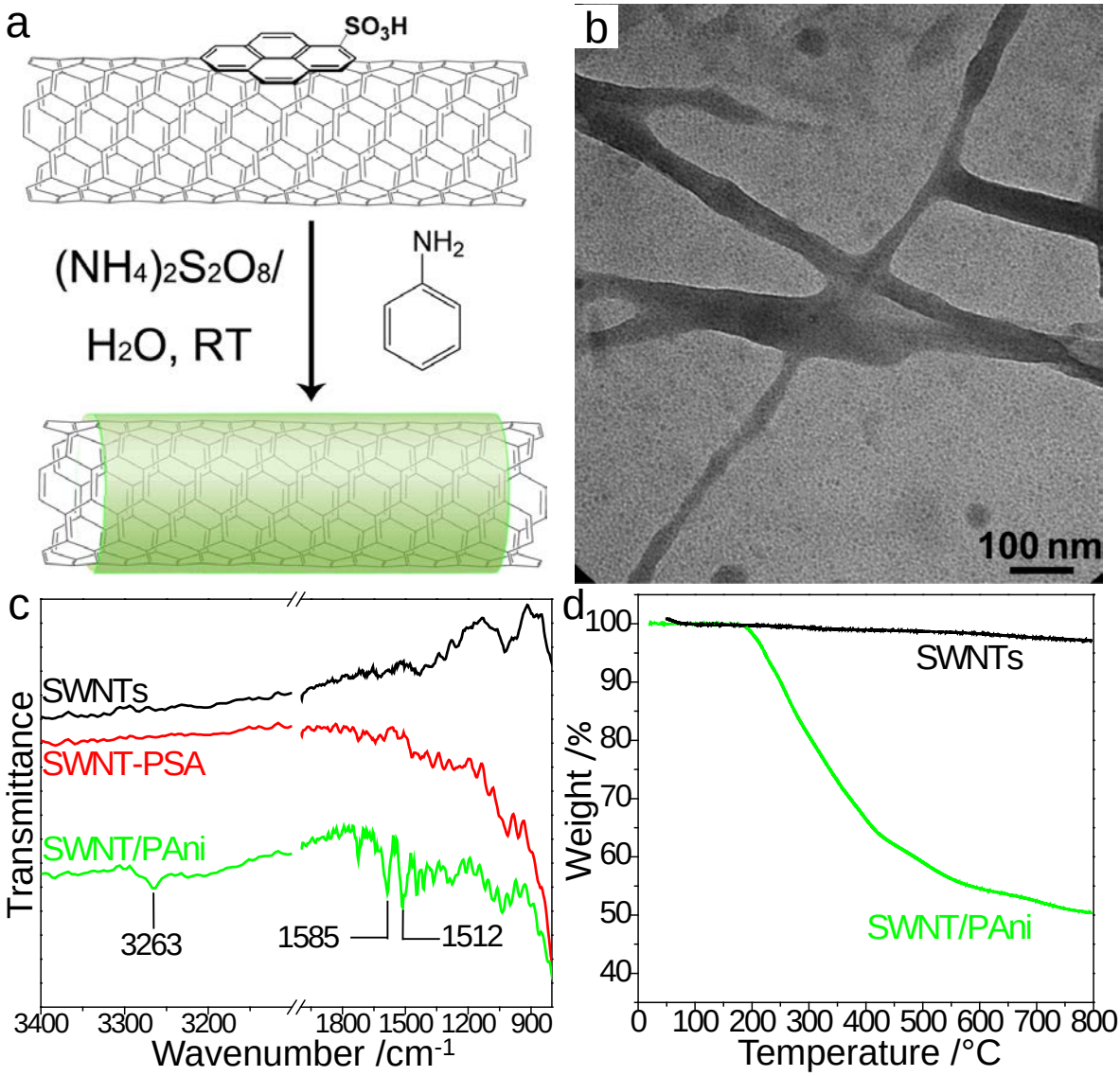

Figure 2-3. Synthesis and characterization of SWNT@PAni hybrid nanostructures with core/shell morphology. (a) Synthetic scheme of SWNT@PAni by *in situ* aniline polymerization onto PSA-modified SWNTs. (b) TEM image of SWNT@PAni. (c) FTIR spectra of pristine SWNTs, PSA-modified SWNTs and SWNT@PAni. (d) TGA traces of pristine SWNTs and SWNT@PAni (in N_2, 10 °C min^{-1}).

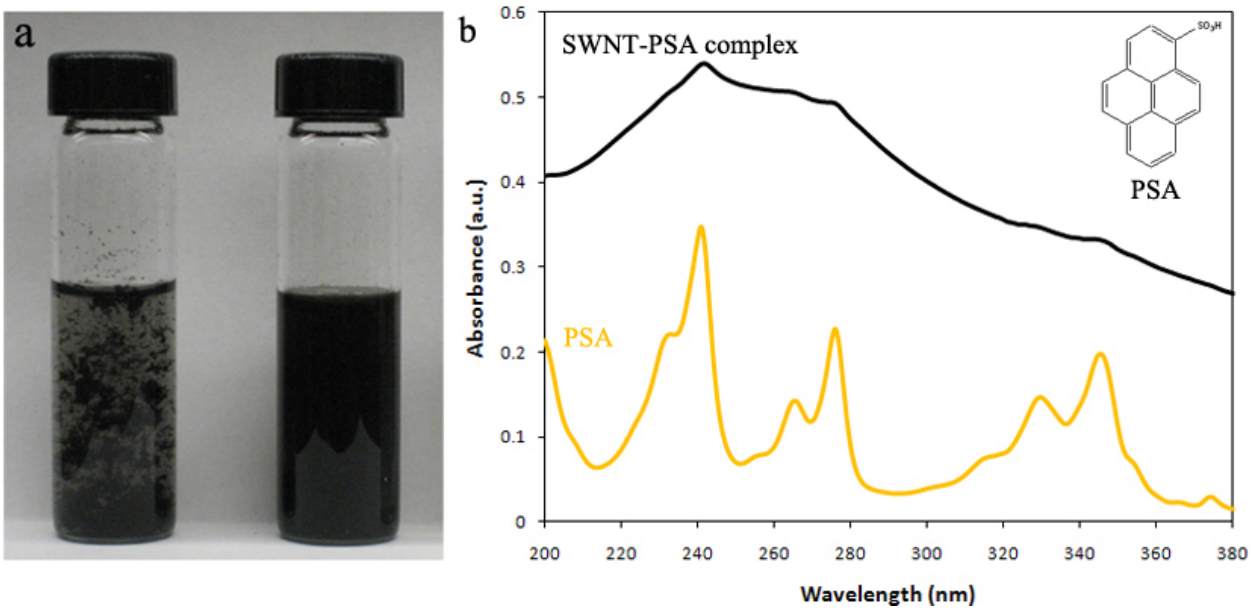

Figure 2-4. Noncovalent functionalization of SWNTs. (a) Digital photographs of aqueous suspensions of pristine SWNTs (left vial) and PSA-functionalized SWNTs (right vial). (b) UV-vis absorption spectra of 1-pyrenesulfonic acid (PSA) and PSA-functionalized SWNTs in water. SWNT-PSA complex shows broad PSA peaks even after three consecutive washes by water, indicting a strong binding between PSA and SWNTs. The broadening of the peaks is probably due to the π-π interaction between PSA pyrene moiety and SWNTs sidewalls. Inset depict the molecular structure of PSA.

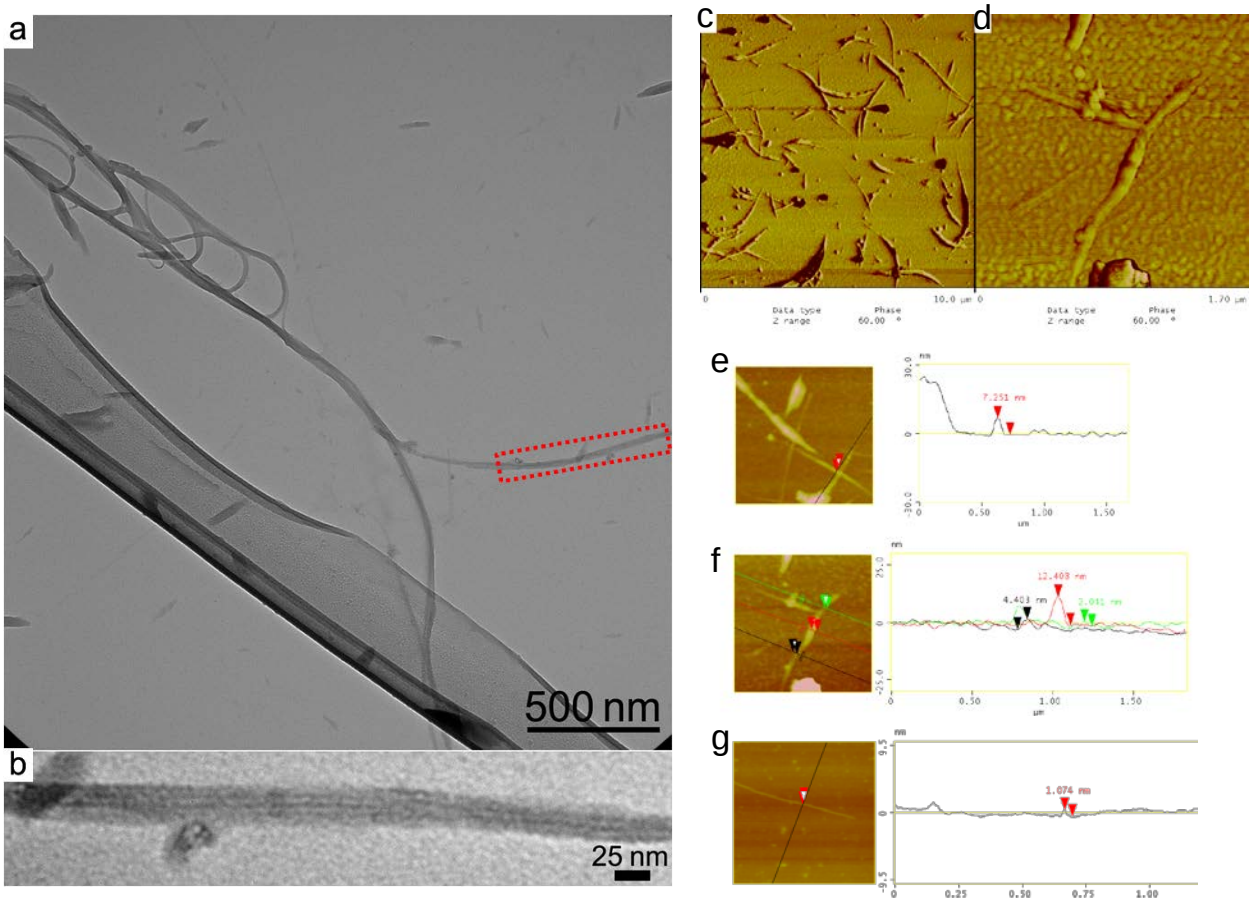

Figure 2-5. Additional microscopic characterization of the core/shell structure. (a) TEM image of SWNT@PAni core/shell hybrid nanostructures (b) is a higher resolution image of the selected area in (a). (c, d) Typical AFM phase images of SWNT@PAni. (e, f) Cross section analysis of two SWNT@PAni, the height of ~ 7-12 nm suggests successful PAni coating. (g) Cross section analysis of a SWNT-PSA before PAni polymerization reveals the height of ~ 1 nm which is characteristic of SWNT diameter.

As comparison, i*n situ* polymerizations of aniline monomer were also carried out with different types of SWNTs: pristine SWNTs and oxidized SWNTs (o-SWNTs). Figure 2-6a shows the composite morphology after the *in situ* polymerization of aniline in a DMF suspension of pristine SWNTs - utilizing a same synthetic condition reported for PAni NFs.[140] Despite the homogeneous suspension of SWNTs in DMF, the resulting SWNT-PAni composite appeared as large aggregates. We believe that aggregation was caused by the dopant agent (HCl), which, upon addition, causes the aggregation of SWNTs in the mixture before polymerization, as observed in the control experiments. We then performed the polymerization without adding acidic dopant in the same SWNTs suspension. Although SWNTs remained largely debundled, under such conditions, the rate of polymerization was suppressed, and only PAni nanoparticles were observed on the SWNT sidewalls, as shown in Figure 2-6b. In another approach, SWNTs were first oxidized to induce oxygen-containing surface functionalities (e.g., hydroxyl and carboxylic groups) before being used as templates in the polymerization. The introduction of oxygen containing groups was expected to not only result a better solubility of SWNTs, but also provide link sites for the polymer on the SWNT surface. Examples using nanotube with carboxylic functionalities in the composite synthesis could be found for both MWNTs[149] and SWNTs.[145] Figure 2-6c demonstrates the result of using o-SWNTs during the aniline polymerization. The rough edges of the products suggested a PAni coating outside individual o-SWNTs, giving a core/shell nanostructure. However, this material was later found to be non-conductive, which could be caused by the damages to the graphitic surface of SWNTs from the oxidation reaction. Compared with the previously reported o-SWNT/PAni composites that were conductive and incorporated into the resistors,[145] our results showed that the degree of the

carboxylic functionalities was an important factor and should be carefully controlled in future applications.

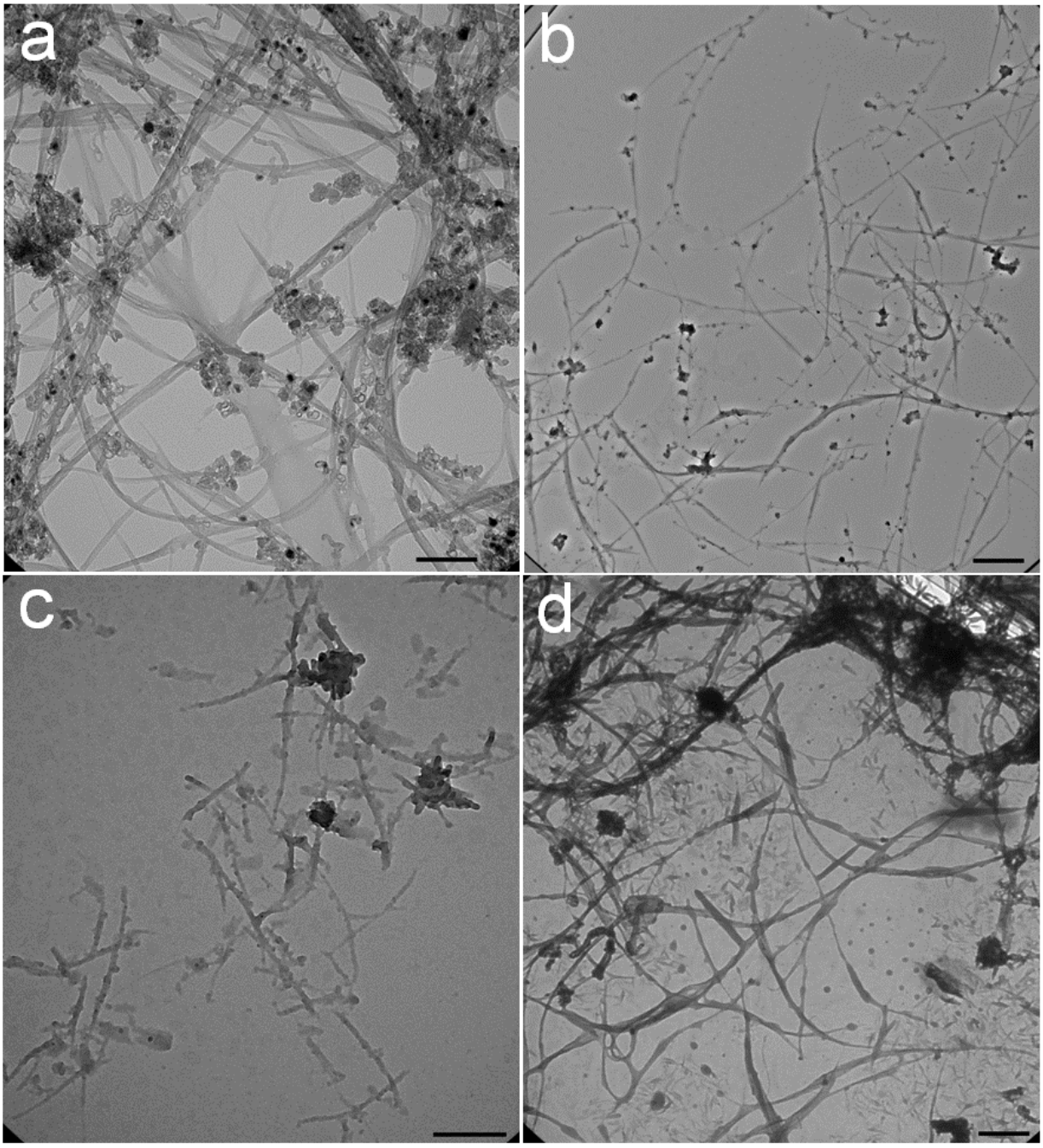

Figure 2-6. TEM images of different SWNT-PAni hybrid systems. (a) SWNT-PAni bulk mixture. (b) SWNTs functionalized with PAni nanoparticles. (c) PAni coated oxidized SWNTs. (d) SWNT@PAni core/shell hybrid nanostructures.

2.4.2 Chemical Sensitivity and Stability of SWNT@PAni - a Positive Synergy

Chemical sensitivity of different SWNT-PAni hybrid systems were explored to probe the influence of morphology on the properties of the hybrid nanomaterials. Acetone was firstly employed as a target analyte here, and the acetone sensitivity of bare SWNTs and pure PAni NFs were tested as comparisons to the SWNT-PAni materials. As shown in Figure 2-7a, SWNTs experienced a decrease in their conductance upon exposure to acetone vapors, while PAni NFs had an increase. PAni NFs had better acetone sensitivity compared to SWNTs, and their response was saturated at the tested concentrations. Different SWNT-PAni hybrid systems showed improved acetone sensitivity in general as compared to bare SWNTs (Figure 2-7b). Moreover, for the SWNT@PAni core/shell nanohybrids, there was about one order of magnitude increase in the acetone response over SWNTs (Figure 2-7c), which was also significantly larger compared with other SWNT-PAni composites. This result indicates that the controlled core/shell morphology could result in a superior enhancement of the chemical sensitivity of the hybrid materials.

Acetone sensitivity of SWNTs was previously explained by charge transfer between adsorbed acetone molecules and SWNTs, which is a weak interaction unless defects are present on SWNTs surface.[150] Therefore bare SWNTs have relatively small response to acetone vapors. PAni NFs, on the other hand, demonstrate high acetone sensitivity because of the polymer swelling when the backbone nitrogen atoms are interacting with acetone molecules, which causes large changes in their electric properties.[141] We hypothesize that PAni shell swelling in acetone vapors has consequent effect on the electrical conductivity of SWNT core. This effect is more significant than charge transfer in SWNTs and results in increased acetone sensitivity of SWNT@PAni core/shell fibers.

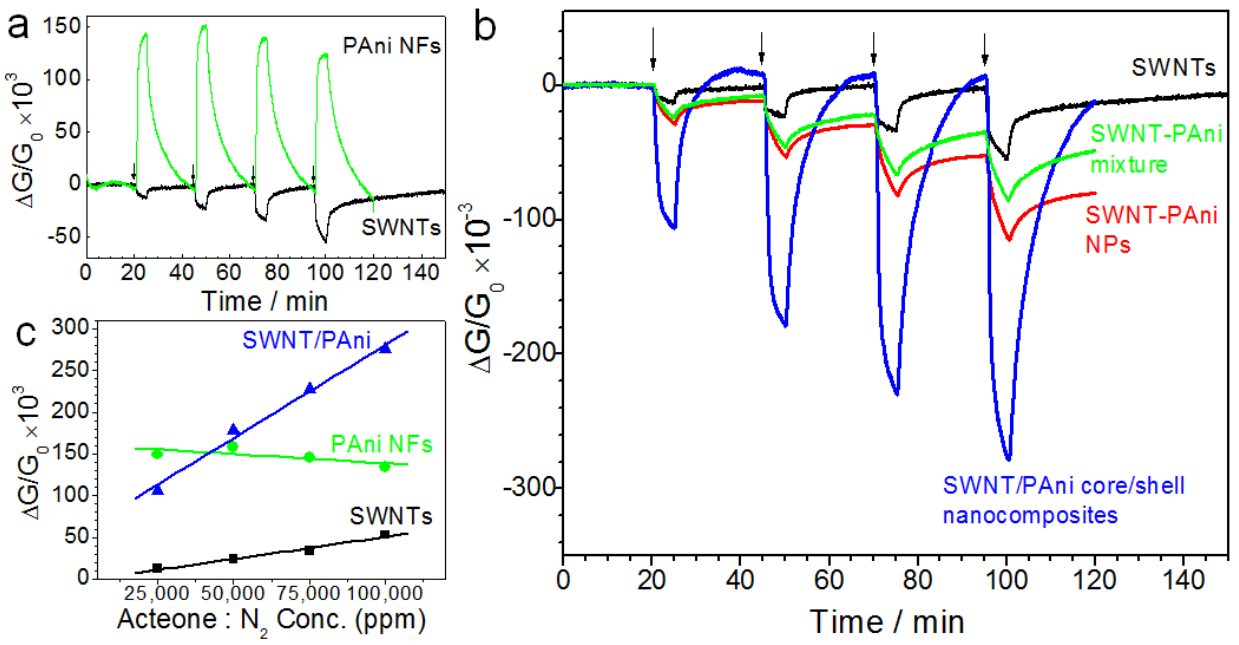

Figure 2-7. Relative conductance changes of SWNTs, PAni nanofibers (NFs), and different SWNT-PAni composites upon exposure to four acetone vapor pulses (25,000, 50,000, 75,000 and 100,000 ppm in N_2). (a) Relative conductance changes of bare SWNTs and PAni NFs, arrows indicate beginning of acetone exposure (5 min). (b) Relative conductance changes of bare SWNTs, SWNT-PAni mixture, SWNT-PAni nanoparticles and SWNT@PAni core/shell nanocomposites, arrows indicate beginning of acetone exposure (5 min). (c) Calibration curves of different sensors. $\Delta G/G_0$ is the change in conductance (G) normalized to the initial conductance (G_0) before vapor exposure.

The electrical response of SWNT@PAni nanohybrids to other chemicals, including ammonia (NH_3), hydrogen sulfide (H_2S), acetic acid (AA) and hydrazine (N_2H_4), was further explored and compared with that of pristine SWNTs and PAni NFs, as shown in Figure 2-8. We chose to study the sensitivity of SWNT@PAni to these chemicals for two reasons. First, they are known to induce charge transfer effects to both SWNTs[151] and PAni.[141] Second, their detection is practically important in industrial monitoring, personal safety and medical field. For example, N_2H_4 is a highly toxic and explosive chemical - a common component of rocket fuels.

PAni has been reported to be an excellent acid/base sensor because of its reversible acid/base doping process.[141] Moreover, its composites with metal salts showed ultrasensitivity to hydrogen sulfide (H_2S).[152] As shown in Figure 2-8a, SWNT@PAni demonstrated a similar response to acid or base analytes, with an increase in conductance to AA vapor and a decrease in conductance to NH_3 gas. We also incorporated $CuCl_2$ into SWNT@PAni[152] and tested the composite with H_2S. As shown in Figure 2-8c, SWNT/PAni has a very weak response to 500 ppb H_2S, which is comparable to bare SWNTs. When treated with Cu(II) salt, SWNT/PAni showed a significant increase in the H_2S sensitivity, similarly to what was reported for PAni/$CuCl_2$.[152]

SWNT@PAni further demonstrated a significant decrease in conductance upon exposure to N_2H_4, similar to PAni NFs (Figure 2-8d). Although the response of SWNT@PAni was not greater than that of PAni NFs, the composite had an advantage of a recovery and thus could be used for multiple vapor exposures. The recovery of SWNT@PAni sensor conductance during allowed time (30 min) was incomplete, and resulted in smaller responses for the consecutive N_2H_4 exposures. It should be emphasized here that the SWNT@PAni sensor can fully recover to the baseline conductance in air overnight. Pristine SWNTs demonstrated a decrease in conductance at the first N_2H_4 exposure, and a progressing increase for the following exposures.

This difference in both direction and magnitude of response to identical analyte concentrations may be a consequence of irreversible change in SWNT conductivity. In fact, N_2H_4 has been demonstrated[151] to induce electron doping effect and transform p-type SWNTs to n-type. Such a change in the main carriers makes SWNTs unsuitable to detect N_2H_4 in a predictable fashion, which is required for sensors. This problem does not exist in SWNT@PAni due to the presence of the PAni shell. However, the polymeric coating may be responsible for slowing down the sensor recovery compared to pristine SWNTs. In a short conclusion, the combination of SWNT and PAni leads to a unique redox behavior of SWNT@PAni and makes it a good candidate for N_2H_4 sensing, which cannot be achieved by either PAni NFs or SWNTs.

The chemical stability of SWNT@Pani is an advantage in comparison to bare SWNTs or PAni NFs. Figure 2-8e depicts the monitoring of the baseline conductance of the SWNT@PAni and the PAni NFs during continuous N_2H_4 tests over the course of four months. While PAni NFs lost their conductivity after the first exposure with no visible recovery, SWNT@PAni responded reversibly for four months of testing (Figure 2-8e, also see Figure 2-9). The limited life time of PAni sensor to N_2H_4 is most likely due to the irreversible nature of the reduction of PAni with N_2H_4.[141] However, for the SWNT@PAni, the PAni shell is in contact with the SWNT core, therefore the SWNT can presumably withdraw electrons from the reduced PAni shell, causing the recovery of the sensor. Similarly, longer life time of SWNT@PAni devices over PAni NFs was observed in ambient conditions.

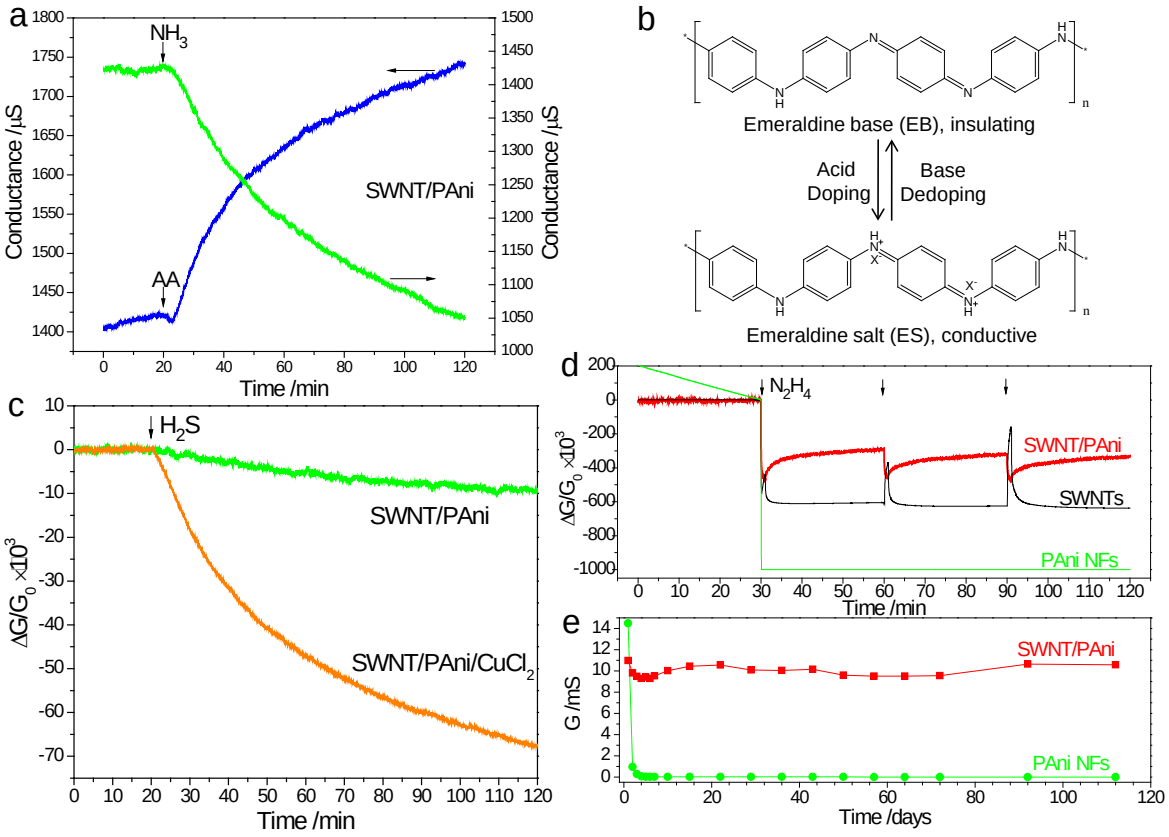

Figure 2-8. Chemical sensitivity of SWNT@PAni. (a) Conductance changes of SWNT@PAni upon exposure to 300 ppm acetic acid (AA) (blue curve) and 100 ppm NH_3 (green curve) in N_2, arrows indicate the beginning of exposure. (b) Chemical structures of protonated and corresponding base forms of PAni and their electric conductivity. (c) Conductance (G) changes of SWNT@PAni and SWNT@PAni/$CuCl_2$ upon exposure to 500 ppb H_2S in N_2, arrow indicates the beginning of H_2S exposure. (d) Conductance (G) changes of SWNTs, PAni NFs and SWNT@PAni upon exposure to three N_2H_4 pulses (saturated vapors in air), arrows correspond to the point when N_2H_4 was introduced (1 min). (e) Comparison of SWNT@PAni and PAni NFs performance (baseline conductance) over period of four months, each point corresponds to one N_2H_4 test (10 min exposure) on different days.

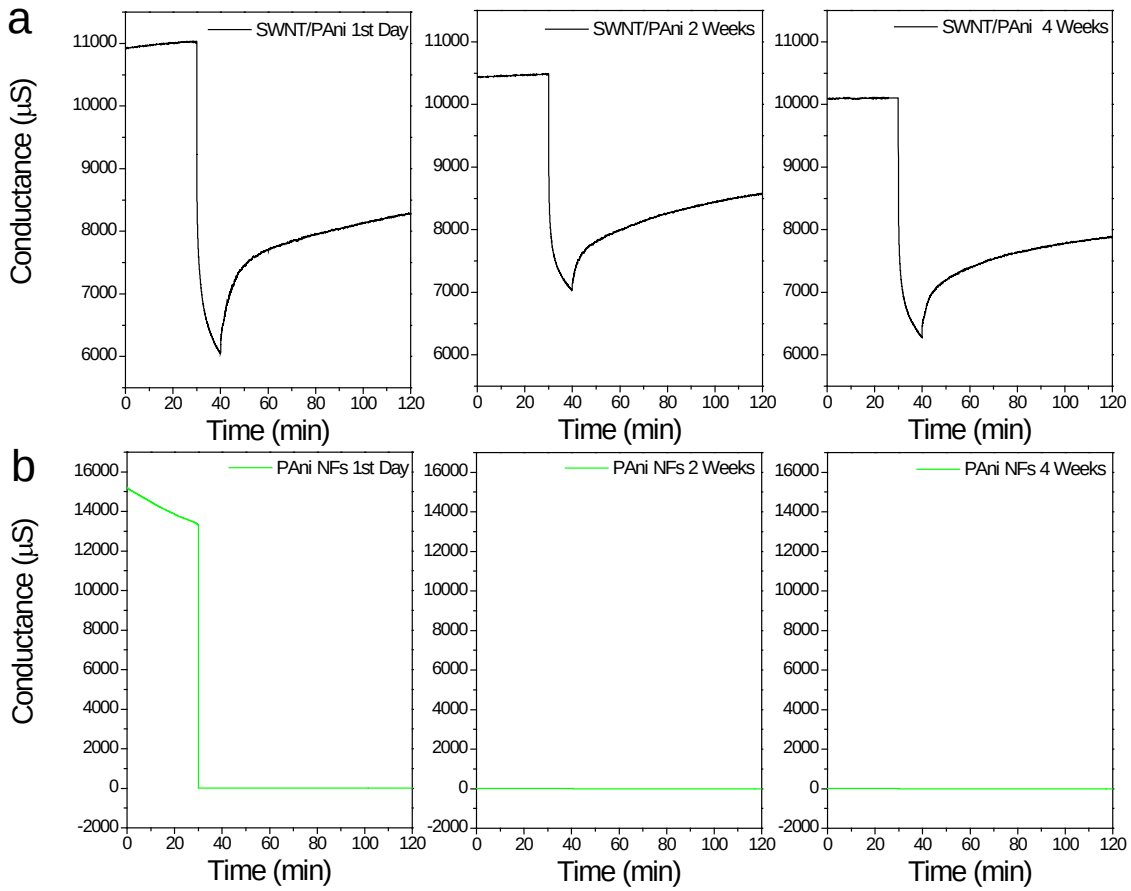

Figure 2-9. Comparison of SWNT@PAni and PAni NFs performance over period of four weeks: detection of hydrazine (N_2H_4, saturated vapors in N_2) over period of four weeks with (a) SWNT@PAni and (b) PAni NFs. Whereas PAni NFs showed irreversible response to the first exposure to N_2H_4, response of SWNT@PAni was reproducible during the time period tested.

The advances in the sensitivity and stability of SWNT@PAni enabled the reversible detection of hydrazine vapors. Hydrazine is commonly used as a hypergolic fuels in the spacecraft by the National Aeronautics and Space Administration (NASA) and the United States Air Force (USAF), yet it is also a highly toxic and explosive chemical. Therefore, detection of trace concentrations of hydrazine vapors is practically important for the safety issue in aerospace. As shown in Figure 2-10, the SWNT@PAni device deomstrated a significant decrease in conductance when exposed to parts-per-billion (ppb) concentrations of hydrazine vapors. Compared with the reported chemiresistor hydrazine sensors based on pure conducting polymer, the reponse of SWNT@PAni was reversible and could thus lead to sensor devices for continous detection and long-time monitoring of trace hydrazine vapors in the specific working environment.

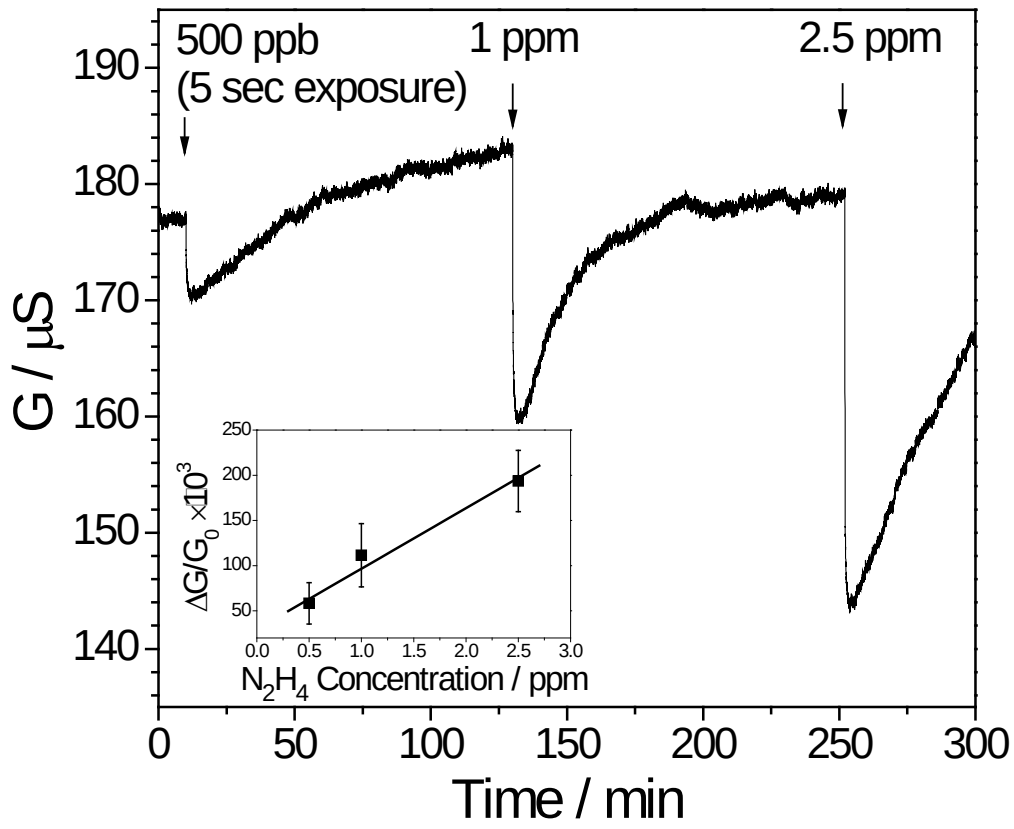

Figure 2-10. Room-temperature, rapid and reversible detection of trace hydrazine vapors. Conductance (G) changes of a typical SWNT@PAni device upon exposure (5 sec) to three hydrazine vapor pulses (0.5, 1 and 2.5 ppm in N_2). Inset depicts the three-point calibration curve of the hydrazine sensor.

2.4.3 Electronic Interactions Between Core and Shell in the SWNT@PAni Hybrid System

The proposed electron transfer between core and shell in SWNT@PAni was further elucidated by electrochemical measurements. Figure 2-11 shows the cyclic voltammograms (CVs) of pristine SWNTs, PAni NFs and SWNT@PAni, within the potential window from −0.2 to +0.8 V (vs. a Ag/AgCl reference electrode). Only one pair of redox peaks was observed for the SWNTs electrode, corresponding to the transition between quinone/hydroquinone states of oxygen-containing functional groups on SWNTs.[153] For the PAni NFs electrode, two pairs of redox peaks (C_1/A_1 and C_2/A_2) were observed, which can be attributed to the redox transitions of leucoemeraldine/emeraldine and emeraldine/pernigraniline, respectively (Figure 2-11b).[154-155] SWNT@PAni showed significantly different CV characteristics compared to that of PAni NFs, as only one pair of redox peaks was observed corresponding to the transition of the PAni shell between leucoemeraldine/emeraldine forms (peaks C_1/A_1). The absence of emeraldine/pernigraniline transition peaks (C_2/A_2) indicates the transformation between these two oxidation states of the PAni shell was inhibited by the SWNT core in the tested potential range. Such inhibition can be rationalized by the electronic interactions between the SWNT core and the PAni shell in the composite, which consequently changes the chemical potential of the PAni shell as well as the energy barrier between different oxidation states. Moreover, peaks C_1/A_1 (leucoemeraldine/emeraldine) of SWNT@PAni can be considered an ideal reversible electrode process compared to the same peaks of PAni NFs. Since the electrical response of PAni sensors comes from the reduction of emeraldine to leucoemeraldine by N_2H_4,[141] the observed increased reversibility for this redox pair (C_1/A_1) can be correlated with the sensor reversibility of the SWNT@PAni as compared to PAni NFs.

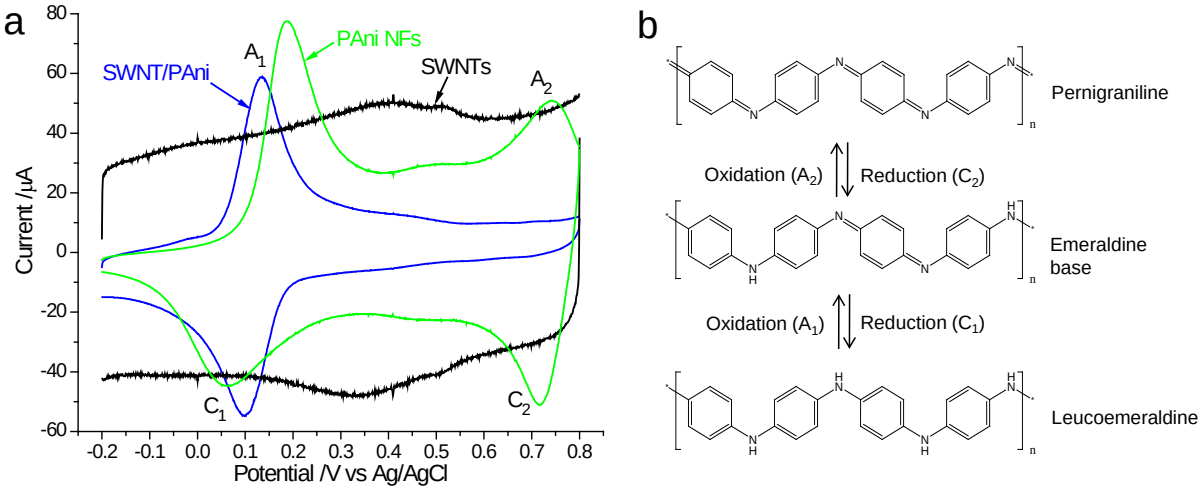

Figure 2-11. Electrochemistry of SWNT@PAni. (a) Cyclic voltammograms (CVs) of pristine SWNTs, PAni NFs and SWNT@PAni in 0.5 M H_2SO_4, within potential window -0.2 to 0.8 V (vs. Ag/AgCl) at scan rate of 100 mV s^{-1}. (b) Three oxidation states of PAni.

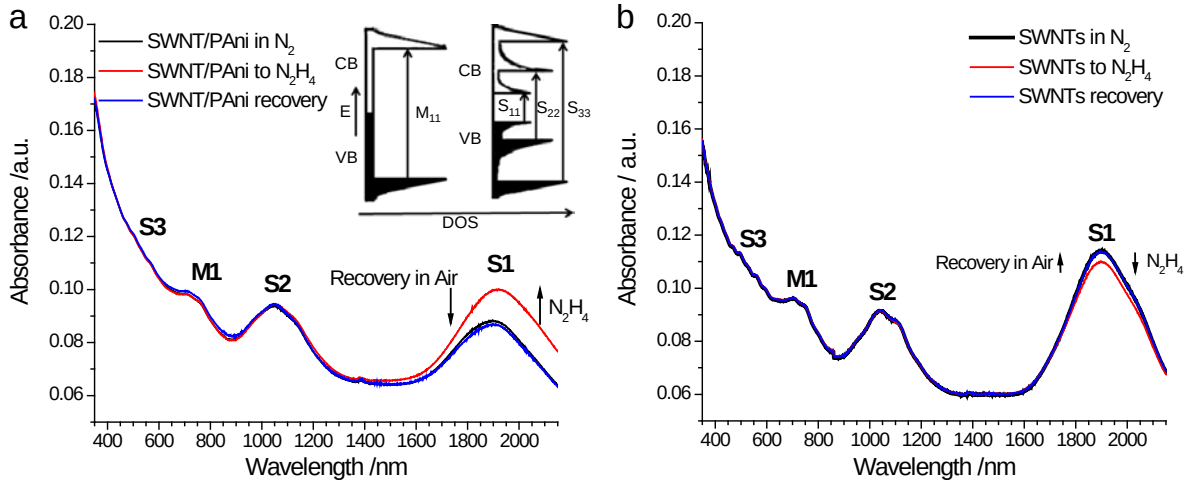

Figure 2-12. Spectroscopic investigation of the electronic interactions in the SWNT@PAni hybrid system. UV-vis-NIR absorption spectra of (a) SWNT@PAni film and (b) pristine SWNTs film: before (black), after (red) exposure to hydrazine vapors and recovery in air (blue). Inset in (a) depicts a density of states (DOS) diagram of metallic and semiconducting SWNTs showing their transition bands.

The electronic interactions between the PAni shell and the SWNT core during N_2H_4 detection were further studied by optical spectroscopy. UV-vis-NIR absorption spectra is a useful characterization tool to probe any electron transfer within SWNTs[30, 47, 156-157] as they have unique electronic structures with several van Hove singularities in their density of state (DOS).[46] The electronic transitions between these singularities in the conduction band (CB) and valence band (VB) of SWNTs result in absorption bands in the UV, visible and NIR regions. Semiconducting SWNTs typically show three transition bands, S_{11}-S_{33}, and metallic SWNTs show one M_{11} band (as shown in Figure 2-12 inset). The S_{11} band is most sensitive to the charge transfer effect on SWNTs since it corresponds to the states at the top of the VB, and monitoring changes in SWNT S_{11} band has been proven successful in many studies of electronic interactions that involved SWNTs.[30, 47, 154-155] Figure 2-12a shows the absorbance spectra of a SWNT@PAni film. The spectra revealed only typical SWNTs absorbance bands, as the absorbance of PAni at 350 − 400 nm was covered by the strong absorbance of SWNTs in thin films. Upon exposure to N_2H_4 vapors, S_{11} peak of SWNT core was increased 13% with a red shift (24 nm), indicating the electron donations to SWNTs. The increase in S_{11} absorbance of the SWNT core in composite is different from what was observed in pristine SWNTs, which show 4% decrease in the S_{11} absorbance upon N_2H_4 exposure (Figure 2-12b). This indicates the specific electronic interaction between the SWNT core and the PAni shell. S_{11} bands of both SWNT@PAni and SWNTs readily recovered to the initial values when N_2H_4 was turned off and the thin films were left in air (Figure 2-12). The recovery of the S_{11} band had similar time dependence as the recovery of electrical conductance of SWNT@PAni composite based devices.

From the above results, we can conclude that the SWNT core can interact effectively with the PAni shell and facilitate the electron transfer processes. In the oxidizing environments,

the SWNT core can donate electrons to the PAni shell and effectively increase the energy barrier to the oxidation between emeraldine and pernigraniline forms, as evident from CV experiments. In the reducing environment (upon N_2H_4 exposure), SWNT core can facilitate the transition between emeraldine/leucoemeraldine forms of PAni. This makes SWNT@PAni composite sensing of N_2H_4 reversible, as evident from solid-state conductivity measurements and UV-vis-NIR absorbance spectroscopy.

2.5 CONCLUSION

In summary, noncovalent functionalization of SWNTs with PSA is a simple and scalable method for the synthesis of SWNT@PAni hybrid nanostructures with controlled core/shell morphology. The delicate combination of SWNT and PAni resulted in unique electronic interactions between the SWNT core and the PAni shell. The unique chemical behavior of the SWNT core and the PAni shell has positive synergistic effects on chemical detection. Our chemical sensing tests demonstrated that SWNT@PAni composite has better sensitivity and stability than either SWNTs or PAni NFs, and thus holds a great promise for real-world sensor applications.

3.0 SELF-ASSEMBLY AND NANOWELDING OF GOLD NANOPARTICLES ON GRAPHITIC TEMPLATES FOR CHEMICAL SENSING

3.1 CHAPTER PREFACE

Part of the materials contained in this chapter was published as a research article in *the Journal of the American Chemical Society*; figures used in this chapter have been reprinted with permission from *J. Am. Chem. Soc.* **2012**, *134*, 3472-3479. (listed as reference 14 in bibliography section). Copyright 2012 American Chemical Society.

List of Authors: Mengning Ding, Dan C. Sorescu, Gregg P. Kotchey and Alexander Star.

Author Contributions: DMN and AS designed the experiments and wrote the manuscript, DMN performed experimental work, DCS performed computational modeling, and GPK synthesized all the graphene samples.

3.2 INTRODUCTION

The bottom-up synthesis of complex architectures from nanoscale building blocks is a fascinating approach to achieve novel materials with unique structures and functions; yet this process remains extremely challenging because it requires careful and delicate control of the building blocks at molecular level.[158-160] One representative example involves the fabrication of one-dimensional (1-D) gold nanowires (AuNWs) from zero-dimensional (0-D) gold nanoparticles (AuNPs), which have been extensively studied due to their potential applications in electronics,[161-162] photonics[163] and sensors.[164] The difficulty with this system arises from the need to precisely place and interconnect individual nanoparticles in a confined dimension.[165-166] Successful bottom-up fabrication of AuNWs has been accomplished through an "oriented attachment" method,[167-169] where recognition of the anisotropic lattice and the reduction of surface energy played an essential role.[170-171] The welding of gold at the nanoscale was another approach for the bottom-up construction of gold nanostructures. Since this method does not require the templating of strong binding surfactants such as oleylamine (OAm), it is favorable for the fabrication of catalysts and chemical sensors. The welding of gold nanostructures has been successfully implemented by a number of methods such as laser heating,[172] Joule heating[173] and cold welding.[174] Combining nanowelding with self-assembly of AuNPs provides another promising bottom-up strategy for the fabrication of AuNWs from AuNPs; one example of such a strategy has been successfully demonstrated by Belcher and co-workers utilizing biological templates.[175]

Progresses made on controlled fabrication of Au nanostructures will significantly benefit the development of chemical sensors. Au has been used as chemical sensors for decades[176] because of its chemical inertness and high conductivity, which changes upon adsorption of different molecules. Hydrogen sulfide (H_2S), for example, has been detected using Au thin film,[177] AuNPs,[178] and most recently AuNPs decorated carbon nanotubes (CNTs).[179] Despite the excellent sensitivity achieved by AuNPs for H_2S, there has been minimal advance in the development of H_2S sensors based on AuNWs. 1-D nanostructures have been considered to be an ideal sensor architecture as a result of their comparable Debye length to cross-sectional radius;[129, 136] therefore, it is of great interest to explore the H_2S sensitivity of 1-D AuNWs.

We report a bottom-up approach for the synthesis of AuNWs using AuNPs as building blocks in aqueous suspension of single-walled carbon nanotubes (SWNTs). Citrate stabilized AuNPs first underwent a 1-D self-assembly process enabled by 1-pyrenesulfonic acid (PSA) decorated SWNT templates, and AuNWs were subsequently formed through a nanowelding process of aligned AuNPs induced by thermal heating. In addition to performing control experiments with different graphitic templates, we used density function theory (DFT) calculations to understand the underlying mechanism of the entire self-assembly and nanowelding processes. We further demonstrated the use of AuNW-SWNTs hybrid material for sensitive and selective detection of H_2S gas. With ultrasensitivity to H_2S at concentrations as low as parts-per-billion (ppb) and no obvious cross-sensitivity towards major components of natural gas and human breath, we established potential applications of this material as an industrial sensor for personal safety and human breath detection.

3.3 EXPERIMENTAL SECTION

Materials: Pristine single-walled carbon nanotubes (SWNTs, P2) and carboxylated single-walled carbon nanotubes (SWNT-COOH, P3) were obtained from Carbon Solutions Inc. 1-Pyrenesulfonic acid hydrate (1-PSA, $C_{16}H_{10}O_3S{\cdot}xH_2O$), 1-pyrenecaboxylic acid (1-PCA, $C_{17}H_{10}O_2$, 97%), gold(III) chloride trihydrate ($HAuCl_4{\cdot}3H_2O$, 99.9+% trace metals basis), sodium borohydride ($NaBH_4$) and all organic solvents were purchased from Sigma Aldrich and used as received. Sodium citrate dihydrate was acquired from Mallinckrodt Baker Inc., and 40 lead ceramic sidebraze (CERDIP) packages (cavity .310 × .310) were procured from Global Chip Materials, LLC.

Preparation of different graphitic templates:

PSA/PCA Functionalized SWNTs (SWNT-PSA/SWNT-PCA):[13] SWNTs powder (5.0 mg) was sonicated in DI water (10 mL) with a Branson 5510 bath sonicator for 15 minutes to obtain a temporary SWNTs suspension. Aqueous solution of 1-PSA or methanol solution of 1-PCA (10 mL, 0.5 mg/mL) was added into this SWNTs suspension following by sonication for 30 minutes. The resulting SWNT-PSA/SWNT-PCA complex was separated out by centrifugation and washed with DI water for three times to afford the final product which was resuspended in 20 mL of DI water.

Sulfonated SWNTs (S-SWNT): Pristine SWNTs were oxidized with nitic acid and sulfuric acid (1:3) following reported procedure.[147] The oxidized SWNTs (5.5 mg) were then suspended in water (7.5 mL) and sulfonated with aryl diazonium salt of sulfanilic acid followed by a hydrazine reduction for 24 hr, similar to a previous publication.[180] Cautions should be taken

when using hydrazine due to its toxicity. The final product was filtrated, washed with DI water for three times, and was finally suspended in 20 mL of DI water.

Graphene Oxide (GO) and Chemically Converted Graphene (CCG): Utilizing a modified Hummers' method, graphite oxide was prepared on graphite flakes that underwent a preoxidation step.[181] Graphene oxide (~ 0.125 wt%) was subsequently formed from graphite oxide that was diluted 1:4 with double distilled water, exfoliated for 45 minutes by sonication, and centrifuged for 30 minutes at 3400 revolutions per minute (r.p.m.) to remove unexfoliated graphite oxide. To form chemically converted graphene (CCG), graphene oxide was reduced following a modified procedure.[180] Briefly, the pH of a dispersion of graphene oxide (75 g) in water was adjusted to approximately 9 with sodium carbonate, and the graphene oxide dispersion was partially reduced through the addition of sodium borohydride (600 mg). After heating the partially reduced graphene oxide dispersion at 80°C for 1 hour under constant stirring, the material underwent four sequential washing/centrifugation cycles, and the partially reduced graphene oxide was dispersed in water via mild sonication for a final mass of 75 g. Finally, the dispersion of partially reduced graphene oxide was reduced by hydrazine. To this end, 50 wt% hydrazine hydrate (4 g) were added to the dispersion of partially reduced graphene oxide, which was subsequently refluxed at 100°C for 24 hours under constant stirring. After refluxing, the CCG was subjected to four sequential washing/centrifugation cycles.

PSA and PCA Functionalized CCG (CCG-PSA & CCG-PCA): CCG-PSA and CCG-PCA were synthesized using the same method for the synthesis of SWNT-PSA and SWNT-PCA.

Sulfonated Chemically Converted Graphene (S-CCG): S-CCG was synthesized using the same method for the synthesis of S-SWNTs.

Self-assembly and Nanowelding of Gold Nanoparticles:

Using SWNT-PSA Template (Synthesis of AuNW-SWNTs): $HAuCl_4$ (5.0 mg) was dissolved in an aqueous suspension of PSA-functionalized SWNTs (19 mL, 0.025 mg/mL). An aqueous solution of sodium citrate (1 wt%, 1 mL) was then added into $HAuCl_4$ and SWNT-PSA solution with vigorous stirring. The mixture solution was heated to 100°C for 30-120 min to yield a purple suspension of SWNTs. The final product was isolated by centrifugation and washed with DI water for several times, and then resuspended in 20 mL of DI water. Control experiments were done under similar conditions without the presence of carbon nanotubes in the solution.

Using Other Graphitic Template: Self-assembly and nanowelding process on other graphitic templates (including SWNT-PCA, SWNT-COOH, S-SWNTs, GO, CCG-PSA, CCG-PCA and S-CCG) were carried out with a same procedure to that of SWNT-PSA template.

Electrical and Chemical Sensing Tests:

Sensor Device Fabrication: Si chips with 300 nm thermal oxide layer and interdigitated gold electrodes were purchased from MEMS and Nanotechnology Exchange. The devices were fabricated by drop-casting aqueous suspension (10 μL) of AuNW-SWNTs or DMF suspensions (70 μL) of SWNTs onto the Si chips which were connected to the 40 CERDIP Packages with Au wires and allowed to dry in ambient.

Gas Sensing Measurements: Gas sensing measurements were carried out using a custom-made system that has been described in our previous publications.[121] In particlular, electrical conductance of 2 chips (with 8 data output) can be measured on a test board by Keithley Dual SourceMeter 2602 and Keithley Switching Matrix 708A, controlled by a Zephyr Measurement Software (http://zephyr.sourceforge.net). A custom-built Teflon chamber was used to control the gas environment during the sensing test. Different concentrations of analyte gases were

generated by mixing certified gases (100 ppm H_2S in N_2 or 1ppm H_2S in N_2, purchased from Valley National Gas, Inc.) with dry N_2 and were passed through the gas chamber containing the sensor device.

Characterizations:

General Characterizations: Transmission electron microscopy (TEM) of all the synthesized samples was performed on a FEI Morgagni microscope, operating at an acceleration voltage of 80 keV. High resolution TEM (HRTEM) images were obtained on a JEOL 2010F high-resolution transmission electron microscope, operating at an accelerating voltage of 200 keV. Scanning electron microscopy (SEM) was performed with a Phillips XL30 FEG microscope equipped with an energy dispersive x-ray spectroscopy (EDS) accessory. X-ray Diffraction (XRD) was performed with a Philips X'pert diffractometer for powder and thin film diffraction.

Spectroscopic Measurement: UV-vis-NIR absorption spectra studies were carried out on a Perkin-Elmer Lambda 900 UV-vis-NIR spectrophotometer. An Iwata HP-BC Plus airbrush was used to make the thin films for all the solid-state measurements. Specifically, the thin films used in the spectroscopic study were created by spraying a DMF suspension of the desired materials by airbrush onto a quartz plate (1"×1") heated up to 180°C. A custom built Teflon chamber was used to allow the gas flow exposure during spectroscopic measurements.

3.4 RESULTS AND DISCUSSION

3.4.1 Bottom-up Synthesis of AuNW-SWNTs

The formation, assembly and welding of AuNPs were first carried out by an *in situ* citrate reduction of $HAuCl_4$ in a suspension of SWNTs, as illustrated in Figure 3-1a. SWNTs were first functionalized with PSA to form a uniform aqueous suspension[13] in which $HAuCl_4$ was later dissolved. The reduction of $HAuCl_4$ was started by the addition of sodium citrate solution, and the reaction proceeded at a controlled temperature (100 °C) with vigorous stirring.

Transmission electron microscopy (TEM) images (Figure 3-1b) showed the self-assembly of AuNPs on the sidewall of functionalized SWNTs after 30 min from initiation of the reaction. Some nanoparticles already appeared in an elongated shape, and the interconnections between nanoparticles started to form, both of which indicated that the AuNPs started to fuse together under the reaction temperature. This fusion occurred regardless of the presence of SWNTs and could be understood as a nanowelding process of aggregated nanoparticles induced by thermal heating.[182] After a longer reaction time, the nanowelding process resulted in the complete formation of nanowires. The final solution appeared purple in color due to a red shift in the Au surface plasmon resonance (SPR) from AuNPs to AuNWs (Figure 3-1c), which was in accordance with the optical studies on other 1-D Au nanostructures.[173] X-ray Diffraction (XRD) pattern of AuNWs corresponded to a face center cubic (fcc) structure (Figure 3-1d). The fcc structure was also confirmed by high-resolution TEM (HRTEM), as shown in Figure 3-1e, where

the interfringe distances of AuNW lattice were measured to be 0.23 nm, in agreement with (111) lattice spacing for fcc gold.

Compared with usually straight AuNWs that were prepared from confined growth of Au nanocrystals,[161] this self-assembly and nanowelding approach resulted in curved and flexible AuNWs. As can be observed from HRTEM, these AuNWs also exhibited different crystalline areas, which indicated that the nanowires were constructed from multiple building blocks and the assembly was not directed by lattice match as in the case of "oriented attachment".[167-169] Similar results was further observed on a single AuNP and an early stage wire that consisted of a few AuNPs welded together (see Figure 3-2a to c), which provide additional proof for the hypothesis of multiple building blocks. Single crystalline area could also be observed on the AuNWs, as shown in Figure 3-1e (right part of the nanowire, also see Figure 3-2d and e). As the building blocks (AuNPs) were initially polycrystalline, the observation of a single crystalline segment indicated a potential alternation of the crystallinity of these AuNWs. Moreover, multi-walled carbon nanotubes (functionalized with PSA) could also serve as the template for this assembly and nanowelding process (as shown in Figure 3-3). Similar programmable assembly and construction of Au nanostructures was reported from biological templates (genetically engineered viruses).[175] Our results demonstrated that inorganic templates such as SWNT-PSA can be employed in such a bottom-up strategy.

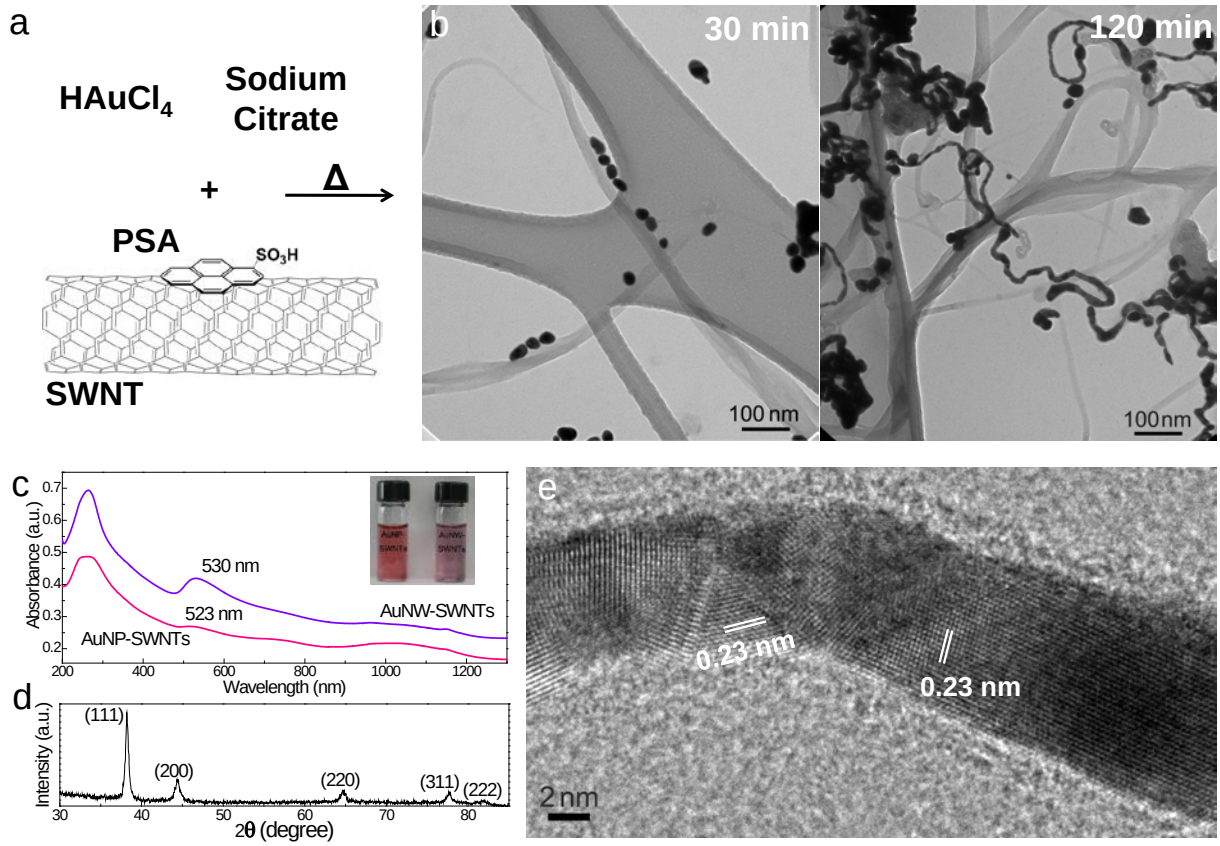

Figure 3-1. Synthesis and characterization of gold nanowires (AuNWs). (a) An aqueous suspension of 1-pyrenesulfonic acid (PSA) functionalized single-walled carbon nanotubes (SWNTs) was used as templates during citrate reduction of chloroauric acid ($HAuCl_4$). (b) TEM images showing the assembly of AuNPs on the SWNTs (after 30 min, left) and their welding into AuNWs (after 120 min, right). (c) UV-vis-NIR absorption spectra of AuNW-SWNTs and AuNP-SWNTs samples. Gold surface plasmon resonance (SPR) shows a red shift with increasing size of gold nanostructures. The inset depicts a digital photo of vials containing suspension of AuNPs and AuNWs (with SWNTs). (d) X-ray diffraction (XRD) pattern of AuNWs. (e) High-resolution TEM image of AuNWs showing the polycrystalline nature of the welded gold nanowires.

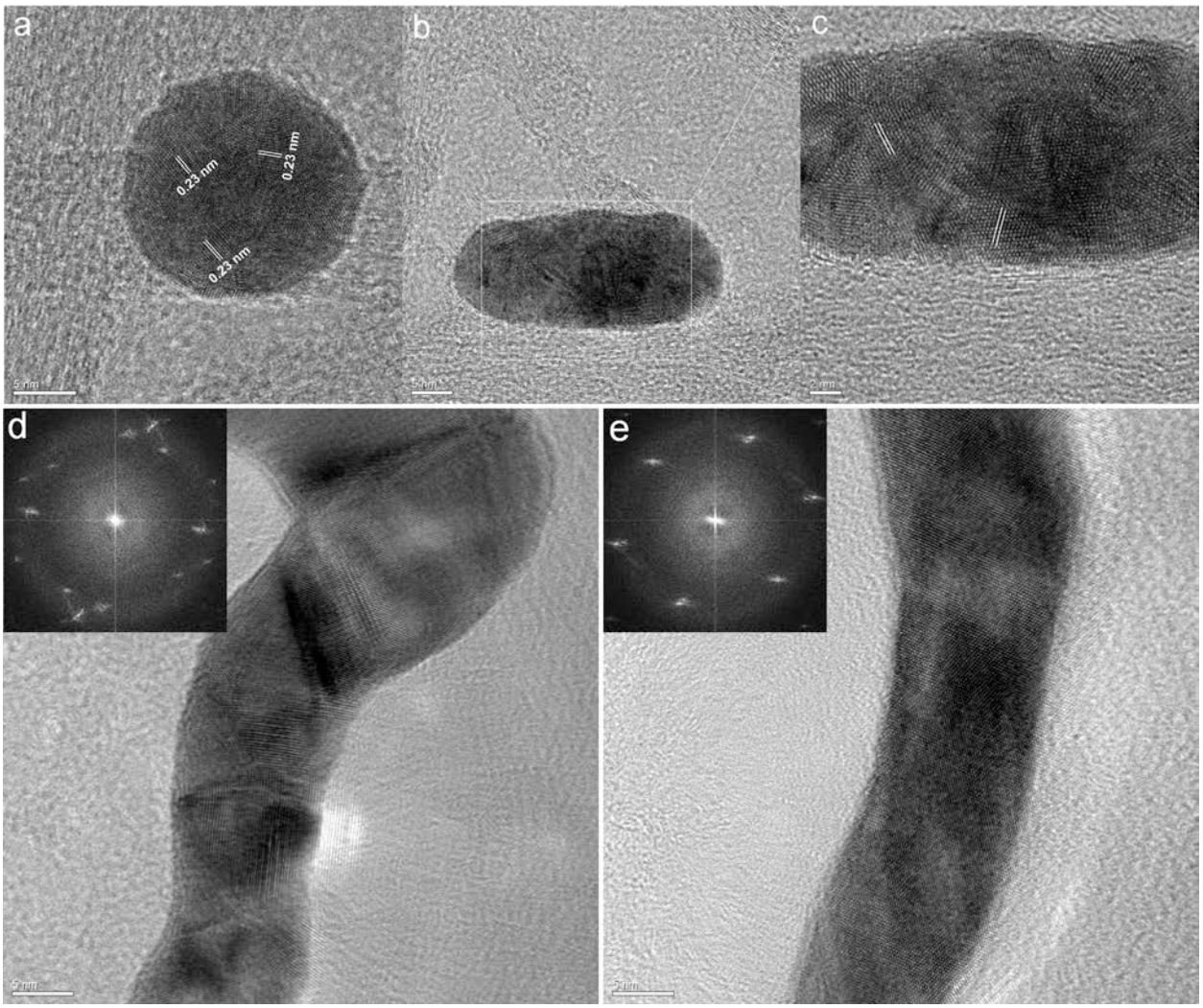

Figure 3-2. HRTEM characterization of AuNPs and AuNWs. HRTEM images of (a) a single gold nanoparticle and (b) three gold nanoparticles welded together. (c) is an enlarged image of the selected area in (b). The interfringe distances in (a) and (c) were measured to be 0.23 nm. (b, c) HRTEM images of gold nanowires synthesized from SWNT-PSA templates with (a) polycrystalline and (b) single crystalline nature. Scale bars are 5 nm.

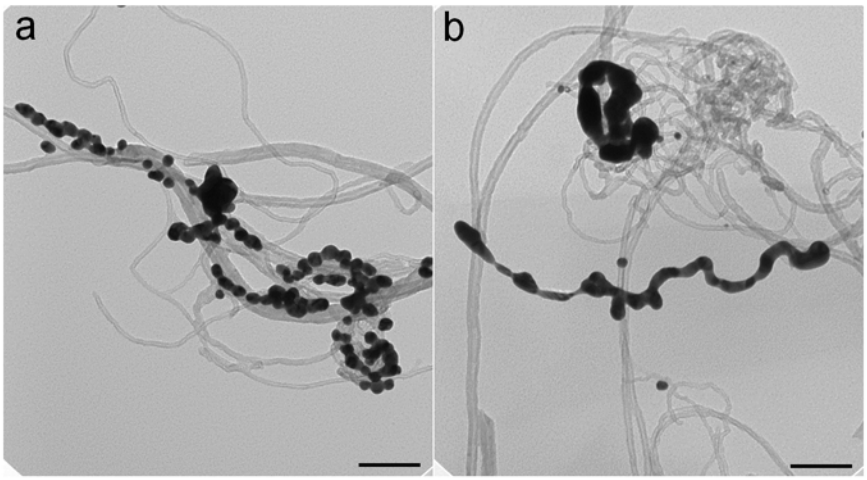

Figure 3-3. MWNT-PSA for the assembly and welding of gold nanoparticles: (a) multiple nanoparticles assembled on the sidewalls of MWNT-PSA; (b) a gold nanowires synthezied after the welding of assembled gold nanoparticles. The resulting nanowires obtained are similar to those obtained using SWNT-PSA templates. Scale bars are 100 nm.

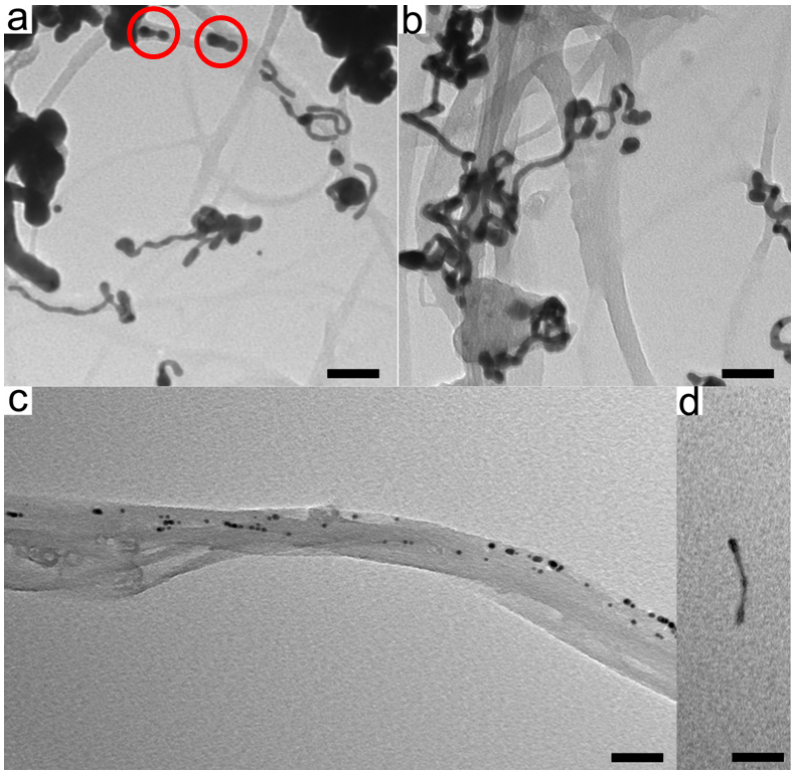

Figure 3-4. Self-assembly and nanowelding of commercial colloidal AuNPs. TEM images of (a) Au nanoparticles (~10 nm) assembled along SWNTs and started to fuse together (in red circles), (b) Au nanowires formed by 10 nm Au nanoparticles, (c) Au nanoparticles (~5 nm) assembled along SWNTs and started to fuse together, (d) Au nanowires formed by 5 nm Au nanoparticles. Scale bars are 50 nm.

3.4.2 Assembly and Nanowelding of AuNPs on Other Graphitic Templates

As the control experiments, $HAuCl_4$ solution was reduced under similar synthetic conditions (−SWNTs, −PSA or +PSA), and only nanoparticles were formed. Without SWNTs in the reaction mixture, AuNWs were not observed regardless of PSA concentration; only aggregates of AuNPs were present (with some of them already fused together).

This observation indicated the necessity of utilizing SWNT template for the formation of nanowire structures. Furthermore, in another control experiment, commercially available gold colloidal solution (Sigma Aldrich) was used as the pre-fabricated building blocks with the SWNT-PSA template; both self-assembly of the nanoparticles and the nanowelding process were observed (Figure 3-4). This result clearly demonstrated that the self-assembly and nanowelding processes do not require *in situ* synthesis of the AuNPs in the system and can be utilized as a general bottom-up approach for the synthesis of 1-D nanomaterials. Our methodology has also been successfully applied for the synthesis of other 1-D nanostructures such as platinum NWs.

The entire self-assembly process, which included adsorption and in-plane diffusion of nanoparticles, was significantly affected by the surface chemistry of both nanoparticles and templates. In order to elucidate such effects, the AuNPs assembly and nanowelding processes were conducted on other graphitic templates, including 1-pyrenecarboxylic acid (PCA) functionalized SWNTs (SWNT-PCA), carboxylated SWNTs (SWNT-COOH, P3, Carbon Solutions, Inc.), sulfonated SWNTs (S-SWNT), as well as 2-D templates, including PSA and PCA functionalized chemically converted graphene (CCG-PSA/CCG-PCA), graphene oxide, and sulfonated chemically converted graphene (S-CCG). By choosing this set of templates, we were adept at exploring the effects of template surface functionalities on the diffusion of AuNPs, which in turn enhanced our understanding of the assembly process.

Although 1-D AuNWs were formed with SWNT-PSA (Figure 3-5a), different products were observed with other templates (Figure 3-5b to h). When employing SWNT-PCA as the template, small aggregates of several nanoparticles were observed after the welding process instead of nanowires, as shown in Figure 3-5b. Although PCA and PSA molecules share a pyrene functionality that is capable of π-π stacking interactions with graphitic surfaces,[148] the presence of carboxylic groups (-COOH) as opposed to sulfonic groups ($-SO_3H$) appear to have prevented the formation of AuNWs. We further probed SWNT-COOH as templates, which have a high degree of carboxylic functionalities, in order to confirm the effect of carboxylic functional groups. Similar to PCA case, only nanoparticles that were attached to the nanotubes were observed (Figure 3-5c).

To further confirm the proposed influence of surface functional groups on the assembly process, S-SWNTs were explored as another template. This material was synthesized through the sulfonation of oxidized SWNTs with an aryl diazonium salt of sulfanilic acid followed by a hydrazine reduction, following a published procedure.[180] S-SWNTs contained both sulfonic and carboxylic groups and had a high solubility in water.[61] As shown in Figure 3-5d, S-SWNT templates led to the formation of an intermediate level product that possessed a few nanowires; most products, however, were aggregated particles. The assembly and welding processes of AuNPs were further explored on 2-D graphene templates. As shown in Figure 3-5e to h, products from CCG-PSA, CCG-PCA, graphene oxide and S-CCG followed the same trends as those observed for SWNTs. CCG-PSA resulted in a full coverage on the graphene after nanowelding (as shown in Figure 3-5e). A number of small gold plates were formed in several confined areas on CCG-PCA (Figure 3-5f) after the welding of small AuNPs aggregates. Furthermore, while

free nanoparticles were observed for graphene oxide templates (Figure 3-5g), an intermediate network of Au nanostructures (Figure 3-5h) was formed using S-CCG as templates.

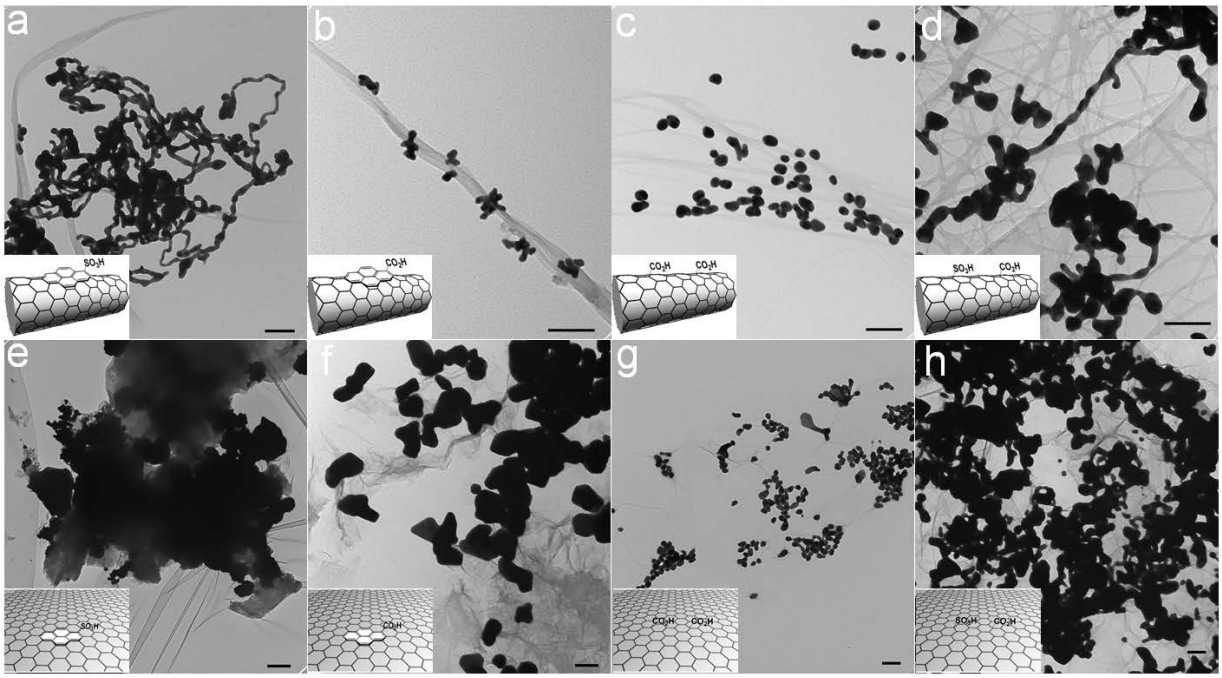

Figure 3-5. TEM images of the products after AuNPs assembly and nanowelding using different graphitic templates. (a) PSA functionalized SWNTs (SWNT-PSA). (b) 1-Pyrenecaboxylate acid (PCA) functionalized SWNTs (SWNT-PCA). (c) Carboxylated SWNTs (SWNT-COOH). (d) Sulfonated SWNTs (S-SWNTs). (e) PSA functionalized chemically converted graphene (CCG-PSA). (f) PCA functionalized chemically converted graphene (CCG-PCA). (g) Graphene oxide. h, Sulfonated chemically converted graphene (S-CCG). Scale bars in (a-d) and (f-h) are 100 nm, scale bar in (e) is 500 nm. Insets are cartoon presentations of the surface functionalizations of the templates.

3.4.3 Mechanistic Understanding of the Assembly and Nanowelding

Computational simulations were employed to provide mechanistic understanding of the self-assembly and nanowelding processes and to rationalize the observed trends of different templates. The proposed self-assembly and nanowelding processes of AuNPs that consists of three mechanistic steps are detailed in Figure 3-6. In the first step, the AuNPs formed in the solution phase and functionalized with citrate molecules adsorbed onto the surface of SWNTs or graphene. In the second step, the adsorbed AuNPs can diffuse on the corresponding graphitic surfaces, and upon meeting, the AuNPs will weld together (third mechanistic step). The net result of these steps renders AuNPs as either 1-D nanowires on the surfaces of SWNTs or as 2-D islands on graphene surfaces.

Specific details in support of these mechanistic steps are provided in Figure 3-6. In panels a-d, we present the most stable adsorption configurations of citrate and PSA anion on small (Au_{20}) clusters and on extended Au(111) surfaces. In both cases, there were appreciable interaction energies but PSA demonstrated increased stability relative to citrate that could be correlated to the bonding type observed for these two systems. In the case of the citrate ion, adsorption took place exclusively through formation of CO-Au bonds (Figure 3-6a and c); for PSA, both the SO-Au bonds and the long-range dispersion interactions between the aromatic carbon rings and the Au surface (Figure 3-6b and d) contributed to the increased stability. These dispersion interactions between AuNPs and aromatic carbon structures have been recognized in other recent studies,[183-184] and were also believed to provide partially support for the strong binding between AuNPs and peptides with aromatic residues.[185-186] Similar dispersion interactions were found to be responsible for the adsorption of Au_{20} nanoparticles on pristine SWNT (Figure 3-6e) or on graphene (Figure 3-6g) surfaces. In the case of PSA functionalized

graphitic surfaces, Au_{20} clusters could adsorb either on top of the PSA molecule (Figure 3-6f and h) or directly on the graphitic surface with simultaneous binding to PSA (Figure 3-6i and j). The increased stability observed for these latest configurations was a consequence of the fact that Au_{20} cluster interacts simultaneously with SWNT (graphene) surfaces through dispersion interactions as well as through formation of SO-Au bonds to PSA molecules. In the case of larger AuNPs, it was expected that PSA molecules would decorate the nanoparticles, particularly in the interface region with graphitic surface. These results provided valid support for the first adsorption step in our proposed mechanism, where PSA on the surface of SWNTs replaced the citrate to bind AuNPs when SWNT-PSA/CCG-PSA were used as templates.

Additionally, other adsorption configurations were simulated to rationalize the synthetic results obtained when using different graphitic templates. For the SWNT-PCA system, comparable interaction energies were found for the adsorption of PCA anion on Au_{20} and Au(111) surfaces (Figure 3-7 a, e and b, f), which did not match the different results observed in the synthesis. However, the dissociation of pyrene acid in the aqueous system was a factor that should be considered in this case. Unlike the strong acid PSA (with a pKa of about 0.7),[187] PCA is a weak acid with a pKa value of 4.0 that mostly remained in a neutral state.[188] The non-dissociated PCA molecule indeed demonstrated weaker binding to Au compared to the PSA anion (Figure 3-7i and j). These results explained the limited assembly of AuNPs observed on the graphitic surfaces with carboxylic functionalities. With no strong binding site, the adsorbed AuNPs were less likely to meet with each other before diffusing back to the solution phase, and thus no welding happened during this process.

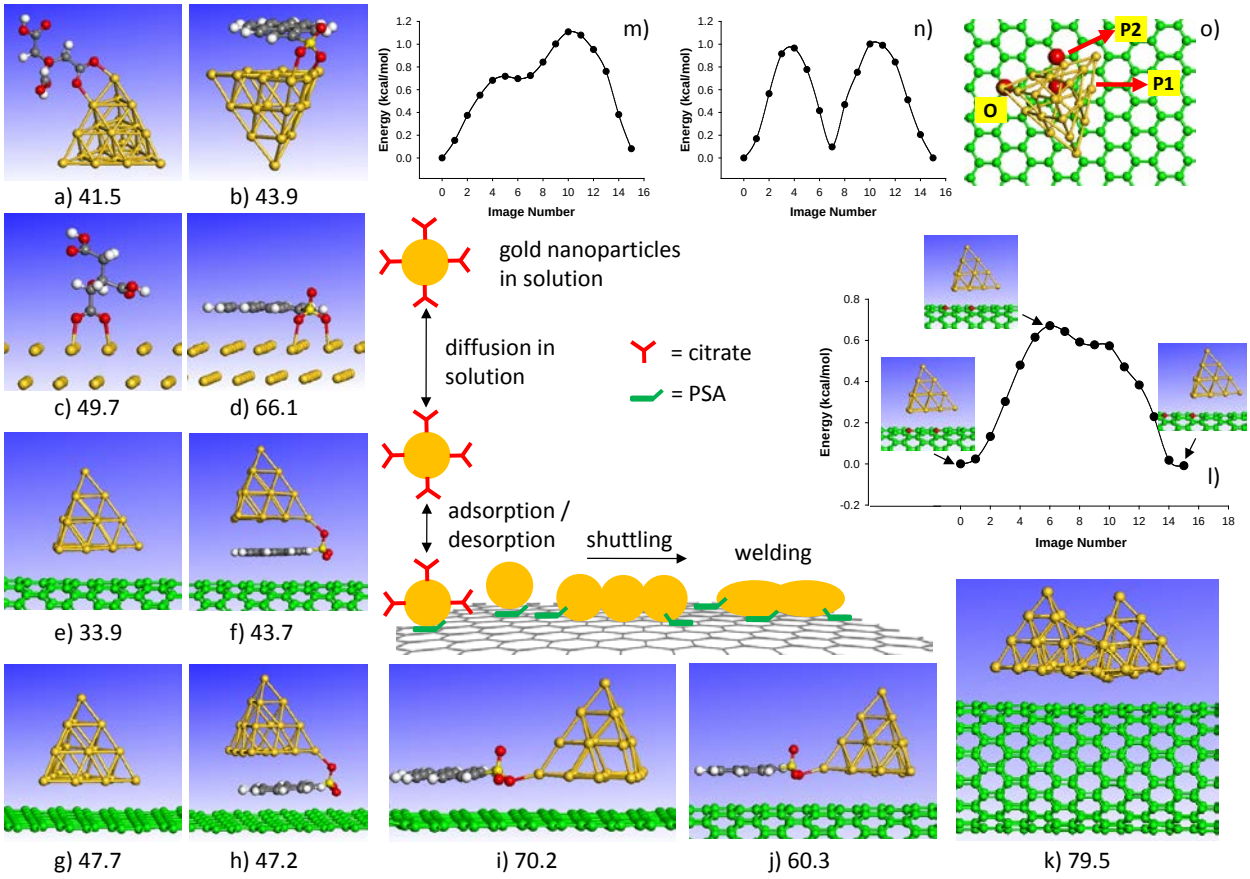

Figure 3-6. Molecular modeling of the adsorption, assembly and nanowelding processes. The middle panel is a schematic illustration of the three mechanistic steps involved in the formation of AuNWs from Au clusters on graphitic surfaces decorated with PSA. (a-d) Adsorption configurations of citrate and PSA on a Au_{20} cluster (a, b) and on Au(111) surface (c, d), respectively. (e-j) Adsorption configurations of a Au_{20} cluster on a bare and PSA decorated CNT (e, f, j) and on bare and PSA decorated graphene (g, h, i); (k) Welding of two Au_{20} clusters on CNT surface. (l) The minimum energy pathway for diffusion of a Au_{20} cluster on a CNT surface between two sites marked in red. (m, n) The minimum energy diffusion pathways of a Au_{20} cluster on graphene surface (from initial position O towards two different directions P1 and P2) indicated in (o). The atomistic configurations correspond to the most stable states identified based on dispersion-corrected DFT calculations. In each case the corresponding binding energies (in kcal/mol) are given with respect to the isolated adsorbate and surface subsystems. In panels a-d the adsorption energies of citrate and PSA are indicated while in panels e-k the adsorption energies of Au_{20} cluster are shown. For PSA and citrate C atoms are represented in gray, O atoms in red, H atom in white and sulfur atom in yellow; for graphene and CNT surfaces C atoms are shown in green while Au atoms are represented in orange.

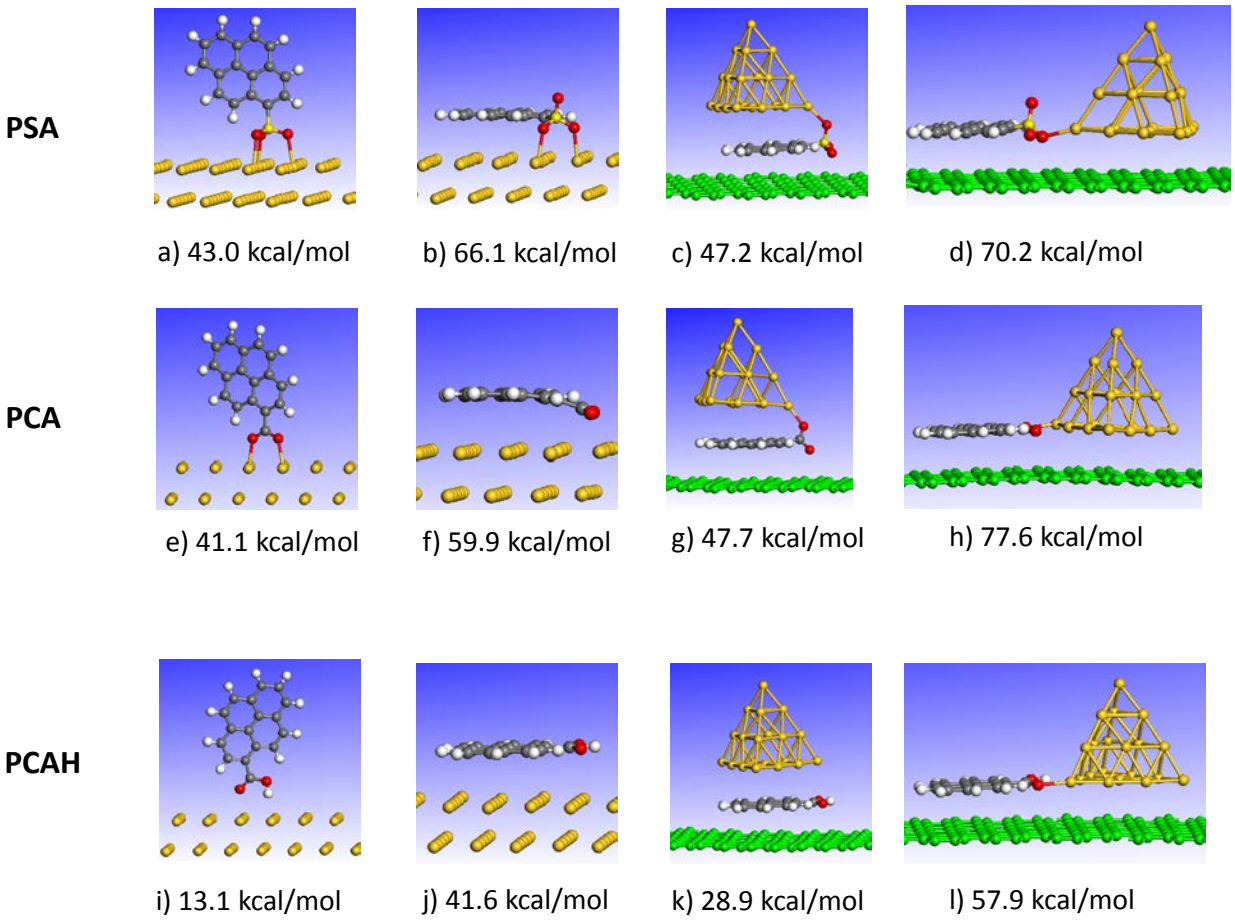

Figure 3-7. Comparison between PSA and PCA functional molecules. Vertical and laying down adsorption configurations of PSA anion (a,b), PCA anion (e,f) and PCA molecule (PCAH, (i,j)) on Au(111) surface. Different adsorption configurations of Au_{20} cluster on PSA (c,d), PCA (g,h) and PCAH (k,l) functionalized graphene. The corresponding binding energies of PSA (a,b), PCA (e, f), PCAH (i,j) and of the Au_{20} cluster (c,d,g,h,k,l) are indicated at the bottom of the corresponding panels.

The adsorbed AuNPs could diffuse on the graphitic surfaces of either SWNT or graphene (second step). We hypothesize a “shuttling mechanism” for this process considering the different results from SWNT-PSA/CCG-PSA and S-SWNTs/S-CCG. After AuNPs bind to the sulfonic groups, the diffusion of PSA molecules on the SWNTs/CCG could carry the AuNPs to assemble together. Due to the weak binding, however, this assembly process did not occur when carboxylic groups were the major surface functionalities. In the case of S-SWNTs and S-CCG, due to the covalent bonding on the surfaces, no “shuttling” of AuNPs would happen. Instead, the AuNPs tightly bound to the sulfonic groups probably acted as a welding center for other AuNPs. The intermediate level of AuNWs formation was a consequence of the competition between the diffusion of AuNPs on the template surface to meet bounded AuNPs and diffusion of AuNPs back to solution.

This diffusion step is illustrated in Figure 3-6l to n in which we present the minimum energy diffusion profiles of a Au_{20} cluster on a SWNT in an axial direction (Figure 3-6l) or on a graphene surface (Figure 3-6m and n) along the P1 and P2 directions shown in the Figure 3-6o. In both cases, the barriers for diffusion were small with values of about 1 kcal/mol. This result indicated that the role of “shuttling” molecules in the self-assembly of AuNPs was not to overcome the energy barriers of in-plane diffusion which are negligible at room temperature conditions. Instead, the “shuttling” molecules provide stronger binding sites for AuNPs than those on pristine SWNTs (Figure 3-6e) or graphene (Figure 3-6g). Such an increased stability is necessary in order to keep the adsorbed AuNPs diffusing (SWNT-PSA/CCG-PSA) or staying attached (S-SWNTs/S-CCG) to the graphitic surface long enough to encounter other AuNPs instead of returning to the solution phase. A similar simulation also revealed that the in-plane diffusion of PSA had a small energy barrier (not shown here). It should also be noted that no

obvious energy difference was found for diffusion barriers of AuNPs along different directions on the 2-D graphene (Figure 3-6m, n, and o). Therefore, the diffusion of AuNPs on the graphitic templates was only confined by the dimensionality of the templates and the resulting Au nanostructures after welding had the same dimensions as the templates (i.e. AuNWs formed on SWNT-PSA or MWNT-PSA and Au plates formed on CCG-PSA). Another fact that should be pointed out was that AuNPs appeared to have a stronger interaction with graphene than SWNTs (Figure 3-6e and g); this could also explain why the aggregation level of AuNPs was higher on graphene templates than on SWNT templates (i.e. CCG-PCA vs. SWNT-PCA, as shown in Figure 3-5b and f).

In the third step of the assembly and welding processes, AuNPs located in close proximity will fuse together. Such a process is illustrated in Figure 3-6k where two Au_{20} clusters initially separated by 3.5 Å nanoweld simply due to the attractive nature of Au-Au interactions. Similar effects are observed for the welding of Au_{20} nanoparticles on a graphene surface starting from different initial configurations. This welding process, achieved through coalescence of adjacent AuNPs, did not require high activation energy and could occur at temperatures much lower than the melting point. This is consistent with the examples of cold welding of Au nanomaterials without thermal heating that have been demonstrated in the literature.[174, 189] Therefore, the thermal heating required in this approach was probably not for the activation of the welding process but rather for overcoming the electrostatic stabilization between individual AuNPs synthesized by citrate reduction.

It should also be noted that the three steps indicated above happen simultaneously in the aqueous system; in the first two steps involving adsorption and nanoparticle diffusion the

individuality of AuNPs is maintained while in the third step upon welding irreversible formation of AuNWs takes place.

3.4.4 Electrical Properties and Chemical Sensing (H_2S) of AuNW-SWNTs

When AuNW-SWNTs hybrid network is incorporated into an electrical circuit, both AuNWs and SWNTs conduct the electricity, and therefore, the Schottky barriers at AuNW-semiconducting SWNT junctions will contribute to the overall conductivity of the network. One practical advantage of such combination is that these Schottky barriers are exquisitely sensitive to changes in the local chemical environment,[121, 190] with direct applications in chemical sensing.

The AuNW-SWNT sensor devices were fabricated by drop-casting the AuNW-SWNT suspension onto a Si chip with interdigitated gold electrodes; the size, pattern and SEM images of a typical device are shown in Figure 3-8a to c. The H_2S response of AuNW-SWNTs was tested, and the data (Figure 3-8d and e) indicated that conductance of the AuNW-SWNT devices significantly decreased when exposed to H_2S at the concentration range from 10 ppb to 40 ppm (diluted in N_2). The detection of H_2S to 10 ppb in N_2 environment at room temperature meets the sensitivity requirement for a variety of applications ranging from mine safety to the detection of breath odor. The recommended exposure limit (REL) to H_2S is 10 ppm, and the presence of H_2S at 500 ppb (or higher) in human breath will cause halitosis (breath odor).[191-192] The cross-sensitivity of AuNW-SWNTs to other major components of natural gas (CH_4) and human breath (O_2, CO_2, H_2O, and artificial flavor compounds) was also tested, and no obvious cross-sensitivity was observed (Figure 3-8f and g). Although the H_2S response appeared to be irreversible at room temperature due to the well-known affinity of Au to S, the recovery of the baseline was achieved simply by heating the sensor chip at 140 °C for 30 min in ambient environment, and the sensor

was found to be reusable. Such heating induced recovery was also observed for other reported Au based H_2S sensors.[178-179]

As a comparison, AuNP-SWNT devices fabricated by electrochemical deposition were also tested for their response to H_2S at both the ppb and ppm levels (Figure 3-8e). At the tested H_2S concentration ranges, AuNW-SWNTs appeared to have better sensitivity to H_2S, especially in the ppb level, with a detection limit for H_2S of about one order of magnitude lower than that of AuNP-SWNTs (the detection limit of AuNW-SWNTs was calculated to be 5 ppb, while the detection limit of AuNP-SWNTs was determined to be around 50 ppb, as demonstrated in Figure 3-9). H_2S tests were also conducted on pristine SWNTs, and much smaller response was observed (Figure 3-8e).

The advanced H_2S sensitivity and selectivity of AuNW-SWNTs originates from the strong Au-S interaction which, however, raises the problem of the reversibility. As shown in Figure 3-8d, the sensor response of AuNW-SWNTs to the H_2S analyte is indeed irreversible at room temperature. In order to overcome this limitation and enable the multiple detections and long-term operations for the AuNW-SWNTs sensors, we demonstrate two modified methods of sensor operation. The first approach is to constantly heat the sensor with an incorporated microheater device. As shown in Figure 3-10a, the H_2S response of the AuNW-SWNTs sensor became reversible when operated at elevated temperature (80 °C). This temperature is relatively mild compared with other high temperature semiconductor sensors, and does not require significant amount of energy consumption. The second approach keeps the room-temperature operation of the device, and employs a post heating to recover the sensor baseline after each H_2S exposure, as demonstrated in Figure 3-10b. The advantage of this latter approach is that it can

keep the benefits from room-temperature operation (low-cost, low-power, easy fabrication, etc.) and only requires a relatively convenient and low-cost step to “refresh” the sensor devices.

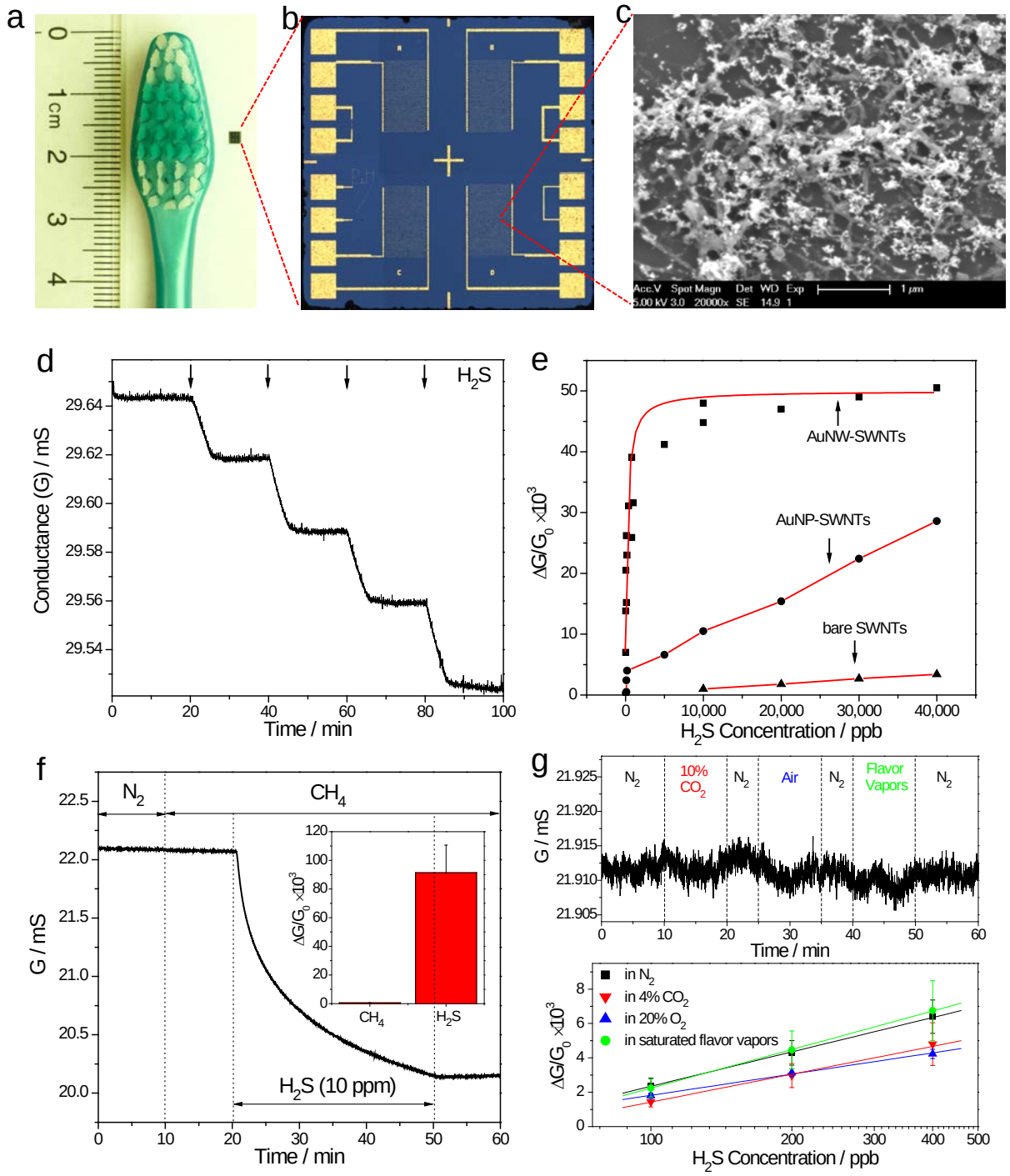

Figure 3-8. Hydrogen sulfide (H_2S) sensitivity of AuNW-SWNT devices. (a) A photograph of the chemiresistor chip in comparison to a toothbrush. (b) An optical image of the chip with micropatterned four interdigitated gold electrodes. (c) SEM image of the AuNW-SWNTs hybrids network bridging two fingers of interdigitated electrodes. (d) A typical real-time network conductance measurement in pure nitrogen and upon four H_2S exposures (5 min)

with concentrations of 100 ppb, 200 ppb, 400 ppb and 1ppm, arrows correspond to the points when H_2S gas was introduced. (e) Electrical response of AuNW-SWNT, AuNP-SWNT and bare SWNT networks to various concentrations of H_2S gas (5 min). The relative conductance change ($\Delta G/G_0$) of AuNW-SWNTs fits the Langmuir isotherm (red curve). (f) Cross-sensitivity of AuNW-SWNTs to typical natural gas components (methane), inset depicts the comparison of the sensor response to 100% methane and 10 ppm H_2S in methane. (g) Cross-sensitivity of AuNW-SWNTs to typical human breath components (carbon dioxide, oxygen and flavor vapors), top depicts the response of AuNW-SWNTs to 10% carbon dioxide, 20% oxygen (air) and saturated vapors of commercial flavor mixture from Colgate-Palmolive company, bottom depicts the sensor response to H_2S (5 min) with concentrations of 100 ppb, 200 ppb, 400 ppb in nitrogen, 4% carbon dioxide, 20% oxygen and saturated vapors of flavor mixture.

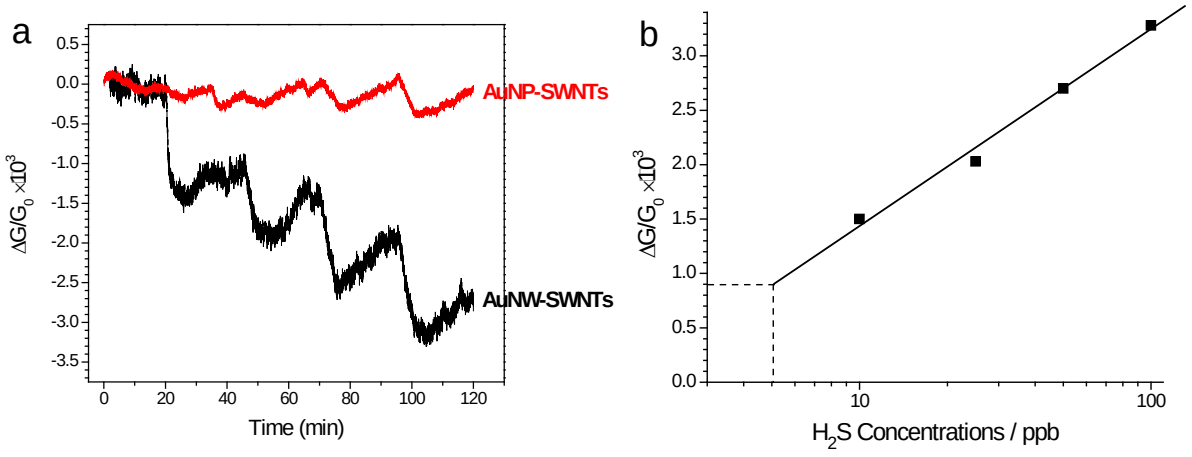

Figure 3-9. Calculation of the detection limit. (a) Real-time network conductance measurement of AuNW-SWNTs and AuNP-SWNTs devices in pure nitrogen and upon four H_2S exposures (5 min) with concentrations of 10 ppb, 25 ppb, 50 ppb and 100 ppb. (b) Determination of the detection limit of AuNW-SWNTs (detection limit was calculated to be 5 ppb).

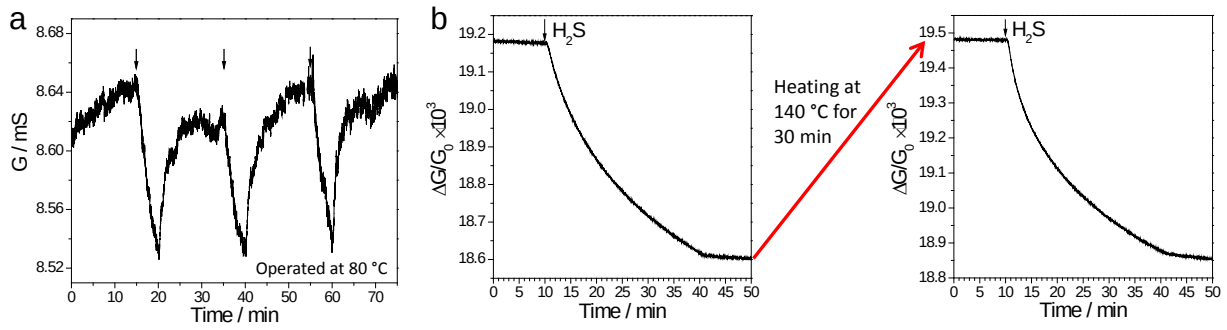

Figure 3-10. Reversible detection of the AuNW-SWNTs H_2S sensor. (a) Reversible response of AuNW-SWNTs upon three exposures of H_2S (1 ppm) when operated at 80 ℃. (b) Recovery of the AuNW-SWNTs sensor device by post heating. The left panel indicates the response of a AuNW-SWNTs sensor exposed to 10 ppm H_2S for 30 min. The right panel indicates the response of the same device tested in the next day after heating at 140 °C for 30 min on a hot plate in ambient environment.

3.4.5 Gas Sensing Mechanisms: AuNW-SWNTs vs. AuNP-SWNTs

One interesting observation is that AuNW and AuNP functionalized SWNTs have different sensing dynamics even though their recognition of H_2S molecules are both based on Au-S interaction. The enhanced chemical sensitivity of AuNW-SWNTs clearly indicates the importance of the gold nanostructures in the hybrid system, which requires further investigation. The architecture of the sensing network was firstly examined to rationalize the differences between AuNW and AuNP decorated SWNT networks. As can be observed from the SEM images of each device (Figure 3-11), 1-D AuNWs formed several connections between SWNTs, which could create additional electrical pathways through the SWNT network. Since the AuNWs became part of the conducting network, it can be hypothesized that the adsorption of H_2S molecules could probably create scattering centers on the AuNWs and modulate the Schottky

barriers at the AuNW-SWNT interfaces, which more effectively decreased the conductivity of the sensing network. AuNPs on the other hand remained isolated (discontinuous and not bridging the SWNTs) in the hybrid system, and their H_2S sensitivity probably involved the H_2S induced charge transfer from AuNPs to the SWNT network, as recently reported elsewhere.[179, 193]

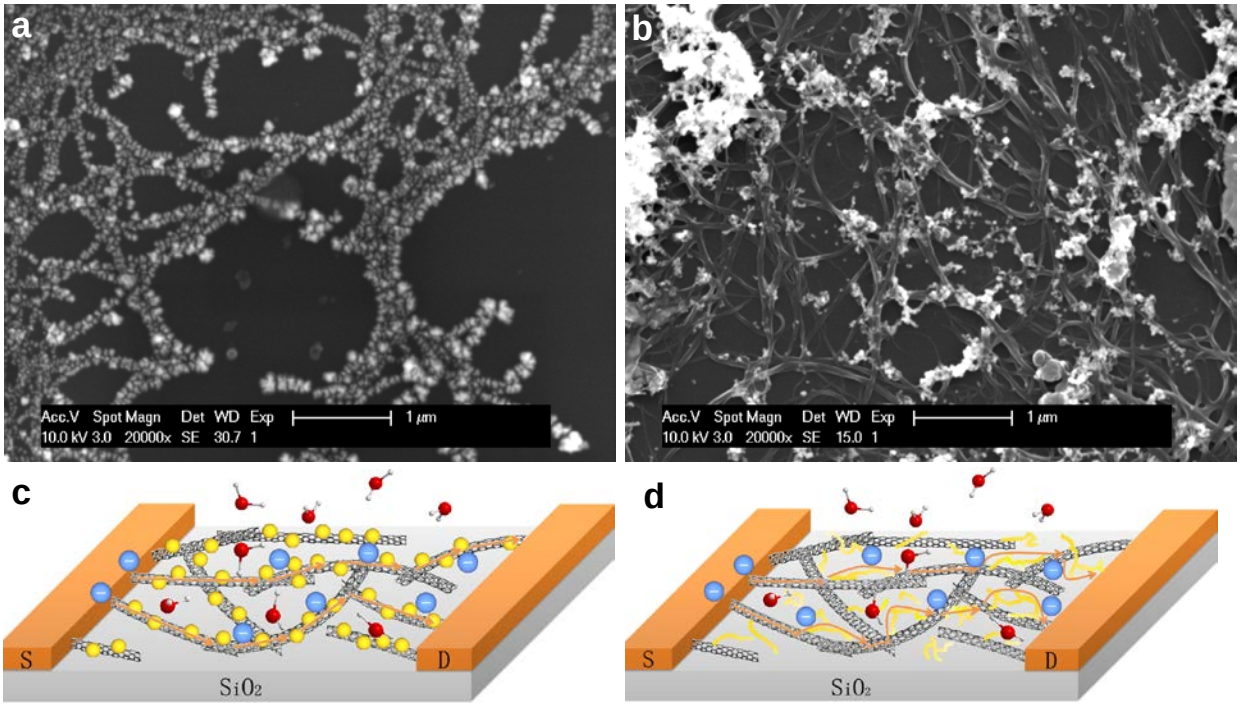

Figure 3-11. Comparison of the sensing platforms. SEM images of (a) AuNP-SWNTs device and (b) AuNW-SWNTs device. AuNPs remain isolated on the SWNT network, AuNWs disperse among the network and bridge the SWNTs. (c, d) Schematic illustration of two different pathways for the charge carriers: (c) for AuNW-SWNTs, current flows through SWNTs network; (d) for AuNW-SWNTs, 1-D AuNWs create a pathway for current flow, arrows indicate the path by which electricity flows.

To further investigate the sensing mechanism of H_2S detection and to test this hypothesis, spectroscopic (UV-vis-NIR) studies of AuNW-SWNTs and AuNP-SWNTs thin films upon H_2S exposure were carried out. In addition to the S_{11}, S_{22}, and M_{11} transition band from the SWNTs, Au nanostructures exhibit a surface plasmon resonance (SPR) band in the visible range of the spectra, which provides additional spectroscopic probing. Our previous results[47] have demonstrated that charge transfer interactions between gas molecules (e.g., NH_3, NO_2) and SWNTs will cause a measurable intensity change of S_{11} peak, thus we can use the same analysis to explore the interaction between H_2S molecules and Au-SWNTs hybrid nanomaterials.

As shown in Figure 3-12a, no change in Au SPR peak or S_{11} peak of AuNW-SWNTs was observed upon exposure to 100 ppm H_2S, even though AuNW-SWNTs showed excellent sensitivity to ppm and ppb level concentrations of H_2S. As a comparison, we also prepared AuNP-SWNTs film by electrodeposition of Au nanoparticles onto the SWNTs film. It turned out that electrodeposited AuNP-SWNTs showed an obvious increase in the S_{11} intensity upon H_2S exposure, whereas the Au SPR peak remained unchanged (Figure 3-12b).

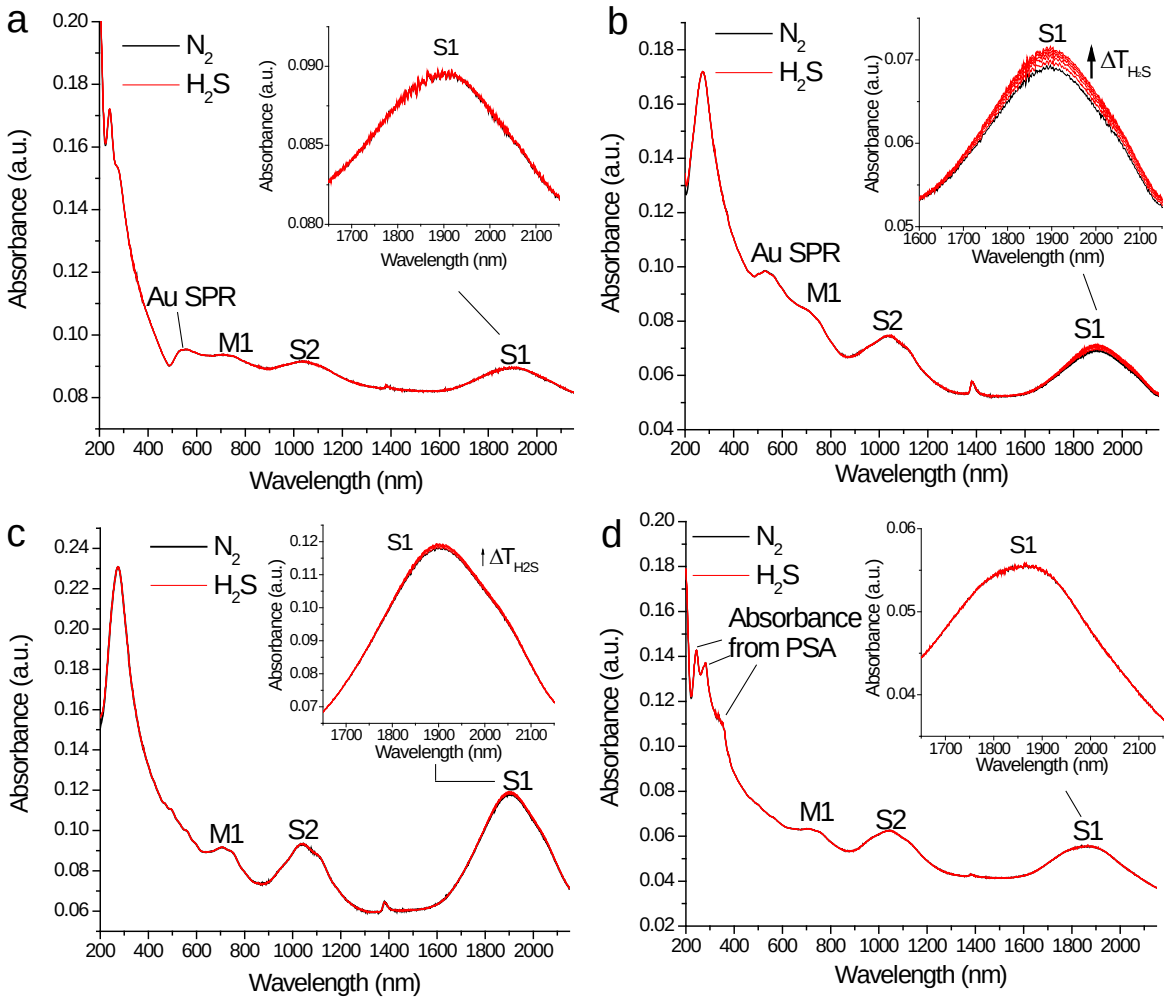

Figure 3-12. Spectroscopic characterization of the sensing mechanisms. UV-vis-NIR absorption spectra of (a) AuNW-SWNTs (b) AuNP-SWNTs (c) Bare-SWNTs and (d) SWNTs-PSA upon exposure to 100 ppm H_2S in N_2.

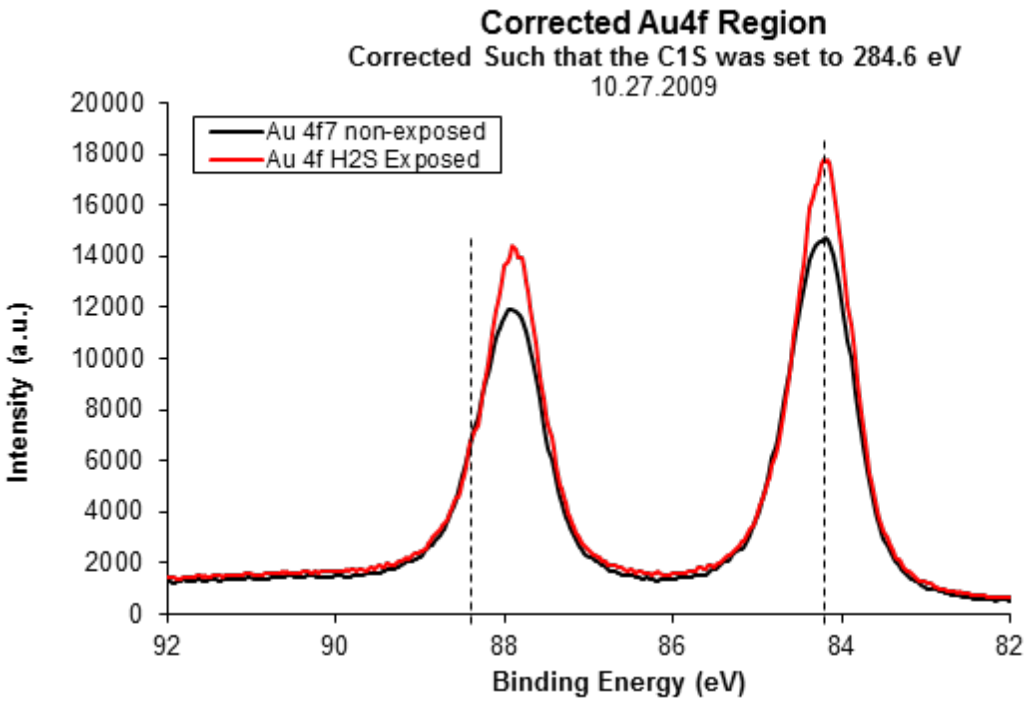

Figure 3-13. XPS of Au 4f (in AuNW-SWNTs) before and after H_2S exposure.

The reason why interaction between H_2S and gold resulted in no obvious change in Au SPR peak (in both Au-SWNTs films) can be explained by the coordination nature of the Au-S bond[194-195] which may not significantly affect the resonance of conducting band electrons of Au surface atoms.[194] This was also confirmed by our XPS results (Figure 3-13). More interestingly, the difference in the S_{11} peak behavior between AuNW-SWNTs film and electro-deposited AuNP-SWNTs film upon H_2S exposure suggests distinct sensing mechanisms. To get a further understanding of this phenomenon, we performed similar measurement on bare SWNTs and SWNTs functionalized with 1-pyrenesulfonic acid (PSA, which was used for non-covalent functionalization of SWNTs) as two control experiments. As we can see in Figure 3-12c and d, bare SWNTs without any further functionalization showed a small increase (less than 1%) in the

S_{11} band, which indicates electron donation to SWNTs by H_2S molecules;[194] in contrast, SWNTs functionalized with PSA showed no such increase in S_1 peak, indicting the PSA was inhibiting the charge transfer between H_2S and SWNTs.

Considering all of these UV-vis-NIR results as well as electrical H_2S sensing experiments, some conclusions regarding the H_2S sensing mechanism can be drawn here: Firstly, without any functionalization, there will be a slight charge transfer interaction between bare SWNTs and H_2S molecules (H_2S donating electrons to SWNTs), such electron donation effect, however, is so small that it will not cause significant conductivity change in the SWNTs network. Alternatively, H_2S binding on Au electrodes will affect the Schottky barriers between the electrodes and SWNTs, such an effect is small, but will cause a minor conductivity change of the whole device (which is observed to be ~0.1% for 10 ppm H_2S exposure, neglectable compared to H_2S response of AuNP-SWNTs or AuNW-SWNTs). Secondly, with PSA functionalization, which was used in this project, such charge transfer between H_2S and SWNTs will be inhibited. Thirdly, with Au nanoparticles directly electrodeposited onto the SWNTs surface, the charge transfer effects are greatly enhanced as indicated by significantly larger increase in S_{11} peak. As a result, p-type SWNTs have electrons donated to the valence band and causing a charge-carrier (h^+) recombination, thus the conductivity of the whole AuNP-SWNTs network will decrease, providing the H_2S sensitivity. And lastly, for the AuNW-SWNTs sensor, with PSA linker to the SWNTs, such charge transfer is inhibited, thus the conductance change we observe in the H_2S sensing test most likely originate from the interaction between H_2S and Au surface and the consequent conductivity change of AuNWs or AuNW-SWNT junctions (Schottky Barriers) in the whole AuNW-SWNTs network.

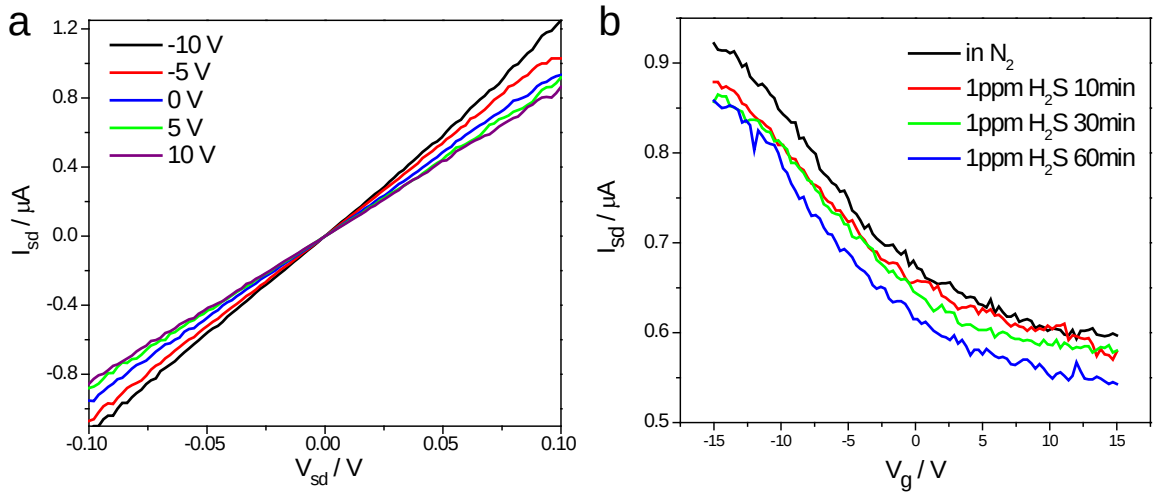

Figure 3-14. Electrical investigation of the sensing mechanisms. (a) I-V characteristics of AuNW-SWNTs at -10 to 10 V gate voltages. (b) Source-drain current (I_{sd}) versus back gate voltage (V_g) of AuNW-SWNTs network in N_2 or with different time (10 min, 30 min, 60 min) of H_2S exposure (1ppm in N_2).

The field-effect-transistor (FET) measurement is another effective way to identify the sensing mechanism of CNT-based sensors.[196] Therefore, the FET characteristics of AuNW-SWNTs network was measured and used to further prove the suggested sensing mechanism (Figure 3-14). Figure 3-14b shows a typical source-drain current (I_{sd}) versus back gate voltage (V_g) curve (black line) measured in N_2. While the AuNW-SWNTs remained part of the p-type semiconductor characteristics from the semiconducting SWNTs and Schottky Barriers between SWNTs and AuNWs, the network also had a specific high "off" current because of the metallic SWNTs and more importantly, AuNWs. This result is in accordance with what we proposed in the H_2S sensing mechanism, revealing the role of 1-D AuNWs and Schottky Barriers played in the AuNW-SWNTs network. The I_{sd}-V_g curves simultaneously recorded during different times of H_2S exposure are also shown in Figure 3-14b (red, green and blue curves). Exposure to H_2S

caused a two stage change in the I_{sd}-V_g curve of AuNW-SWNTs device. First the curve showed a slightly tilt while the "off" current remained unchanged (red curve), this tilt indicated the modification of Schottky Barriers between AuNWs and semiconducting SWNTs.[196] With longer exposure time (green curve), the transistor characteristics started to shift towards the negative current ("shifting down"). Such negative shift in baseline current suggested a decrease in the conductivity of metallic part of the network, which is most like to be the AuNWs. When the H_2S molecules were adsorbed onto the surface of AuNWs, they created new scattering centers and thus caused carrier mobility reduction in AuNWs. With longer exposure time, the I_{sd}-V_g curve of AuNW-SWNTs finally showed changes with combined effects (blue curve). Overall, the FET characterizations further support the hypothesis on the sensing mechanisms of AuNW-SWNTs hybrid network.

3.5 CONCLUSION

In summary, we have explored the self-assembly and nanowelding processes of AuNPs on graphitic templates and demonstrated a simple yet scalable bottom-up approach for the synthesis of 1-D AuNWs using 0-D AuNPs as building blocks. SWNTs-PSA appeared to be an effective template material for 1-D assembly of AuNPs, and subsequent nanowelding of aligned AuNPs could be induced by thermal heating to form AuNWs. DFT simulations elucidated the mechanism of this process. The three-step model revealed in this work, which included adsorption, in-plane diffusion ("shuttling") and nanowelding, provided some insights into controlling and manipulating the motion of nanoparticles on the graphitic surface, and this work supplemented the existing toolbox of bottom-up fabrication techniques for complex material

architectures. Additionally, the AuNW-SWNT network showed ultrasensitivity to H_2S in both the ppb and ppm levels with detection limit as low as 5 ppb at room temperature. This hybrid material exhibited a promising potential for incorporation into a portable, low-power, inexpensive and easy-to-use detection tool for applications such as industrial control, personal safety or personal healthcare. The sensing mechanisms of both AuNW-SWNTs and AuNP-SWNTs hybrid systems have systematically investigated through spectroscopic and electrical characterizations. It was demonstrated that different morphology of the Au functionalities significantly altered the sensing mechanisms of the resulting hybrid nanostructures, indicating the importance to understand and control the hybrid morphology and interfacial conditions for the future improvement of such sensing technology.

4.0 PHOTOINDUCED CHARGE TRANSFER AND CHEMICAL SENSITIVITY OF SINGLE-WALLED CARBON NANOTUBE-TITANIUM DIOXIDE HYBRID NANOMATERIALS

4.1 CHAPTER PREFACE

Part of the materials contained in this chapter was published as a research article in *the Journal of American Chemical Society*; figures used in this chapter have been reprinted with permission from *J. Am. Chem. Soc.* **2013**, DOI: 10.1021/ja402887v. (listed as reference 98 in bibliography section).

List of Authors: Mengning Ding, Dan C. Sorescu, and Alexander Star.

Author Contributions: DMN and AS designed the experiments and wrote the manuscript, DMN performed the experimental work and DCS performed computational modeling.

4.2 INTRODUCTION

Considerable research efforts have been recently devoted to develop novel hybrid nanostructures with increased complexity and expanded functionality that could benefit nanotechnology-based electronics,[1] medicine,[2-4] catalysis,[5-6] energy generation[7-8] and sensors.[4, 11-14] For example, titanium dioxide (TiO_2) has been combined with carbon nanotubes (CNTs) to improve the TiO_2 performance in photovoltaics[7] and photocatalysis.[197] Incorporation of CNTs brings certain potential advantages. Firstly, the high conductivity of CNTs could provide effective electron pathways, therefore increase the electron diffusion length and prevent the electron-hole recombination.[7, 197-199] Secondly, the one-dimensional (1-D) morphology of CNTs could serve as a template[24, 200-201] to regulate the growth of TiO_2 into 1-D structures, while 1-D morphology[202-207] and core/shell architecture[208-209] could both lead to enhanced electronic transport and result in improved efficiency of photocatalysis or photovoltaic devices. The third advantage relates specifically to the single-walled carbon nanotubes (SWNTs). Due to their unique optical and electrical properties that are sensitive to the electron donation or acceptance, SWNTs could be employed as spectroscopic[30, 210-214] or electrical[12, 30, 215-216] probes in a hybrid system to elucidate the underlying charge transfer and electronic interaction at the interface. Moreover, the ease of fabrication and the high performance of SWNT-based semiconductor devices allow the utilization of SWNT-based hybrid materials in real-world applications such as chemical sensing.[12, 14, 214] In this work, we demonstrate the unique electrical behavior of SWNT-TiO_2 hybrid systems upon photoexitation and chemical exposure, through which their interfacial electronic coupling, charge separations and photocatalytic activities can be successfully probed.

In addition, we report a SWNT-TiO_2 nanohybrid with core/shell structure for the room-temperature detection of acetone vapors at ppm concentrations, which offers promising clinical applications (*e.g.*, diagnostic tools) as concentration of breath acetone has long been correlated with ketoacidosis and the blood sugar level in case of diabetes.[217-218] Density functional theory (DFT) calculations have also been applied here to further study the electronic coupling of TiO_2 and SWNTs and to rationalize the underlying mechanism of acetone sensitivity.

4.3 EXPERIMENTAL SECTION

Materials: Pristine single-walled carbon nanotubes (P2-SWNTs) and oxidized single-walled carbon nanotubes (P3-SWNTs, containing surface functionalities of carboxylic acids between 1.0 and 3.0 atomic %) were obtained from Carbon Solutions Inc. Titanium(IV) isopropoxide ($Ti(iOPr)_4$, 99.999% trace), titanium(IV) oxide (anatase, nanopowders, 99.7% metal basis), titanium (IV) oxide (rutile, nanopowders, 99.5% metal basis), and all other chemicals and organic solvents were purchased from Sigma Aldrich and used as received. Si chip with an oxide layer (300 nm thick) and interdigitated gold electrodes were purchased from MEMS and Nanotechnology Exchange, and 40 lead ceramic sidebraze (CERDIP) packages (cavity 0.310 × 0.310) were procured from Global Chip Materials, LLC. Cylinders with ultra-high purity gases or gas mixtures (grade 5.0 dry N_2, grade 5.0 dry O_2, 20 ppm acetone balanced in grade 5.0 dry N_2, 20 ppm acetone balanced in grade 5.0 dry air, 10% CO_2 balanced in grade 5.0 dry N_2, 200 ppm ethanol balanced in grade 5.0 dry N_2) were all purchased and certificated from Matheson Tri-Gas DBA Valley.

Synthesis of o-SWNT@TiO_2 core/shell nanohybrids: o-SWNTs (P3, 0.5 mg) were suspended in ethanol (17 mL) by ultrasonication (30 min using a Branson 5510 bath sonicator). $Ti(OiPr)_4$ (50 μl) was added under vigorous stirring using micropipette and the mixture of o-SWNTs and $Ti(OiPr)_4$ was stirred for 1 hr. Deionized (DI) water was subsequently added into the system (300 μL x10 over 50 minutes) and the resulting mixture was stirred for an additional 15 minutes. The final product was isolated on a filter (PTFE filter membrane, 2 μm), washed with ethanol (x3), and resuspended in DI water (20 mL).

Synthesis of SWNT-PSA@TiO_2 core/shell nanohybrids: pristine SWNTs (P2) were first functionalized with PCA in ethanol following a similar approach described in section 2.4 and 3.4. PCA functionalized SWNTs (1.5 mL, 0.25 mg/mL) were then diluted in ethanol (16 mL) by ultrasonication (30 min using a Branson 5510 bath sonicator). $Ti(OiPr)_4$ (50 or 25 μl) was added under vigorous stirring using micropipette and the mixture of o-SWNTs and $Ti(OiPr)_4$ was stirred for 1 hr. Deionized (DI) water was subsequently injected by a syringe pump into the system (30 mL/hr for 30 to 60 min) and the resulting mixture was stirred for an additional 15 minutes. The final product was isolated on a filter (PTFE filter membrane, 2 μm), washed with ethanol (x3), and resuspended in DI water (20 mL).

Synthesis of SWNT&TiO_2 mechanically mixed nanohybrids: SWNTs (P2 or P3, 0.5 mg) and anatase TiO_2 nanopowders (3 or 15 mg) were each sonicated in DI water (10 mL) for 15 min. The SWNT and TiO_2 suspensions were then mixed together and sonicated for another 15 min.

Synthesis of SWNT-TiO_2 covalently linked nanohybrids: P3-SWNTs (0.5 mg) were suspended in ethanol (17 mL) by ultrasonication (30 min). The suspension was then vigorously stirred, and $Ti(OiPr)_4$ (5 μl) was then added into the suspension. The mixture of P3-SWNTs and $Ti(OiPr)_4$ was stirred for 1 hr, and then TiO_2 suspension (anatase nanopowders, 3 or 15 mg

suspended in 3 mL ethanol after 15 min of sonication) was added into the system. The reaction mixture was further stirred for 1 hr, and was then centrifuged to collect the final product. The product was washed with ethanol for three times, and was resuspended in 20 mL of DI water.

Synthesis of GOx-TiO_2 nanohybrids: GOx suspension (5 mg/mL x 1 mL) was diluted with ethanol (16 mL). $Ti(OiPr)_4$ (50 μl) was added under vigorous stirring using micropipette and the mixture of GOx and $Ti(OiPr)_4$ was stirred for 1 hr. Deionized (DI) water was subsequently added into the system (300 μL x10 over 50 minutes) and the resulting mixture was stirred for an additional 15 minutes. The final product was isolated on a filter (PTFE filter membrane, 2 μm), washed with ethanol (x3), and resuspended in DI water (20 mL).

General Characterizations: Transmission electron microscopy (TEM) of all the synthesized samples were performed on a FEI Morgagni microscope, operating at an acceleration voltage of 80 keV. High resolution TEM (HRTEM) images were obtained on a JEOL 2010F high-resolution transmission electron microscope, operating at an accelerating voltage of 200 keV. Scanning electron microscopy (SEM) was performed with a Phillips XL30 FEG microscope equipped with an energy dispersive x-ray spectroscopy (EDS) accessory. X-ray Diffraction (XRD) was performed with a Bruker D8 Discover XRD with GADDS Detector for powder and thin film diffraction. Raman spectroscopy was performed with a Renishaw inVia Micro-Raman Microscope (using an excitation wavelength of 633 nm).

Electrical test and chemical sensing measurement: Electrical tests and sensor measurements were performed to the similar procedures described in section 2.4 and 3.4. A different gas chamber was used where a quartz window was on top for the UV light exposure. Ultraviolet light was generated from a UVP Model UVGL-55 hand-held lamp (365 nm in wavelength, 25 $\mu W \cdot cm^{-2}$). During the sensing tests, different concentrations of analyte gases

were generated by mixing certified gases (20 ppm acetone balanced in dry N_2, and other gases all purchased from Valley National Gas, Inc.) with dry N_2 at controlled ratio of gas flow rate and were passed through the gas chamber containing the sensor device.

4.4 RESULTS AND DISCUSSION

4.4.1 Synthesis of SWNT-TiO_2 hybrids with core/shell morphology

Oxidized SWNTs (o-SWNTs, containing surface oxygen functional groups between 1.0 and 3.0 atomic %)[219] were purchased from Carbon Solutions, Inc. and used as received. The growth of a TiO_2 layer over individual SWNT was achieved through a two-step sol-gel synthesis approach, as illustrated in Figure 4-1a. Carboxyl or hydroxyl groups on the surface of SWNTs first reacted with titanium(IV) isopropoxide ($Ti(OiPr)_4$), which was used as the TiO_2 precursor. The grafted -O-$Ti(OiPr)_3$ underwent further hydrolysis and condensation steps upon addition of water. This sol-gel process initiated from the surface of SWNTs produced a one-dimensional core/shell structure. Transmission electron microscopy (TEM) images (Figure 4-1b) illustrated the morphology of this o-SWNT@TiO_2 core/shell hybrid material. Exposed parts of nanotubes were still observed (Figure 4-1c), indicating an incomplete TiO_2 layer on the SWNT surface determined by the distribution of oxygen functional groups on the nanotube walls. TiO_2 templated along SWNTs in a pseudo one-dimensional morphology, with some level of aggregations probably resulting from the hydrolysis and condensation of excess of $Ti(OiPr)_4$ in the suspension. The majority part of as-synthesized TiO_2 appeared to be amorphous, with small crystalline regions observed in high-resolution TEM (HR-TEM) images (Figure 4-1d). The

interfringe distances of the crystal lattice in theseareas were determined to be 0.350 nm, which correspond to the lattice spacing of anatase (101) surface. Similar to other TiO_2 materials prepared by sol-gel approach, the overall cystallinity of the o-SWNT@TiO_2 nanohybrids could be tuned upon further calcination (Figure 4-1e). Raman spectroscopy, X-ray diffraction (XRD) and energy-dispersive X-ray spectroscopy (EDX) were employed to confirm the composition and crystallinity of the resulting nanostructures (Figure 4-2). We also noticed that the thickness and morphology of the TiO_2 shell were dependent on the amount and rate of water injection during sol-gel synthesis with SWNT templates (Figure 4-3).

A noncovalent approach similar to what have been described previously (Chapter 2 and 3) has also been applied for the synthesis of TiO_2 coatings over the pristine SWNTs functionalized with PSA. As shown in Figure 4-4, SWNT@TiO_2 core/shell nanohybrids were successfully synthesized and a more uniform coating (with narrower distribution of diameters) was achieved with this noncovalent approach. Moreover, the diameters of the TiO_2 shell could be controlled by the amount of Ti precursor and H_2O. Similar synthetic approaches were also applied to the GOx (not shown here). While the other types of SWNT@TiO_2 and GOx-TiO_2 hybrid nanomaterial are still under investigation, the characterization and electrical/sensing properties discussed in the following text is based on o-SWNT@TiO_2 hybrid system.

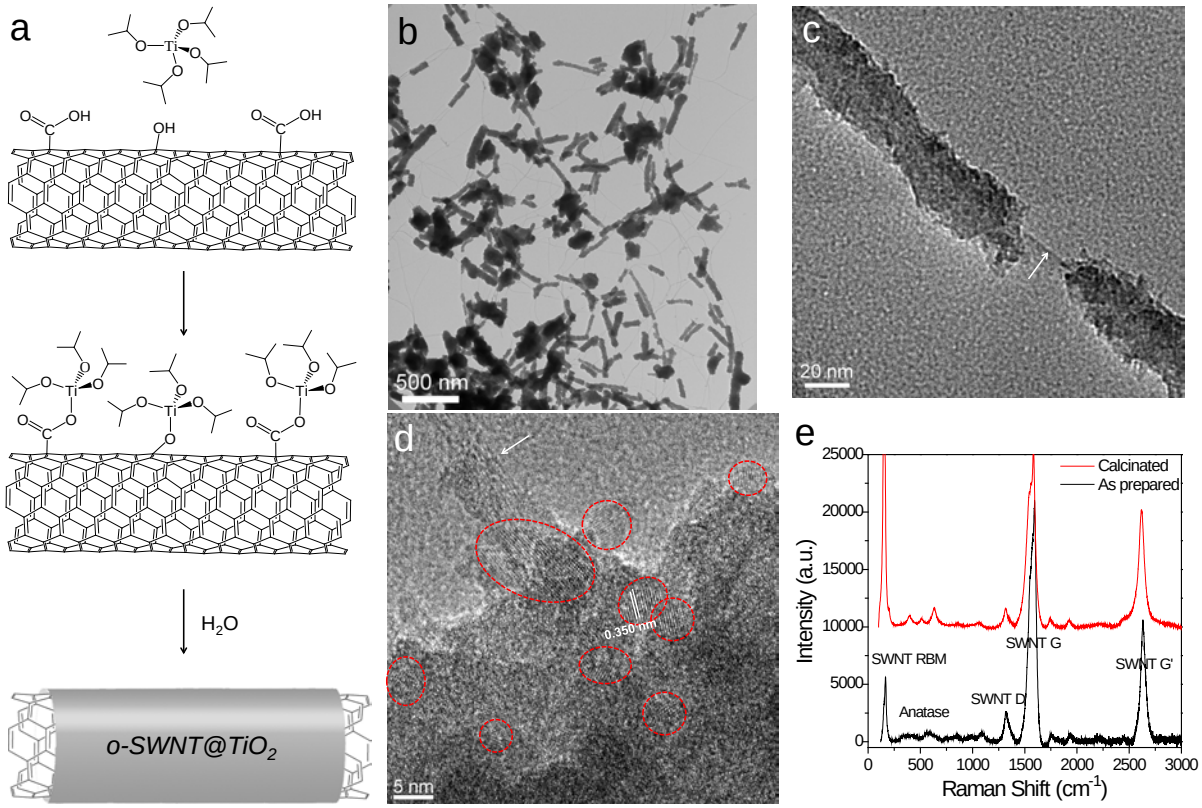

Figure 4-1. Synthesis of single-walled carbon nanotube-titanium dioxide core/shell nanostructures (o-SWNT@TiO_2). (a) Sol-gel synthesis of o-SWNT@TiO_2 hybrid using titanium isopropoxide, $Ti(OiPr)_4$ as a precursor and oxidized SWNTs as a template. The $Ti(OiPr)_4$ precursor first reacted with oxygen surface functionalities of SWNTs, and further hydrolysis upon addition of water resulted in the growth of a TiO_2 shell over SWNTs. (b, c) Transmission electron microscopy (TEM) images revealing the formation of pseudo one-dimensional TiO_2 shells over SWNTs. (d) High-resolution TEM image of the SWNT-TiO_2 boundary, with small crystalline regions highlighted by red ovals. White arrows in c and d indicate the uncoated SWNT segments. (e) Raman spectroscopy of the o-SWNT@TiO_2 hybrids before and after calcination.

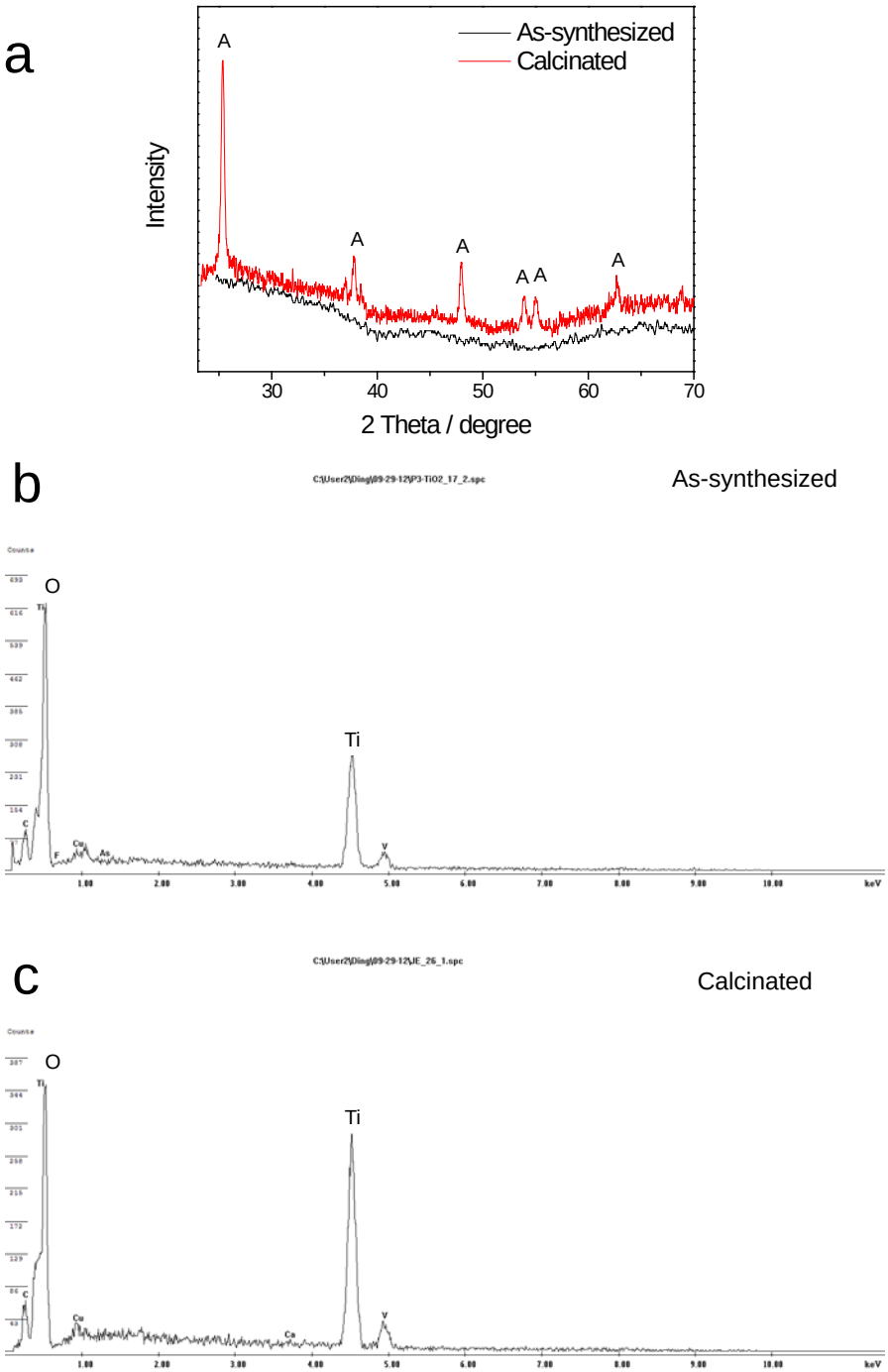

Figure 4-2. Additional characterization of the crystallinity and composition of the hybrid nanostructures. (a) X-ray diffraction (XRD) and (b, c) energy dispersive x-ray spectroscopy (EDX) of as-prepared (b) and calcinated (500 °C for 30 min in Ar) (c) SWNT/TiO_2 core/shell nanohybrids.

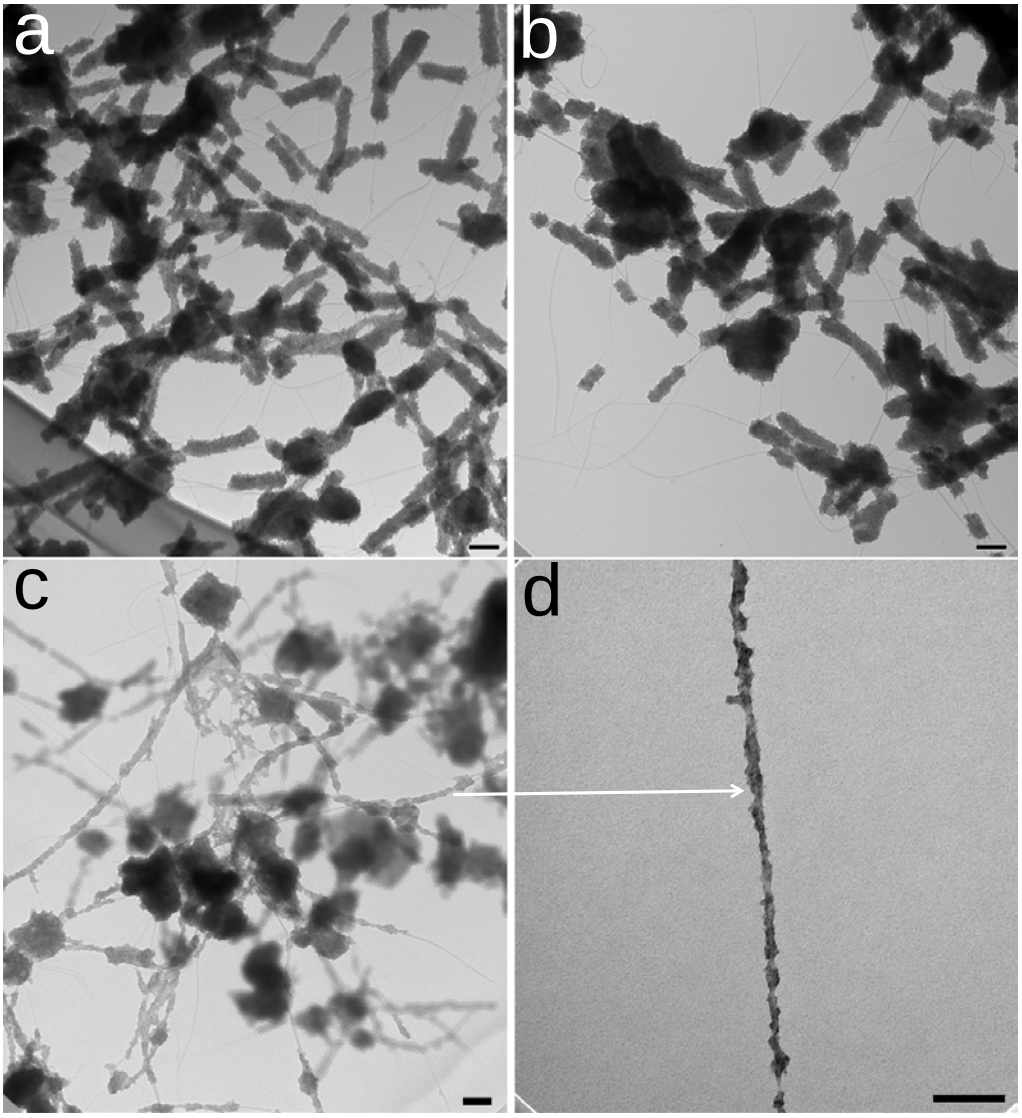

Figure 4-3. Morphology control of the o-SWNT@TiO_2 nanohybrids. TEM images of o-SWNT@TiO_2 core/shell hybrids prepared using: (a) $Ti(OiPr)_4$: H_2O ratio of 1:1000 (the hybrid was used in electrical studies, (b) $Ti(OiPr)_4$: H_2O ratio of 1:500 and (c) and (d) without any addition of water but stirring of reaction mixture in ambient for 72 hr.

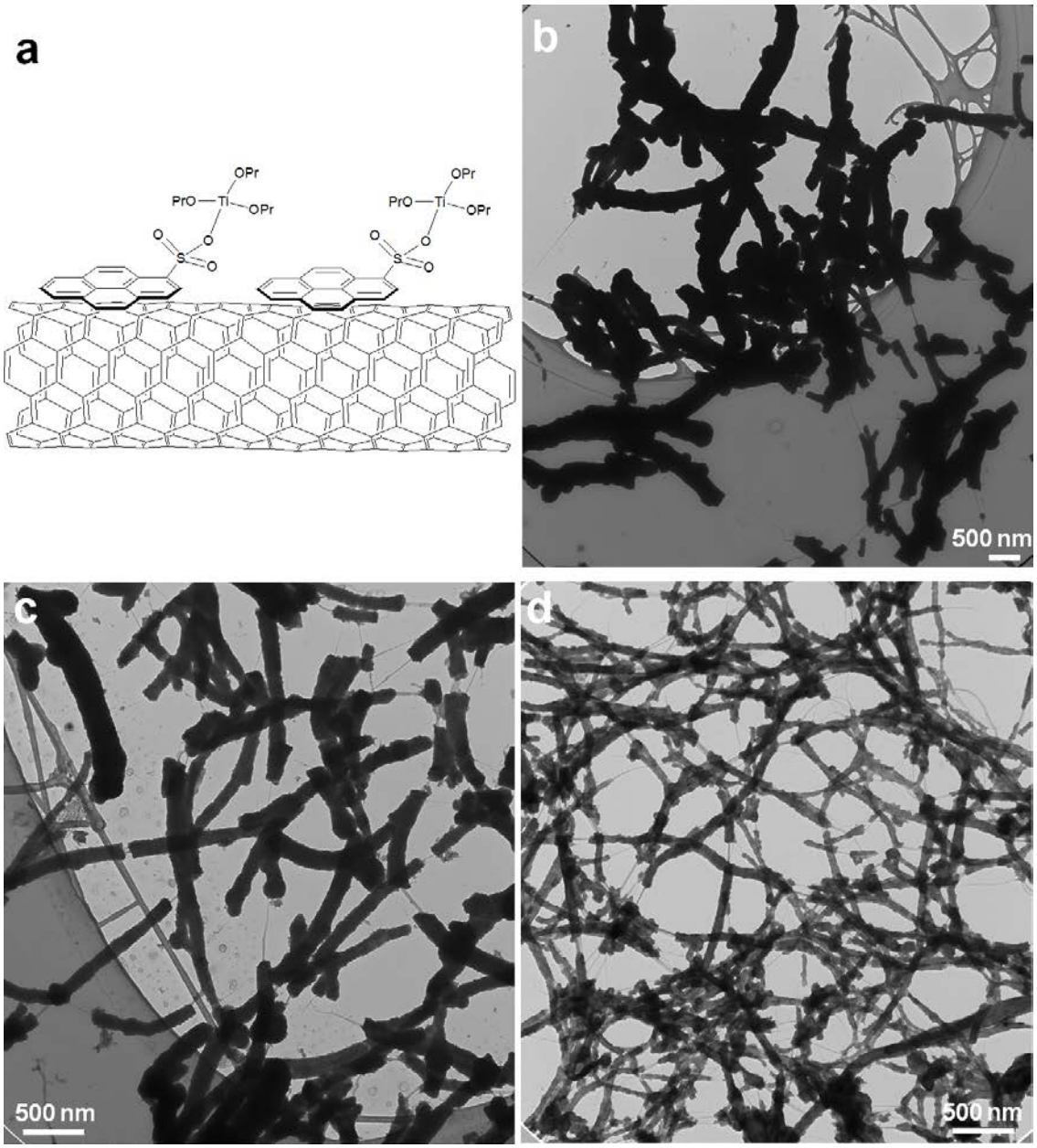

Figure 4-4. Synthesis and morphology control of the SWNT@TiO_2 hybrid nanomaterials from PSA functionalized SWNTs. (a) Schematic illustration of the reaction of $Ti(OiPr)_4$ with SWNT-PSA template. (b-d) SWNT@TiO2 hybrid nanostructures with the condition of (b) 50 μL $Ti(OiPr)_4$ + 3 mL H_2O, (c) 50 μL $Ti(OiPr)_4$ + 1.5 mL H_2O and (d) 25 L $Ti(OiPr)_4$ + 1.5 mL H_2O.

4.4.2 Electrical Behavior and Interfacial Charge Transfer of o-SWNT@TiO_2 Hybrid under UV Illumination

As illustrated in Figure 4-5, a conductive film was fabricated *via* deposition of o-SWNT@TiO_2 hybrid on a Si wafer with SiO_2 insulating layer and interdigitated gold electrodes (10 μm pitch) prepared by standard photolithography (Figure 4-5a). Figure 4-5b and c depict scanning electron microscopy (SEM) images of o-SWNT@TiO_2 hybrid network forming electrical connections between the gold electrodes. Upon illumination with ultraviolet light (365 nm), o-SWNT@TiO_2 hybrid networks showed a decrease in conductance, as demonstrated in Figure 4-5d. When the UV light was turned off, the conductance of o-SWNT@TiO_2 device only underwent a partial recovery, and the rate of conductance increase was much slower compared with the initial decrease in response to UV light (Figure 4-5d). The dramatic decrease in conductance is consistent with the previously reported phenomena of photoexcited electrons being transferred from the conduction band of TiO_2 to the conduction band of SWNTs.[7, 199] Another possible phenomena, generation of the photocurrent in the TiO_2 component was ruled out in this case as it should result in an opposite signal (data not shown here). Since semiconducting-SWNTs demonstrated a typical p-type behavior at ambient conditions,[220] electron transfer to the SWNTs caused reduction of the hole carriers in SWNTs, leading to a decrease in the network conductivity. Such electron transfer has been known to allow a more effective charge separation in TiO_2 and consequently inhibit the electron-hole recombination. The prevention of fast recombination in TiO_2 is indeed observed from the relatively slow recovery of baseline conductance in Figure 4-5d. To further probe this process, similar measurements were done on the SWNT-TiO_2 devices in the presence of oxygen (air). A relatively slower conductance drop in

response to the UV illumination was observed in the air environment, and the recovery was much faster, as shown in Figure 4-6a. The slower UV response and faster recovery in air is in accordance with the addition of electron scavengers (oxygen adsorbed on TiO_2 surface) in the oxygen rich environment that can trap the photoexcited electrons[221-222] and subsequently limit their transfer to SWNTs. This quenching effect was further supported by the conductance recovery observed during the 20% oxygen exposure when SWNT/TiO_2 device was under the UV illumination (Figure 4-6b).

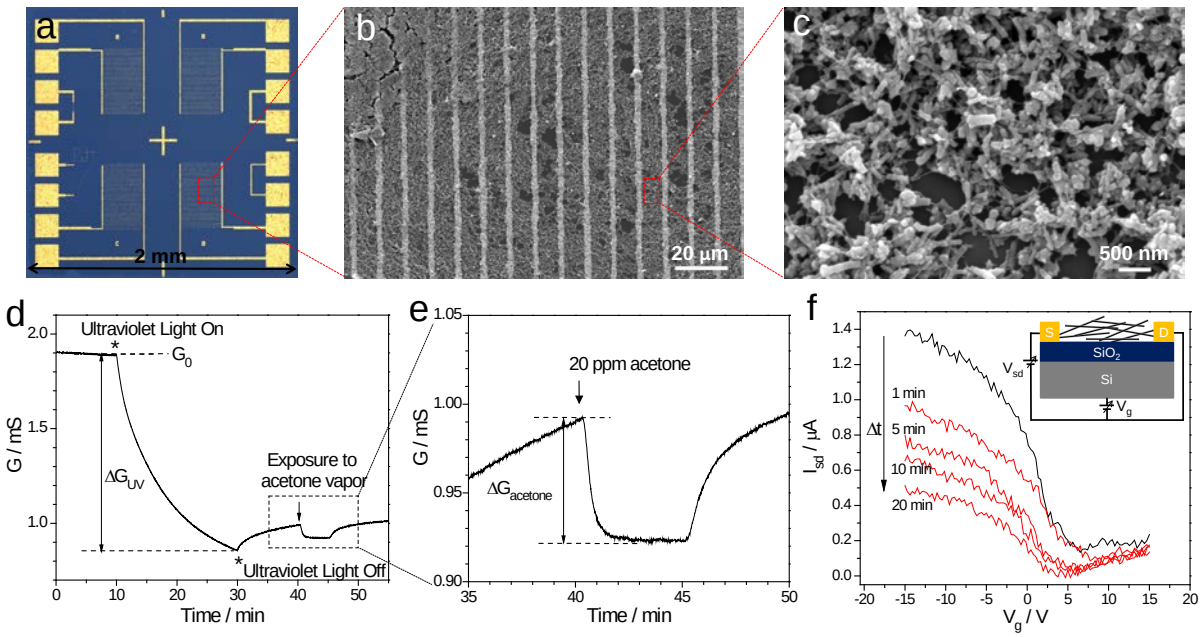

Figure 4-5. Electrical behavior of o-SWNT@TiO_2 devices under UV illumination and chemical exposure. (a) Optical image of a silicon chip with four sets of interdigitated gold electrodes used in this study. (b, c) SEM images of the o-SWNT@TiO_2 core/shell hybrid film deposited between the gold electrodes. (d) Conductance (G) versus time response to ultraviolet light (365 nm) illumination and acetone vapors (20 ppm, balanced in N_2). Arrows indicate beginning and end of acetone exposure. (e) Field-effect transistor (FET) characteristics of SWNT-TiO_2 hybrid network in N_2 under UV illumination at different time intervals (V_{sd} = 3 V). Inset: schematic representation of the o-SWNT@TiO_2 FET device.

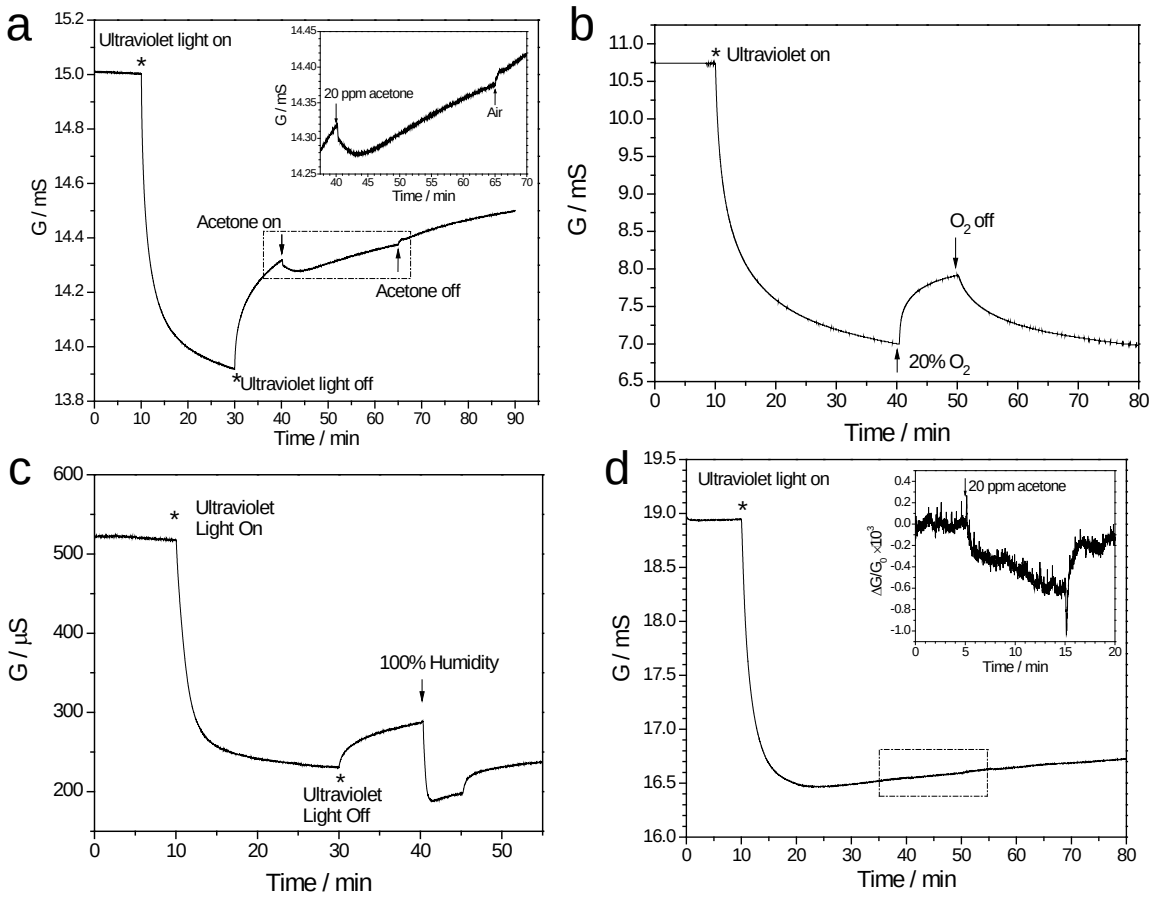

Figure 4-6. Conductance (G) versus time response of the o-SWNT@TiO_2 device to UV light (365 nm) irradiation and other chemical exposures. (a) Response to acetone vapors (20 ppm, balanced in dry air) using air as background and carrier gases. Asterisks indicate the points when UV light was turned on and off, arrows indicate the points when gases/vapors were introduced to the gas flow cell. (b) Response to O_2 (20%). (c) Response to 100% humidity (H_2O vapors). (d) Response to acetone vapor (20 ppm) in high humidity (100%) and air environment.

The o-SWNT@TiO_2 hybrid network was also tested in a field-effect transistor (FET) device configuration using interdigitated gold electrodes as source/drain and a Si substrate as back gate. As shown in Figure 4-5e, o-SWNT@TiO_2 hybrid demonstrated p-type FET characteristics, similar to the random network composed of pristine SWNTs at ambient conditions.[114, 220] This indicates that the transistor characteristics of the hybrid are determined by SWNT components. Upon UV illumination, the I-V_g curve of SWNT-TiO_2 tilted and shifted to a negative gate voltage (negative threshold voltage) and a smaller current. The change in FET characteristics at zero gate voltage matches the conductance versus time measurements (Figure 4-5d). A shift towards negative gate voltage generally indicates a decrease in hole carrier concentration for the p-type semiconductor after UV exposure. This is also consistent with the charge transfer from excited TiO_2 to semiconducting SWNTs. Due to the presence of metallic-SWNTs, the SWNT-TiO_2 network also demonstrated a baseline conductance when the transistor was adjusted to the "off state". The decrease in current that was simultaneously observed upon UV illumination suggests creation of scattering centers at the SWNT-TiO_2 interface that influence the conductivity of metallic SWNTs as well. The emerged ambipolar characteristic of the SWNT-TiO_2 transistor is another consequence of the reduction of hole carriers and is in accordance with similar studies on the bare SWNT devices.[106] The summarized process of photoexcitation and subsequent electron transfer is illustrated in Figure 4-8a.

Chemical sensitivity provides useful information on the process of surface adsorption[150, 220] and catalytic reactions.[223] Moreover, it also characterizes the potential of hybrid materials for practical application in chemical detection. When the UV light was turned off, the slowly recovering conductance of SWNT-TiO_2 went close to a steady state after 10 min in N_2 and set up a new baseline that could be utilized for chemical sensitivity tests. As shown in Figure 4-5d,

exposure to 20 ppm acetone vapors led to a fast decrease in the conductance of o-SWNT@TiO_2 device, with complete recovery to the baseline when acetone vapor exposure was terminated (response to higher acetone concentrations is shown in Figure 4-7a). This photoinduced acetone sensitivity is different from previously reported sensors based on CNTs[220, 224-226] and provides useful information on the molecular interactions between nanohybrid and acetone molecules with implications for future development of acetone sensors and catalysts for the photooxidation of acetone.

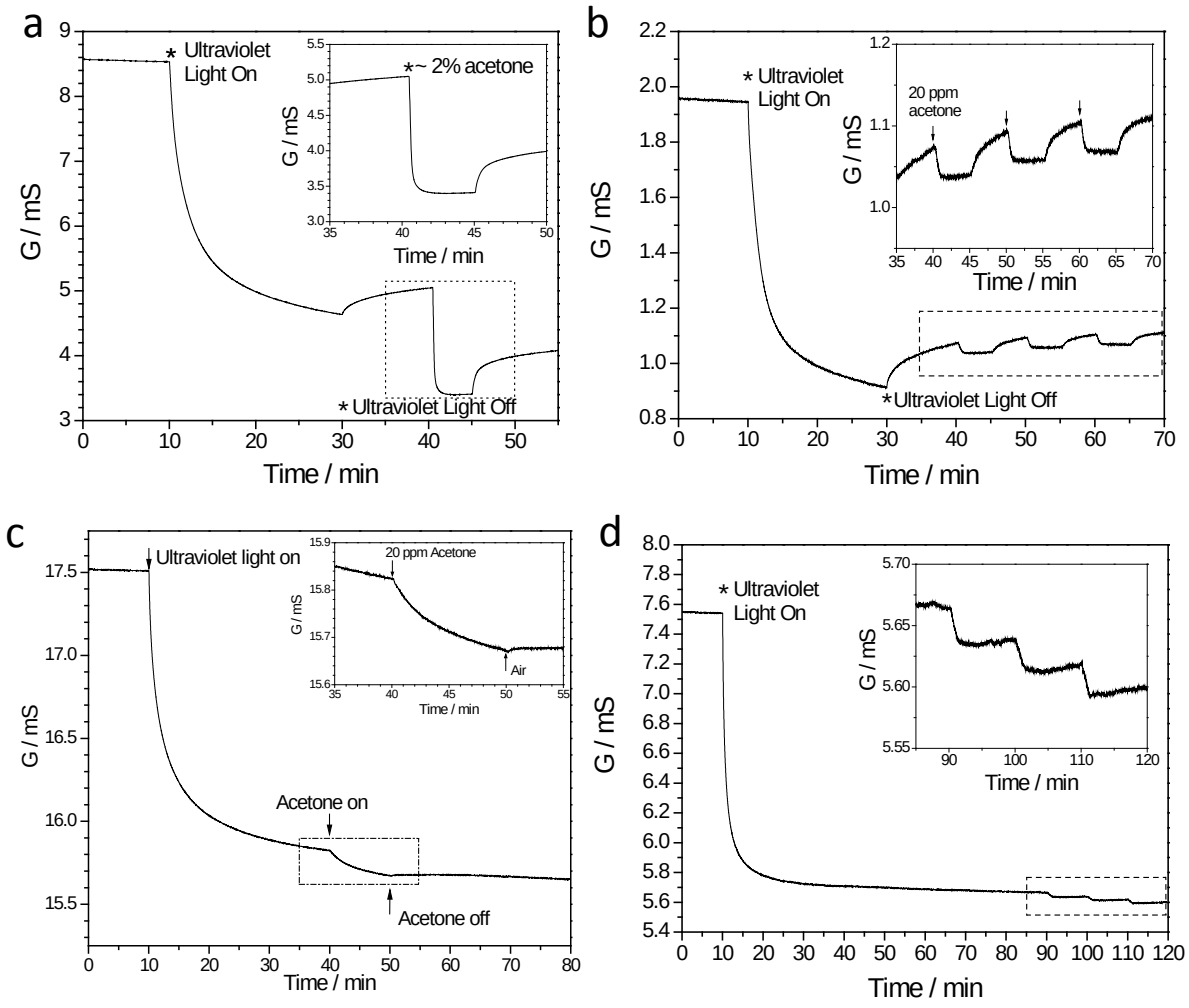

Figure 4-7. Different operation scheme of the o-SWNT@TiO_2 acetone sensor. **(**a) Conductance (G) versus time response of the o-SWNT@TiO_2 device upon irradiation of ultraviolet light (365 nm) and exposure to acetone vapors (~2%, generated by bubbling dry N_2 through liquid acetone). Asterisks indicate the points when UV light was turned on and off, arrows indicate the points when acetone vapor was introduced to the gas flow cell. Inset depicts the enlarged figures of the conductance change upon exposure to acetone vapors. (b) Electrical response of the o-SWNT@TiO_2 device to three concessive acetone vapor exposures (20 ppm). (c) Electrical response of the o-SWNT@TiO_2 device to acetone vapor exposure (20 ppm) while UV light was kept on. (d) Electrical response of the o-SWNT@TiO_2 device to three concessive acetone vapor exposures (20 ppm) while UV light was kept on.

4.4.3 Charge transfer efficiency and acetone reactivity of the photoexcited hybrid systems.

In order to confirm our proposed interfacial process in the SWNT-TiO_2 hybrids and to better understand the factors that regulate their electrical behavior, other SWNT-TiO_2 hybrid systems with different morphologies and interface conditions were also synthesized and analyzed. Specifically, commercially available pristine or oxidized SWNTs and Anatase TiO_2(A) samples were mixed by either mechanical mixing (using sonication) or covalent attachment (see methods for details). Similar electrical measurements were performed on all these SWNT-TiO_2 hybrid systems and their UV and acetone responses (defined in Figure 4-5d) are summarized in Figure 4-8b.

First, it could be noticed that addition of TiO_2 dramatically increased the UV response of the device compared with bare SWNTs network (either pristine or oxidized SWNTs), and larger UV responses were observed for a higher amount of TiO_2 in all hybrid systems, regardless of their interconnections with SWNTs. Such difference in the magnitude of conductance change and its correlation with the TiO_2 loading further confirmed that the electrical behavior of SWNT-TiO_2 hybrid systems was a result of the interfacial charge transfer process, different from the photoinduced molecular desorption mechanism previously proposed for bare SWNTs devices.[106, 227-228] Moreover, while pristine SWNTs and oxidized SWNTs showed similar UV and acetone sensitivities when mechanically mixed with anatase TiO_2(A) nanocrystals, covalent attachment between TiO_2 nanocrystals and SWNTs led to a significant increase in the UV response (o-SWNT-TiO_2(A) vs. o-SWNT&TiO_2(A) in Figure 4-8b). This difference clearly indicates that covalent linkage between TiO_2 and SWNTs led to enhanced electron transfer efficiency and therefore a better charge-hole separation in the hybrid system, while the type of SWNTs (pristine

vs. oxidized) had less influence. Overall, o-SWNT@TiO_2 presented the largest UV response, because of increased covalent linkage and interface area between SWNT and TiO_2. We can conclude from all these results that this hybrid system presents an efficient electronic transfer at interface upon UV irradiation.

Increasing the amount of TiO_2 resulted in enhanced acetone sensitivity in all nanohybrid systems, which confirmed its role of recognition layer (Figure 4-8b). Compared with other hybrid systems, o-SWNT@TiO_2 core/shell hybrid demonstrated the highest acetone sensitivity, which is probably due to two distinct factors: i) the abundant covalent bonding between SWNTs and TiO_2 facilitates the electronic coupling and interactions across the hybrid interface, leading to a more efficient and sensitive interfacial charge transfer (as also indicated by its best UV response); and ii) the less ordered structure of as-synthesized TiO_2 (amorphous in nature with few small crystalline areas) offers more oxygen vacancies or unsaturated surface Ti centers that were more reactive to acetone molecules, as compared to the highly crystalized commercial TiO_2 nanoparticles (Figure 4-8b).

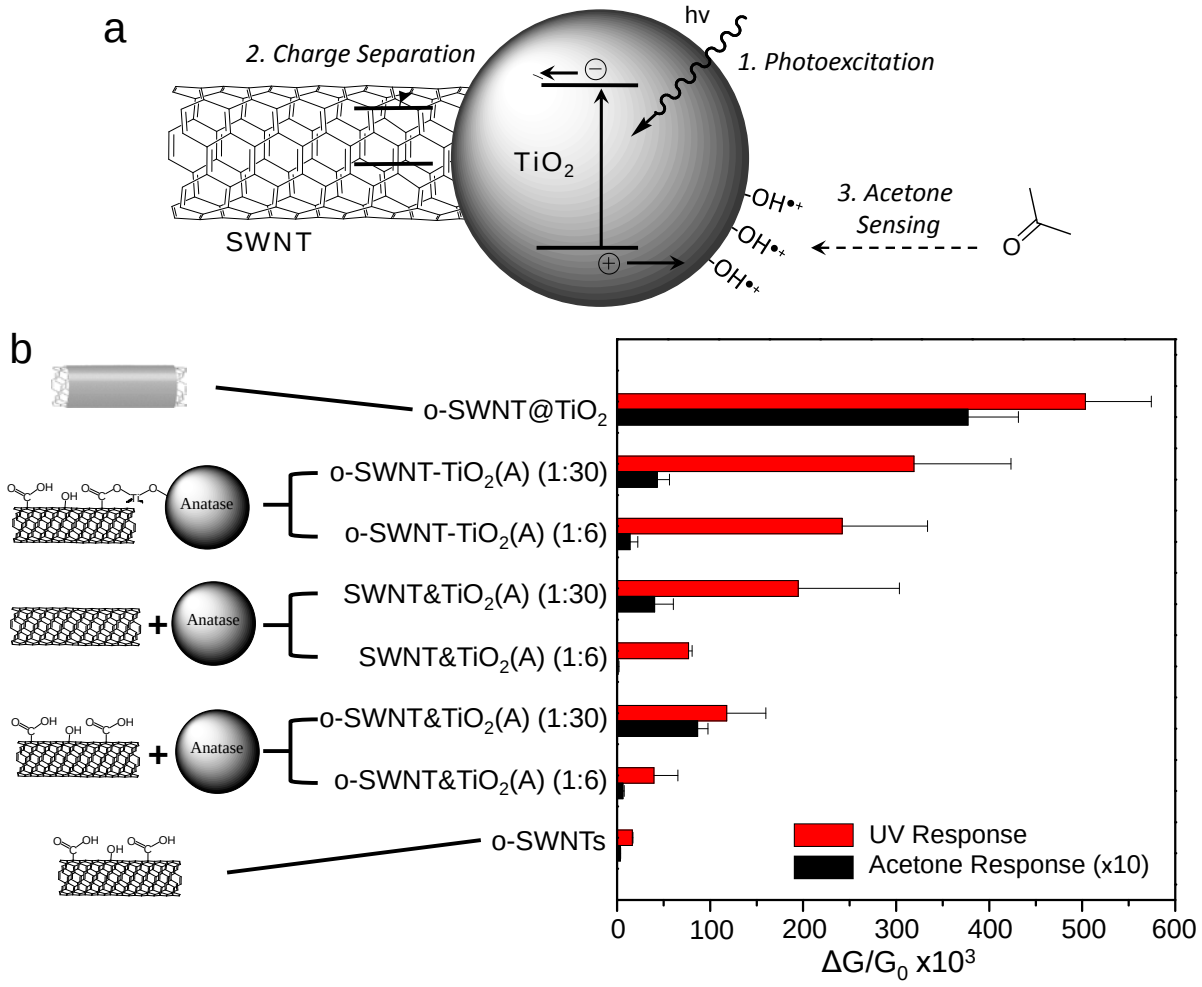

Figure 4-8. Schematic illustration of UV illumination, charge separation and acetone sensing and comparison of the electrical responses of different SWNT-TiO_2 hybrid systems. (a) Schematic of the band structure of SWNT-TiO_2 hybrid, photoinduced charge separation and acetone sensitivity. (b) Schematic illustrations (left) of different SWNT-TiO_2 hybrid systems including: oxidized SWNTs (o-SWNTs), as-prepared o-SWNT@TiO_2 core/shell hybrid, covalently linked anatase nanopowders with o-SWNTs (o-SWNT-TiO_2(A)), mechanically mixed pristine SWNTs and anatase nanopowders (SWNT&TiO_2(A)), and mechanically mixed o-SWNTs and anatase nanopowders (o-SWNT&TiO_2(A)). The numbers after each label indicate the weight ratio of SWNTs to TiO_2 in the hybrid. The right panel illustrates the UV (red bars) and acetone responses (black bars) of each hybrid system, with standard deviation (n=15). For comparison, acetone responses were multiplied by a factor of ten.

4.4.4 Theoretical Simulations of the SWNT-TiO_2 Interaction and Acetone Sensing.

The main findings on the charge transfer efficiency and acetone sensitivity of different SWNT-TiO_2 hybrid systems obtained by electrical measurements were further supported by Density Functional Theory (DFT) calculations. Figure 4-9a depicts the optimized binding configuration of a $Ti_{10}O_{20}$ cluster on a pristine (14,0)-SWNT surface, while Figure 4-9b and c illustrate the adsorption of the same cluster, respectively of a hydrogenated TiO_2 cluster on a SWNT functionalized with an O atom with formation of a covalent Ti-O-C linkage. For each of these configurations, corresponding binding energies of the $Ti_{10}O_{20}$ ($Ti_{10}O_{20}H_4$) cluster on SWNT are also indicated. The interfacial charge distributions (with the calculated amount of electron transfer) and the charge differential plots are also listed in Figure 4-9d to f and g to i, respectively. A negligible binding energy and very small charge transfer between the TiO_2 cluster and the pristine SWNT (Figure 4-9a, d, g) indicated weak mutual interactions. This interaction was significantly increased upon formation of a covalent linkage facilitated by the presence of either adsorbed O (44.7 kcal/mol in Figure 4-9b vs. 3.1 kcal/mol in Figure 4-9a), with direct enhancement of the interfacial charge transfer (-0.41 e in Figure 4-9e vs. -0.02 e in Figure 4-9d). The enhanced interfacial electronic coupling (also see Figure 4-9h) through covalent linkage is also in agreement with UV response measurements. Furthermore, hydrogenation of the $Ti_{10}O_{20}$ cluster showed a significant influence on the charge distribution at the hybrid interface (Figure 4-9f and i), indicating the sensitivity of the interfacial charge distribution within the SWNT-TiO_2 nanohybrids upon binding of any redox chemical species on the surface active site.

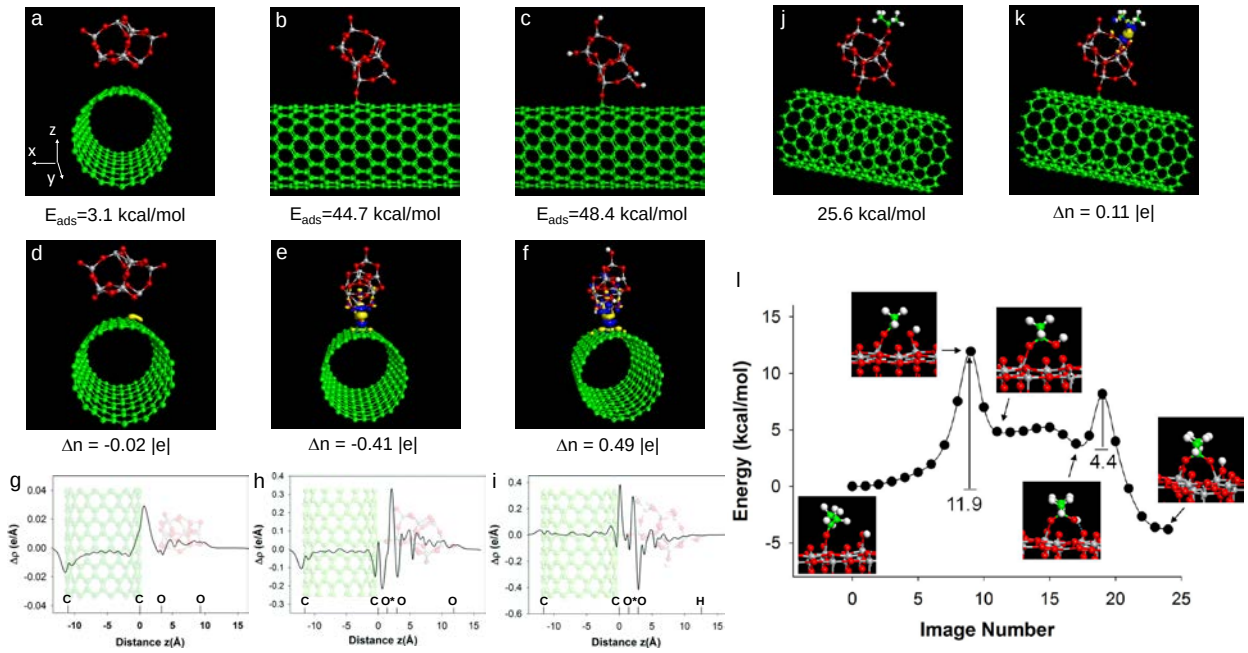

Figure 4-9. Density Functional Theory (DFT) simulation of the electronic coupling and acetone sensing process. a, Representative adsorption configuration of a $Ti_{10}O_{20}$ cluster on a pristine (14,0) single-wall carbon nanotube (SWNT). b, Adsorption configuration of a $Ti_{10}O_{20}$ cluster on a (14,0) SWNT through Ti-O-C linkage. c, Adsorption of a hydrogenated (with formation of four OH bonds) $Ti_{10}O_{20}$ cluster on the oxygen-decorated SWNT. C atoms are green, Ti atoms are gray, O atoms are red and H atoms are white. The adsorption energies (E_{ads}) of $Ti_{10}O_{20}$ cluster are indicated for each case in the lower part of the top panels. d-f, Charge difference maps of the $Ti_{10}O_{20}$ cluster for the binding configurations illustrated in panels a-c, respectively. The corresponding Bader charges (Δn) transferred from SWNT (with O in e and f) to $Ti_{10}O_{20}$ are shown in each case. In panel d the indicated isosurfaces correspond to values of 0.004 $e^-/Å^3$ (yellow) and -0.0015 $e^-/Å^3$ (blue) while in panels e and f to values of +0.02 $e^-/Å^3$ (yellow) and -0.02 $e^-/Å^3$ (blue). g-i, Plane averaged charge density different plots for configurations a-c at different z-planes, respectively. j, Adsorption configuration of acetone on-top of a Ti site (η^1-acetone) on the SWNT-O-$Ti_{10}O_{20}$ hybrid and the corresponding E_{ads}. k, Charge difference map of acetone for the binding configurations in j and corresponding Bader charge transfer from acetone to $Ti_{10}O_{20}$ cluster. l, Minimum energy pathway for reaction of a η^1-acetone molecule initially co-adsorbed near a terminal hydroxyl OH_t group on anatase (101) surface leading to formation of a $(CH_3)_2CO$-OH complex (configurations #11 and #17) followed by transfer of a H atom to a surface bridging oxygen and formation of an η^2-acetone-O adatom complex (configuration #24).

We further analyzed the adsorption of an acetone molecule on the TiO_2 cluster. A representative binding configuration and the corresponding charge transfer at the acetone-oxide interface are illustrated in Figure 4-9j and k. An electron transfer of 0.11 e from acetone to the hybrid was observed (Figure 4-9k), indicating a partial oxidation of the acetone molecule, which explained the observed reduction of the hole carriers of the p-type o-SWNT@TiO_2 hybrids (as discussed in section 4.5.2). We further assume that the effect of UV illumination was to generate enough reactive sites for acetone molecules on the TiO_2 surface (such as hydroxyl radicals) that were probably occupied by other molecules (such as water) before the UV exposure. Furthermore, several possible intermediate configurations from the reaction between an adsorbed acetone (in a η_1-configuration at a Ti five-folded site) and a nearby terminal hydroxyl (OH_t) group (that mimics the hydroxyl radical generated through UV illumination) on the TiO_2 anatase (101) surface were calculated with their energy profile (Figure 4-9l). We observed relative low energy barriers for both the direct and reverse reactions of acetone-OH_t and formation of acetone-O adatom complex. This behavior is consistent to the observed reversible electrical signals in the sensor tests. In particular, for the acetone-O adatom configuration a new band in the density of states (DOS) was observed within the band gap of TiO_2.[98] This intermediate band indicated that adsorbed acetone molecules could further serve as hole traps on the photoexcited TiO_2 surface, and could be further oxidized if under continuous UV illumination. These theoretical results are also consistent with our observations that during the sensing measurements, the response of SWNT-TiO_2 device was actually irreversible if the UV light was kept on (see Figure 4-7). This irreversible detection with *in situ* UV exposure was indeed a result of the irreversible oxidation of the adsorbed acetone on the photoexcited TiO_2. The overall mechanism

of photoinduced acetone sensitivity of SWNT-TiO_2 indicated by the experimental and theoretical results is also summarized in Figure 4-8a.

4.4.5 Acetone sensing with o-SWNT@TiO_2 and its potential in the breath detection.

The photoinduced acetone sensitivity of o-SWNT@TiO_2 hybrid can be utilized as a promising sensory tool for the electrical detection of acetone vapors. Figure 4-10a depicts the electrical response of o-SWNT@TiO_2 devices (in a chemiresistor configuration) upon exposure to varying concentrations of acetone vapors at ppm level. The baseline of the sensor device was first set up through UV illumination, and four pulses of acetone vapors (diluted with N_2) with increasing concentrations (indicated by red bars) were subsequently introduced into the gas flow cell. As shown in Figure 4-10a, multiple exposures were successfully measured as each electrical response reached a full recovery after respective pulses without any additional operation. Device variations were also tested and results (shown in Figure 4-11) indicated a good reproducibility of the o-SWNT@TiO_2 acetone sensors. Different response rates were observed to the varying concentration of acetone vapors. The response signal did no saturate at lower concentration (2 ppm) during the 180 seconds of each acetone exposure, but the device reached equilibrium in a shorter time at higher concentrations (t_{90} = 50s for 20 ppm). We found a linear relationship between the electrical response rate at the first 60 seconds (fast response region) and the acetone concentrations, which could serve as calibration curve for the sensor (Figure 4-10b). For 180 seconds of exposure time, we calculated a signal to noise ratio (S/N) of 14 for 2 ppm of acetone, and a detection limit of 0.4 ppm was determined (using S/N=3) for our o-SWNT@TiO_2 acetone sensor. This detection limit is lower compared with previously reported SWNT-based detection of acetone,[220, 224-225] which is limited by its weak electronic interactions with SWNTs.[226]

Although utilizing TiO_2 as a sensitive coating to CNTs has been previously reported,[229] our results demonstrate that the photoexcited o-SWNT@TiO_2 has improved sensitivity to acetone.

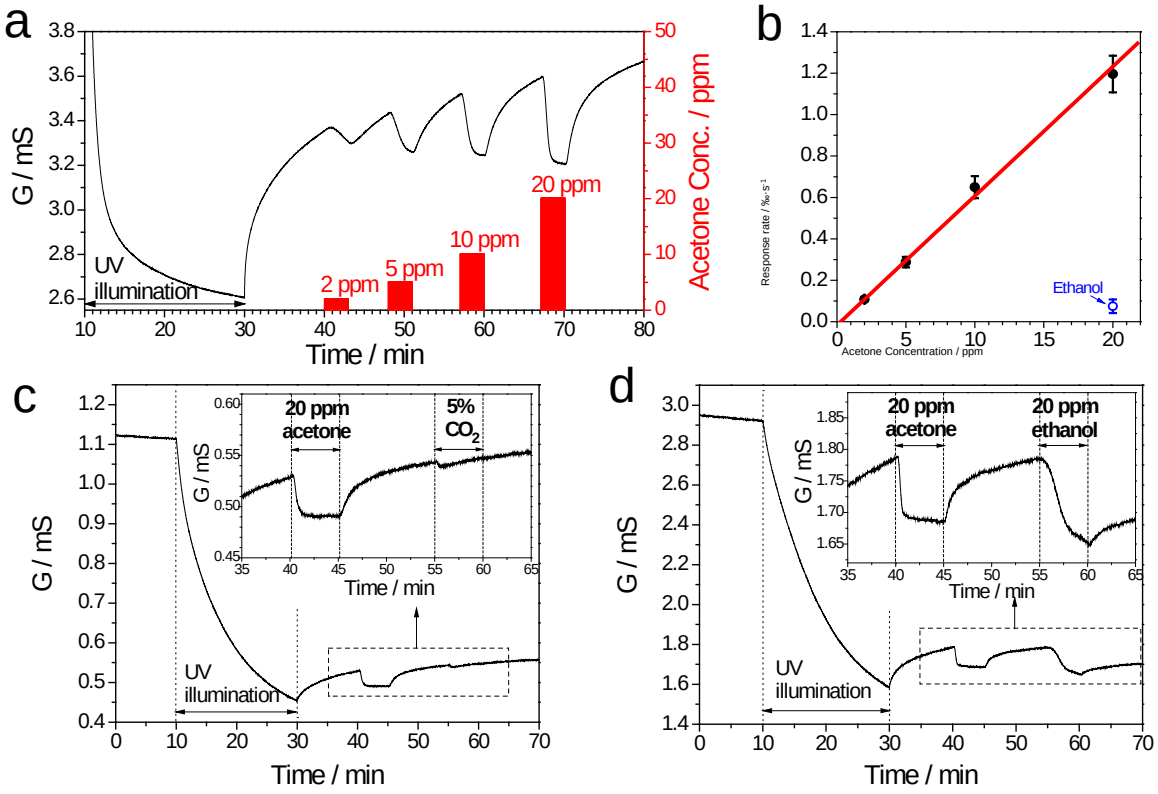

Figure 4-10. Detection of acetone vapors using o-SWNT@TiO_2 devices. Electrical response of o-SWNT@TiO_2 devices to varying acetone concentrations: (a) Conductance (G) response of the device to acetone vapors of varying concentrations (2 ppm, 5 ppm, 10 ppm and 20 ppm, balanced in N_2) after UV illumination. (b) Acetone response rate (*i.e.*, relative conductance change per unit time) of o-SWNT@TiO_2 devices (n=10). (c, d) Cross sensitivity of the o-SWNT@TiO_2 device between 20 ppm acetone and 5% CO_2 (c) 20 ppm ethanol (d).

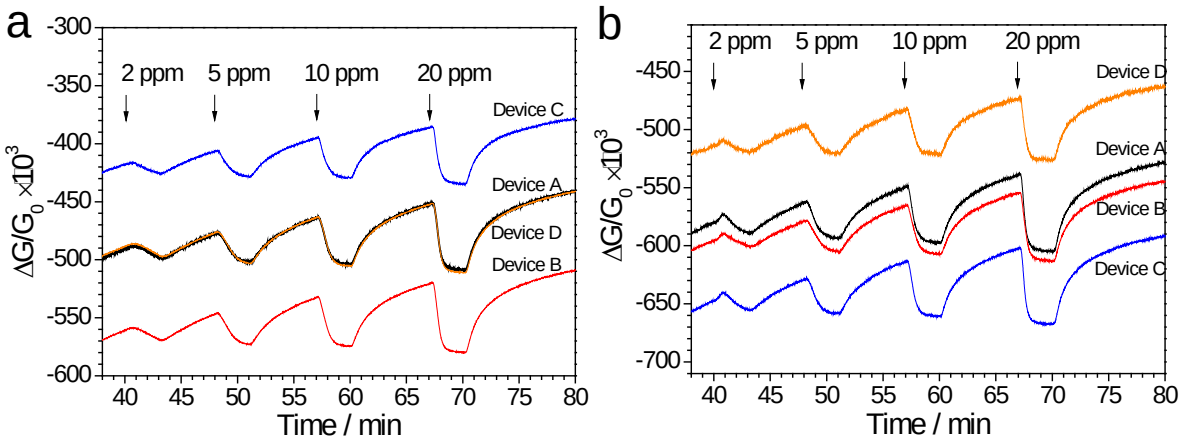

Figure 4-11. Deviation of o-SWNT@TiO_2 acetone sensor devices in a same chip and between different chips. (a) and (b) each depicts 4 o-SWNT@TiO_2 devices within a same chip upon exposure (3 min) to acetone vapors with varying concentrations (2, 5, 10 and 20 ppm in N_2).

To evaluate the potential of these acetone sensors for breath analysis, cross sensitivity tests to major components of human breath (O_2, CO_2, H_2O and ethanol) and other possible breath biomarkers (NH_3, H_2, CO and NO)[218, 230-231] were also performed. We did not observe any significant response when o-SWNT@TiO_2 was exposed to 5% CO_2, as shown in Figure 4-10c. The negligible CO_2 response of o-SWNT@TiO_2 is in accordance with the low binding energy and reactivity of CO_2 molecules on the TiO_2 surface.[232] For the similar reason, no significant cross-sensitivity was observed for other trace biomarkers, indicating a potentially selective detection of breath acetone using o-SWNT@TiO_2 in case of other metabolic conditions (see Figure 4-12 for details). We have already demonstrated that O_2 had a larger effect on the excited o-SWNT@TiO_2 as electron scavenger, and cross-sensitivity to humidity vapor was also observed due to its molecular interaction with both TiO_2 and SWNTs (Figure 4-6b and c). Despite the

sensitivities to O_2 and H_2O, the o-SWNT@TiO_2 sensor was successfully utilized to detect 20 ppm of acetone vapor in both air and high humidity background, with increased noise level and higher detection limit (Figure 4-6d).

Ethanol is another type of hole scavenger and could be present in human breath as a result of the alcohol consumption. As shown in Figure 4-10d, photoexcited o-SWNT@TiO_2 demonstrated a comparable sensitivity yet a different response dynamic towards 20 ppm acetone and ethanol vapors. This result indicated different types of adsorption or reaction occurred on the photoexcited TiO_2 surface for these two analytes. We hypothesize that dynamics of the electrical response to chemical molecules are closely related to their binding energies. For example, in a bare carbon nanotube or graphene sensors, rapid response arises from the adsorption of acetone molecules on the low-energy binding sites, while slow response comes from the adsorption of acetone molecules on the high-energy binding sites.[150]

DFT calculations were employed to provide the adsorption energy of acetone and ethanol molecules in case of dense binding on the TiO_2 surface. As demonstrated in Figure 4-13, acetone binding energies significantly decrease with the increasing number of molecules (up to three in Figure 4-13d) on a limited area of TiO_2 surface, due to the steric repulsions between their two methyl groups. This result indicates that a higher coverage of acetone molecules on a TiO_2 surface is energetically unfavorable, which is probably why acetone response of SWNT/TiO_2 reached to an equilibrium value more rapidly. On the other hand, increased coverage of ethanol molecules results in increased adsorption energy due to the hydrogen bonding between adjacent adsorbed or dissociated ethanol molecules. This higher energy adsorption configuration at high molecular coverage is consistent with the slow response region observed for SWNT/TiO_2

devices during the ethanol exposure. Moreover, the fact that ethanol can dissociate on the TiO_2 surface explains the slow and incomplete recovery after the ethanol exposure.

Due to the different response dynamics, electrical response of o-SWNT@TiO_2 to acetone and ethanol vapors with comparable concentrations can be distinguished via their response rates (as demonstrated in Figure 4-10b). For the practical sensor consideration, our results indicate that high concentrations of alcohol vapors in human breath could result in false positives during the analysis of breath acetone, and cautions or additional steps have to be taken in such case.

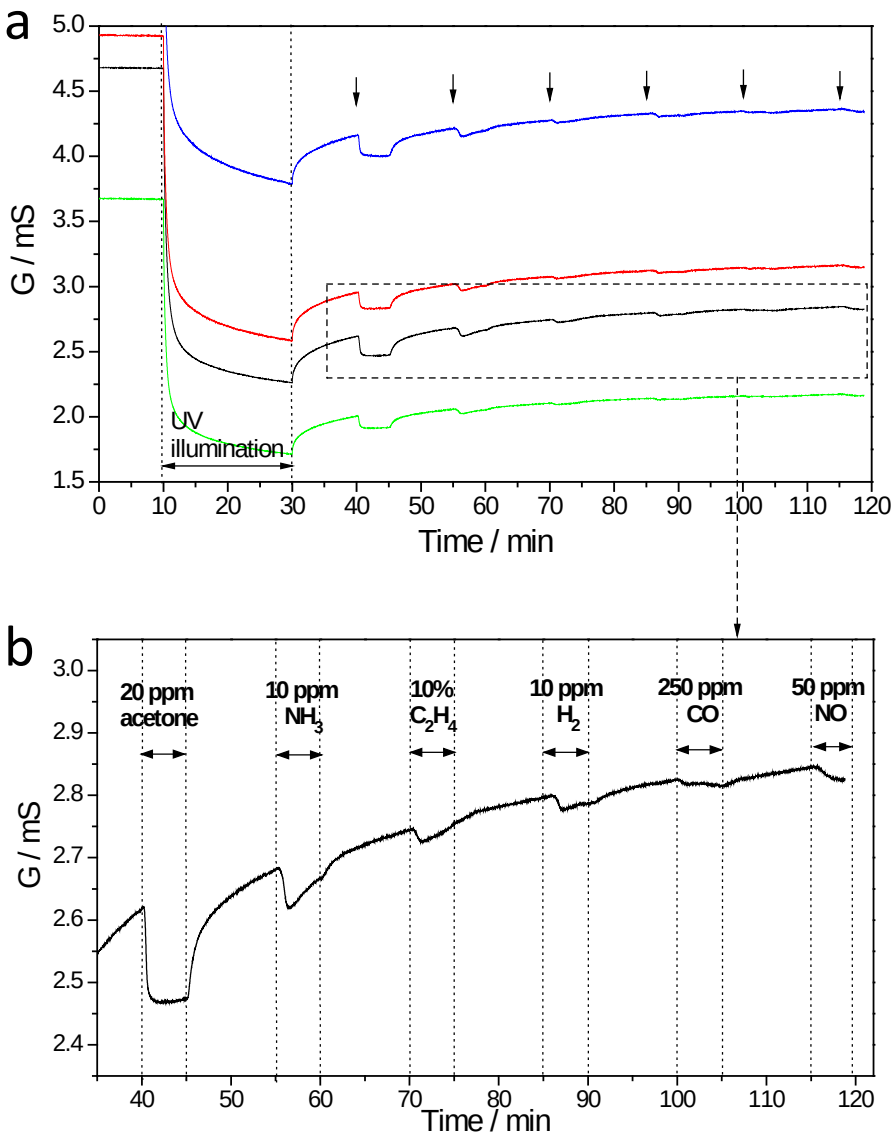

Figure 4-12. Cross-sensitivity tests. (a) Conductance (G) versus time response of the o-SWNT@TiO_2 devices to UV light (365 nm) irradiation and exposure to different breath markers, arrows in (a) indicate six exposures each to an individual gas/vapor, which in turn are 20 ppm acetone, 10 ppm NH_3, 10% C_2H_4 (in analogue to isoprene in breath), 10 ppm H_2, 250 ppm CO, and 50 ppm NO. (b) An enlarged figure of dashed area in (a).

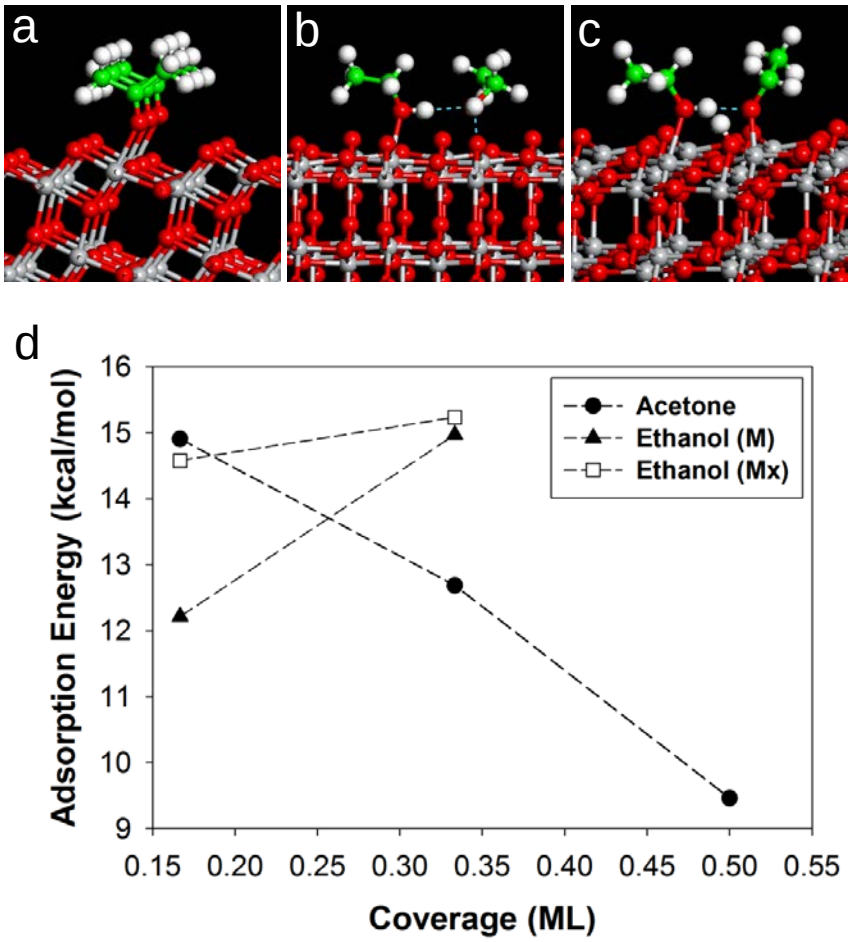

Figure 4-13. Simulation of dense adsorption of acetone and ethanol molecules on the TiO_2 surface. Pictorial view of the adsorption configurations of (a) acetone and methanol (b,c) on anatase (101) surface. Panel (a) illustrates the binding state of acetone at Ti-five folded (Ti(5f)) site at 0.5 ML coverage. Panel (b) represents the adsorption configuration of two ethanol molecules adsorbed in a molecular state (M) at two nearby Ti(5f) sites while panel (c) represents the configuration of a mixed state (Mx) in which one of the two molecules adsorbs in a dissociated state with formation of an OC_2H_5 radical and a bridging hydroxyl. In panel (d) the variation of the adsorption energy of acetone and ethanol molecules with coverage is indicated. For the ethanol case the M states correspond to molecular adsorption while the Mx states denote mixed configurations.

4.5 CONCLUSION

In summary, we have developed facile and scalable synthesis of the o-SWNT@TiO_2 hybrid nanostructures with controlled core/shell morphology. Unique electrical behavior of this hybrid nanomaterial was observed in response to the UV illumination and subsequent chemical exposure. Based on both experimental and theoretical studies of a group of systematically designed SWNT-TiO_2 hybrid systems, we established a fundamental understanding of interfacial charge transfers between photoexcited TiO_2 and SWNTs with different morphologies and interfacial conditions. The ability to monitor the efficiency of electron-hole separation during the UV excitation with the SWNTs as an electrical probe would benefit the future design and development of SWNT-TiO_2 based photovoltaic devices or photocatalysts.

Utilizing the SWNT-TiO_2 devices as chemiresistors, we demonstrated ultrahigh acetone sensitivities with linear and reversible responses at the concentration range between 2 to 20 ppm, and a calculated detection limit of 0.4 ppm. The ultrahigh sensitivity to ppm level of acetone vapors, fast and reversible response, together with miniature size and room temperature operation makes this SWNT-TiO_2 nanohybrid a promising sensing platform that could find applications in the detection of breath acetone. The development of a micro-sized low-power electronic breath acetone sensor device could further benefit personal healthcare by serving as a convenient and low-cost diagnostic tool for diabetes or a novel and high-throughput analytical method in the clinical studies of metabolic disorders.

5.0 SYNTHESIS OF ONE-DIMENSIONAL SIC NANOSTRUCTURES FROM FUNCTIONALIZED CARBON NANOTUBES - A "GLASSY BUCKYPAPER"

5.1 CHAPTER PREFACE

Materials contained in this chapter were published as a research article in *ACS Applied Materials & Interfaces*; figures used in this chapter have been reprinted with permission from *ACE Appl. Mater. Interfaces* **2013**, *5*, 1928-1936. (listed as reference 233 in bibliography section).

List of Authors: Mengning Ding and Alexander Star.

Author Contributions: DMN and AS designed the experiments and wrote the manuscript, DMN performed the experimental work.

5.2 INTRODUCTION

Silicon carbide (SiC) has been widely recognized as a versatile material with tremendous industrial applications because of its unique mechanical, electrical and thermal properties.[234] The synthesis of SiC has been extensively explored during the past century and many general synthetic methods have been summarized in great detail. Recently, the research focus has been shifted to the fabrication of one-dimensional (1-D) SiC nanostructures because of their potential applications in nanoelectronics as analogues to carbon nanotubes[103] and Si nanowires.[235] Due to their high thermal stability, chemical inertness, and high mechanical strength, 1-D SiC nanostructures are especially promising for the employment in high power, high frequency and high temperature environment.[236-237] Growth of 1-D SiC nanostructures has been carried out by a variety of methods including chemical vapor deposition (CVD),[238-242] arc discharge,[243-244] pyrolysis of polysilazane,[245] crystal growth from solution,[246-247] carbothermal reduction,[248-249] vapor-solid reaction between gaseous carbon and Si substrate,[240, 250] and through a confined reaction between Si precursors and carbon nanofibers[251-253] or carbon nanotubes (CNTs).[254-259] This latter approach has its own advantages due to the easy processing of free standing carbon nanotube samples, and the increasing industrial production and declining cost of carbon nanotubes. Lieber and co-workers first demonstrated the synthesis of SiC nanorods through the reaction between carbon nanotubes and gaseous SiO or SiI_4.[254] In this approach CNTs acted as both carbon source and template for the growth of the one-dimensional nanostructures. Similar approaches were reported following this work with different Si sources including sputter-coated Si,[255] SiO vapor,[256-258] and Si vapor.[259] Despite the successful synthesis of one-dimensional SiC

nanostructures, all of these methods required the generation of toxic Si-containing vapor that complicated the manufacturing process, and caused significant waste of the Si precursors. Here we report a facile and scalable approach where adsorbed silicate was employed as the Si precursor to react with carbon nanotube templates. The silicate was introduced by washing the "buckypaper" of carbon nanotubes with aqueous sodium silicate solution. Since sodium silicate is also known as water glass, the resulting SWNT-silicate film is designated here as "glassy buckypaper". This "glassy buckypaper" was further used to produce the SiC nanostructures after high-temperature calcination. The solution-based approach to prepare "glassy buckypaper" and the solid state reaction for the synthesis of SiC has the advantages of easy operation, scalability and potentially low-cost production. Moreover, it prevents the waste of Si precursors because the sodium silicate solution used in each synthesis can be recycled and reused.

5.3 EXPERIMENTAL SECTION

Materials: Pristine single-walled carbon nanotubes (SWNTs, P2) were obtained from Carbon Solutions, Inc. Multi-walled carbon nanotubes (MWNTs) were obtained from Bayer MaterialScience, Inc. Sodium metasilicate, n-hydrate ($Na_2SiO_3 \cdot 9H_2O$) was purchased from J T Baker, Inc. All organic solvents were purchased from Sigma Aldrich and used as received. High purity argon and hydrogen gas cylinders (Grade 5.0) were purchased from Valley National Gas, Inc.

Preparation of "buckypaper" and "glassy buckypaper": Single-walled carbon nanotubes (SWNTs, 10.0 mg) were suspended in ethanol (10.0 mL) by 15 min of sonication (Branson 5510 bath sonicator). The suspension was filtered (with PTFE filter, 2 μm) and then washed with DI

water (5 mL x 3) and then ethanol (5 mL x 3). A continuous and rigid SWNTs network thin film (known as “buckypaper”) was formed on top of the filter membrane after this process. While still on the filter, the “buckypaper” of SWNTs was subsequently washed with 0.1 M Na_2SiO_3 aqueous solutions (2 mL x 5). The as-prepared SWNT-silicate composite maitained a film structure, and was then collected and dried in oven at 120 °C overnight. A digital photograph image of the resulting composite film, designated as “glassy buckypaper”, is demonstrated in Scheme 1.

Synthesis of SiC nanorods: The “glassy buckypaper” was placed in the middle of an alumina tube inside a tube furnace (CM Furnaces, Inc.). A gas mixture (800 sccm of Ar flow mixed with 50 sccm of H_2 flow) was introduced into the alumina tube to create the reaction environment. The temperature of the furnace was increased to 1300 °C, and was kept for different time periods from 1 to 10 hr. After 10 hr of reaction at 1300 °C, the product was then burned in air at 700 °C for 3 hr to remove all the unreacted carbon to afford SiC nanorods. Alternative synthesis conditions of 1500 °C for 1 hr resulted in a similar SiC nanorod product. SiC product synthesized under these conditions required no further thermal treatment. Figure 5-1 illustrates the detailed processes of this synthetic approach.

Synthesis of SiC nanowires: The “glassy buckypaper” was placed in the middle of an alumina tube inside a tube furnace. A gas mixture (800 sccm of Ar flow mixed with 50 sccm of H_2 flow) was introduced into the alumina tube to create the reaction environment. The furnace was heated to 1400 °C, and the heating was quickly stopped once the temperature reached the desired value (a so-called “fast reaction”). A small amount of SiC nanowires with impurities was produced by this procedure. The product was then burned in air at 700 °C for 3 hr to remove all the unreacted carbon species to yield SiC nanowires.

Characterizations: Transmission electron microscopy (TEM) of all the synthesized samples was performed on a FEI Morgagni microscope, operating at an acceleration voltage of 80 keV. High resolution TEM (HRTEM) images were obtained on a JEOL 2010F high-resolution transmission electron microscope equipped with an energy dispersive x-ray spectroscopy (EDX) accessory, operating at an accelerating voltage of 200 keV. Scanning electron microscopy (SEM) was performed with a Phillips XL30 FEG microscope equipped with an energy dispersive x-ray spectroscopy (EDX) accessory. X-ray Diffraction (XRD) was performed at a Philips X'pert diffractometer for powder and thin film diffraction.

Electrical measurements of SiC nanorods: An aqueous suspension of SiC nanorods (0.01 mg/mL) was drop-cast (10 μL x 10) onto a ceramic chip (dense aluminum oxide) with interdigitated platinum electrodes (4 mil spacing, from Electronics Design Center, Case Western Reserve University). Two high temperature wires with Nextel fiber insulation (maximum working temperature 980 °C, from Omega Engineering, Inc.) were employed as the conducting wires and were connected to a Keithley SourceMeter 2400. The connection between the chip and high temperature wires was established by wrapping a thin platinum wire around the end of the high temperature wire; the other end of the thin wire was kept in touch with electrodes on the chip and fixed with platinum-silver paint (maximum working temperature around 600 °C, ESL ElectroScience). The maximum working temperature of such device was up to 600 °C, and could reach up to 1000 °C with a proper platinum paint. Utilizing this system, we managed to measure the I-V characteristics of the SiC nanorod devices from room temperature to 600 °C in hundred degree intervals in Ar environment (bias voltage from -20V to 20V); each temperature was maintained for half an hour before each electrical test. Field-effect transistors (FETs) were also fabricated from the SiC nanorods. Specifically, a small amount of SiC nanorods (0.5 μL of 0.01

mg/mL aqueous suspension) were deposited on top of a Si chip with an oxide layer (300 nm) and interdigitated gold electrodes (from MEMS and Nanotechnology Exchange). The back gate of the chip was attached to a conducting alumina tape through silver paint, and the whole device was taped on top of a glass slide. The FET characteristics of the SiC nanorod device were measured with a Probe Station Micromanipulator that was connected to Keithley SourceMeter 2400, and the temperature of the device was controlled by a hotplate, from room temperature to 400 °C in air.

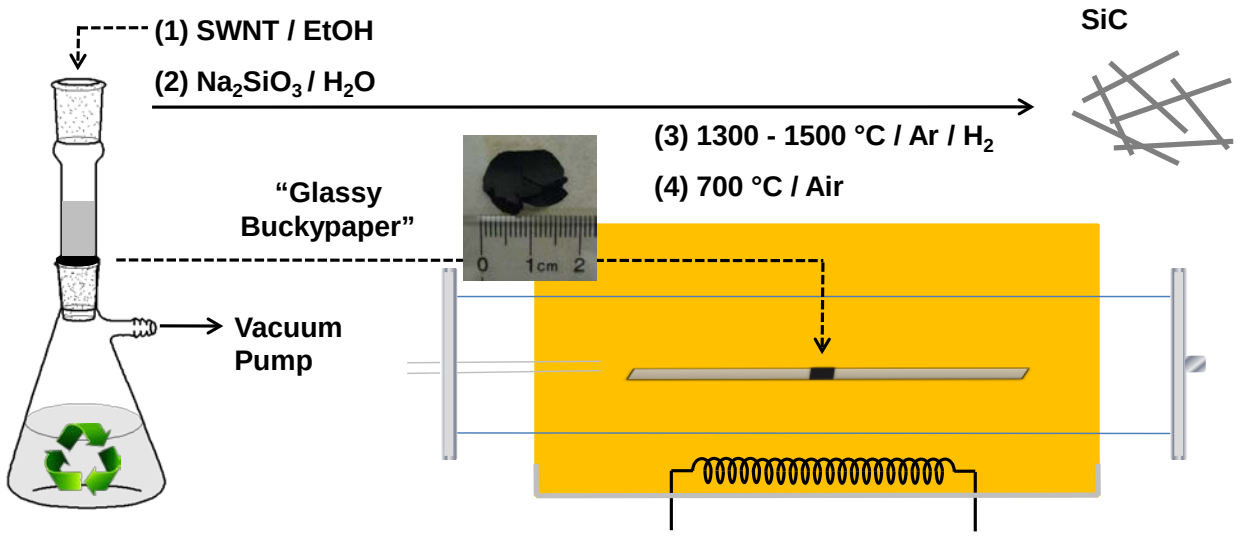

Figure 5-1. Schematic illustration of the synthesis of one-dimensional (1-D) SiC nanostructures from a SWNT-silicate composite ("glassy buckypaper"). "glassy buckypaper" was prepared using vacuum filtration of (1) SWNTs suspension in ethanol, followed by (2) continuous washing with sodium silicate solution. The "glassy buckypaper" was further (3) calcinated at high temperature in a tube furnace and after (4) burning unreacted carbon in air affording SiC 1-D nanostructures.

5.4 RESULTS AND DISCUSSION

5.4.1 Synthesis of SiC Nanorods from the "Glassy Buckypaper"

Figure 5-2a shows a typical SEM image of the as-prepared SWNT-silicate composite film ("glassy buckypaper"). At relatively low temperatures (1000 - 1200 °C), no reaction between SWNTs and silicate took place and no SiC was formed. However, an aggregation of silicate on the side walls of SWNTs was observed and nanoparticles composed of SiO_2 were formed (Figure 5-2b and c). When the calcination temperature was raised to 1300 °C, SWNTs started to react with silicate and the phase of SiC could be gradually observed, as indicated by the XRD and EDX results (Figure 5-3a and b). After 10 hr of calcination, the reaction was close to completion and the residue carbon could be removed by an additional calcination in air which was confirmed by XRD (Figure 5-3a). As also revealed by the XRD spectra, the resulting SiC samples had a well-developed cubic (3C-SiC) crystal structure (also known as β-SiC). Multiple orientations were indicated by the XRD peaks, where the [111] orientation appeared to be predominant. The reaction rate could be further increased by employing a higher calcination temperature. For example, the complete reaction between SWNTs and silicate could be accomplished within 1 hr at 1500 °C. However, at this temperature, a lower yield of SiC materials (15 wt% vs. 20 wt% for 10 hr at 1300 °C) was observed. This was probably due to the volatilization and decomposition of SiC at such high temperatures in a reducing environment.[260] Figure 5-3c depicts a typical SEM image of the products after calcination of the "glassy buckypaper" at 1300 °C for 10 hr. The resulting SiC products were in the form of nanorods with approximately 100 nm in diameter

and 1 μm in length, which is also shown in the TEM images (shown in details in the following sections). These characterization results provide evidence that a solid state reaction was enabled to form 1-D SiC nanomaterials through the employment of "glassy buckypaper" with SWNTs as the C source and silicate as the non-toxic Si source. This reaction is different from the generally reported vapor-liquid-solid (VLS) or vapor-solid (VS) mechanism. As a result, material processing was simplified during the synthesis and this "glassy buckypaper" approach shows promising potentials for large scale production.

As a control experiment, multi-walled carbon nanotubes (MWNTs) were also used to form a MWNT-silicate composite to obtain the SiC products. Although MWNTs have elemental composition similar to SWNTs and possess 1-D morphology, SiC nanorods were not formed (data not shown here). The specific requirement of SWNTs in this synthetic approach was probably due to two reasons. First, SWNTs could easily form a rigid solid film containing the adsorbed silicate (i.e., the "glassy buckypaper"). This could be a key factor to maintain the structural integrity of the nanotubes during the high temperature solid state reaction to produce SiC. As for MWNTs, large particles were formed instead of a continuous film after they were washed with silicate solutions under the same conditions. Second, as the Si source in this approach was from the silicate adsorbed on the surface of carbon nanotubes, the corresponding C source was only necessary from the surface C atoms. While SWNTs were entirely composed of surface atoms, inner tubes of MWNTs provided and excess of C during the reaction. The extra C could go through a variety of possible reactions, and these subsequent reactions were overall not beneficial for maintaining the existing 1-D morphology.

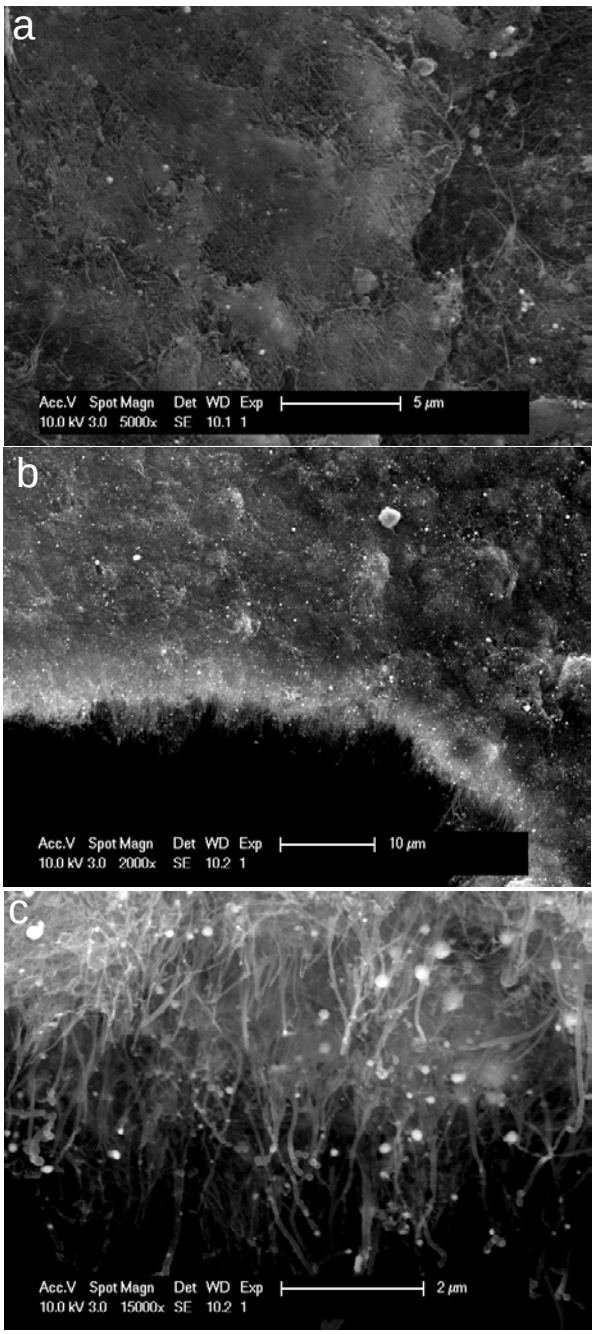

Figure 5-2. Morphology of the "glassy buckypaper". (a) Scanning Electron Microscopy (SEM) image of a SWNT-silicate film ("glassy buckypaper"). (b, c) SEM images after low temperature calcination (1200 °C) of "glassy buckypaper".

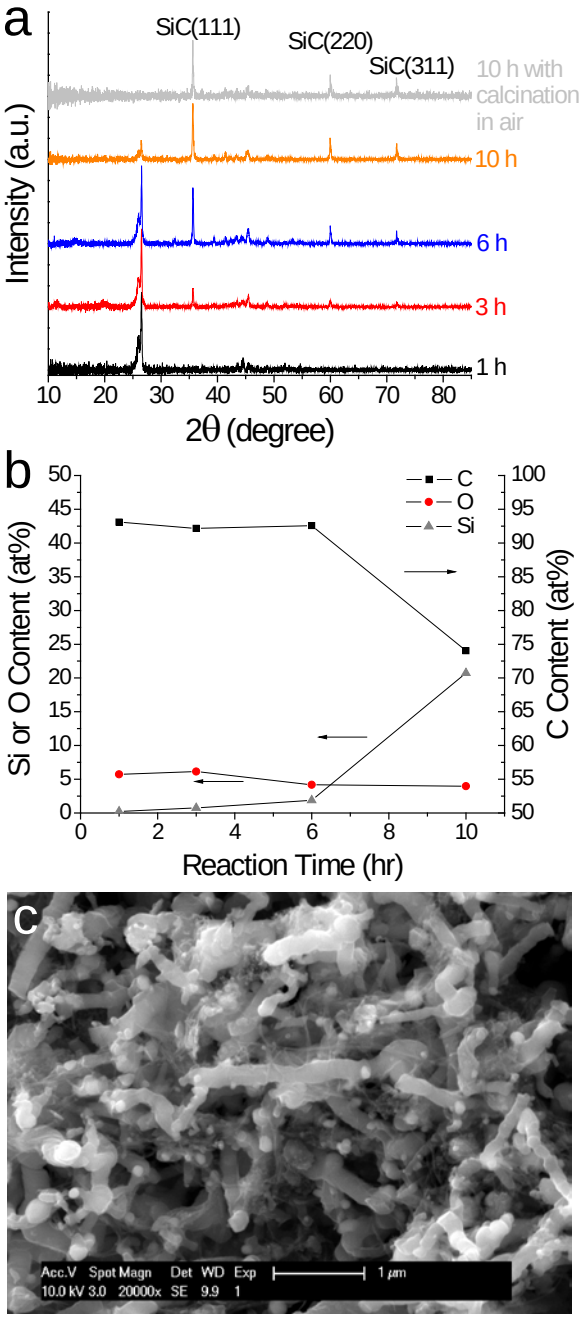

Figure 5-3. Synthesis of SiC nanorods from the "glassy buckypaper". (a) X-ray diffraction (XRD) patterns of the SiC products after different times of calcination at 1300 °C and after calcination at 700 °C in air. The intensity of graphitic peaks (around 27°) gradually decreased with the increasing reaction time, while intensities of the SiC peaks increased. After calcination in air, the C residues were completely removed, resulting in pure SiC product. (b) Energy dispersive x-ray spectroscopy (EDX) analysis of the SiC products after different times of calcination at 1300 °C. (c) Scanning Electron Microscopy (SEM) image of the SiC nanorods.

5.4.2 Characterization of the SiC Nanorods

The morphology and crystal structure of SiC nanorods synthesized from the "glassy buckypaper" were further studied in detail. Figure 5-4a shows the TEM image of a typical SiC nanorod, and electron diffraction patterns of the selected area of this nanorod (top dashed rectangular part in Figure 5-4a) are demonstrated in Figure 5-4b. The selected area electron diffraction (SAED) patterns indicated that the SiC nanorod was single crystalline, with a well-developed 3C-SiC crystal structure.[261] This was further confirmed by the High-Resolution TEM (HR-TEM) imaging of the same nanorod (Figure 5-4c), where the interfringe distance of the lattice was determined to be 0.25 nm, in agreement with (111) lattice spacing of the 3C-SiC. The corresponding fast Fourier transformed (FFT) diffraction patterns are also demonstrated as the inset of Figure 5-4c. It could be noticed that the FFT patterns revealed the same structural information as the SAED patterns, and they were thus employed in the following structural analysis. The detailed crystal structures of the SiC nanorod were consistent with the conclusion obtained from the bulk XRD results (Figure 5-3a). Furthermore, EDX analysis of the single SiC nanorod indicated that it contained C and Si elements with an atomic ratio that was close to 1:1, as shown in Figure 5-4d.

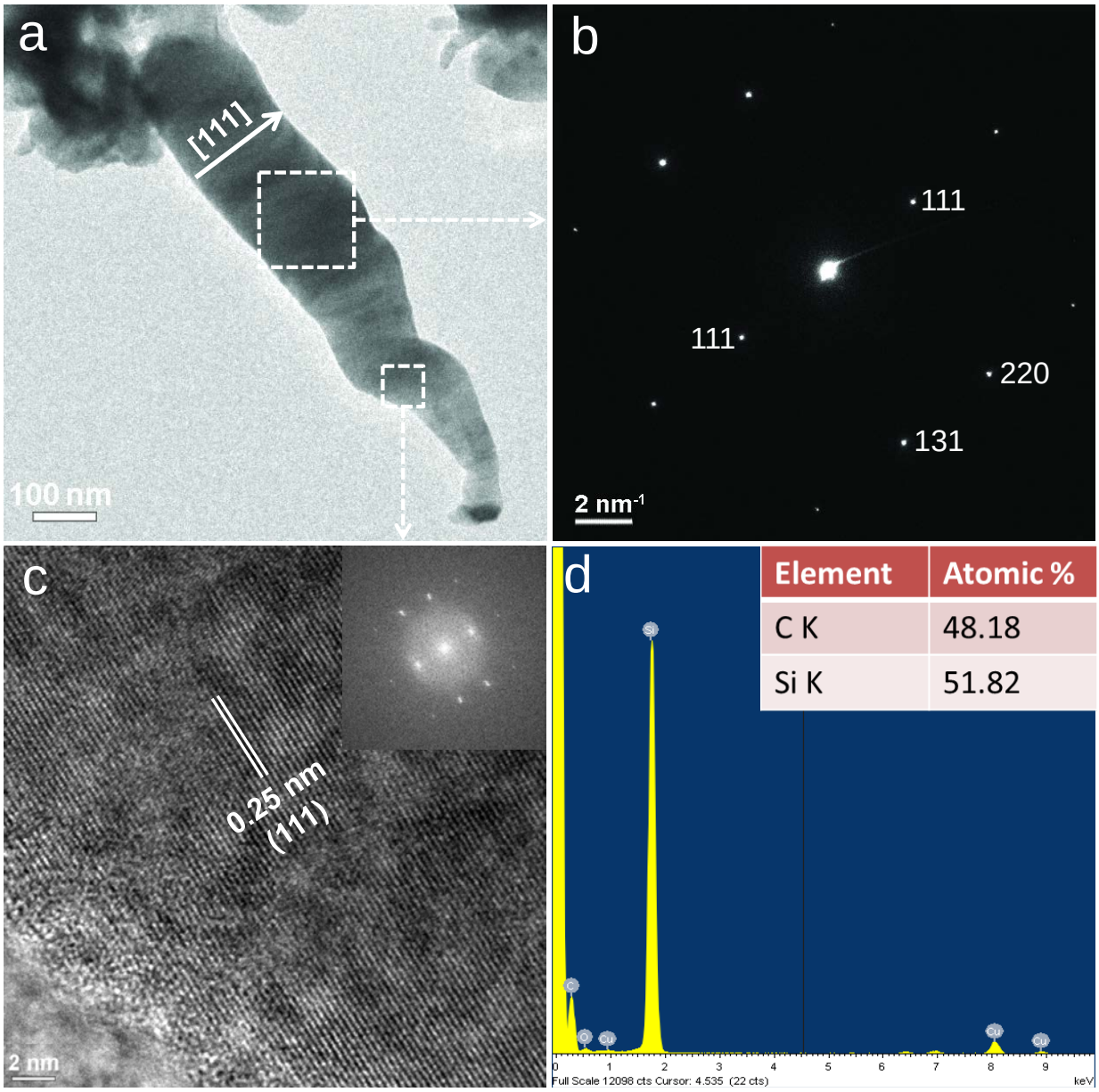

Figure 5-4. Crystal structure of a typical SiC nanorod. (a) Transmission Electron Microscopy (TEM) image of a typical SiC nanorod. (b) Selected area electron diffraction (SAED) patterns corresponding to the dashed area in (a), showing a single crystalline structure same as β-SiC. (c) High-Resolution TEM (HR-TEM) image of the selected (dashed) area of SiC nanorod in (a). The lattice spacing is 0.25 nm, in accordance with the (111) surface lattice of β-SiC. Inset depicts the Fast Fourier Transform (FFT) diffraction patterns of the image. (d) Energy dispersive x-ray spectra (EDX) of the SiC nanorod. Inset depicts the C and Si atomic ratio within the nanorod.

While most SiC nanorods synthesized from "glassy buckypaper" exhibited similar crystal structures to that in Figure 5-4a, other morphology was present. Figure 5-5a demonstrates a relatively long nanorod with disordered or defective structure that could be attributed to the stacking faults (SF), as shown in Figure 5-5b.[262-263] Long streaks resulting from the stacking faults[263] were further observed in the FFT diffraction patterns (Figure 5-5b inset). The end point of the nanorod appeared to be single crystalline, as shown in Figure 5-5c and d, which could probably serve as the starting point for the growth of the SF regions. The interface between two different regions is demonstrated in Figure 5-5d, where the transition from single crystalline to the highly disordered SF area occurred at a bend in the nanorod. It should be mentioned that such nanorods with high SF ratios were not commonly observed in the bulk nanorod sample, as also indicated by the lack of an SF diffraction peak[239, 263] in the bulk XRD result (Figure 5-3a). Another typical single crystalline 3C-SiC nanorod that was representative to the sample is demonstrated in Figure 5-5e and f.

The cubic (3C) crystal structure of SiC nanorods was similar to a variety of previously reported SiC nanowires.[239, 251-252] However, a [111] lattice orientation that was perpendicular to the longitudinal axes of the nanorods was observed in our sample, as illustrated in Figure 5-4a, Figure 5-5a and e, and was further confirmed by the lattice lines observed in HR-TEM image and corresponding SAED/FFT patterns. This orientation was different from the most reported structures of SiC nanowires, where the [111] direction was usually along the growth direction of the nanowires.[239, 251-252, 261-264] This unusual orientation was probably resulted from our unique synthetic approach from "glassy buckypaper", where formation and growth of SiC nanorods originated from pure solid state reactions.

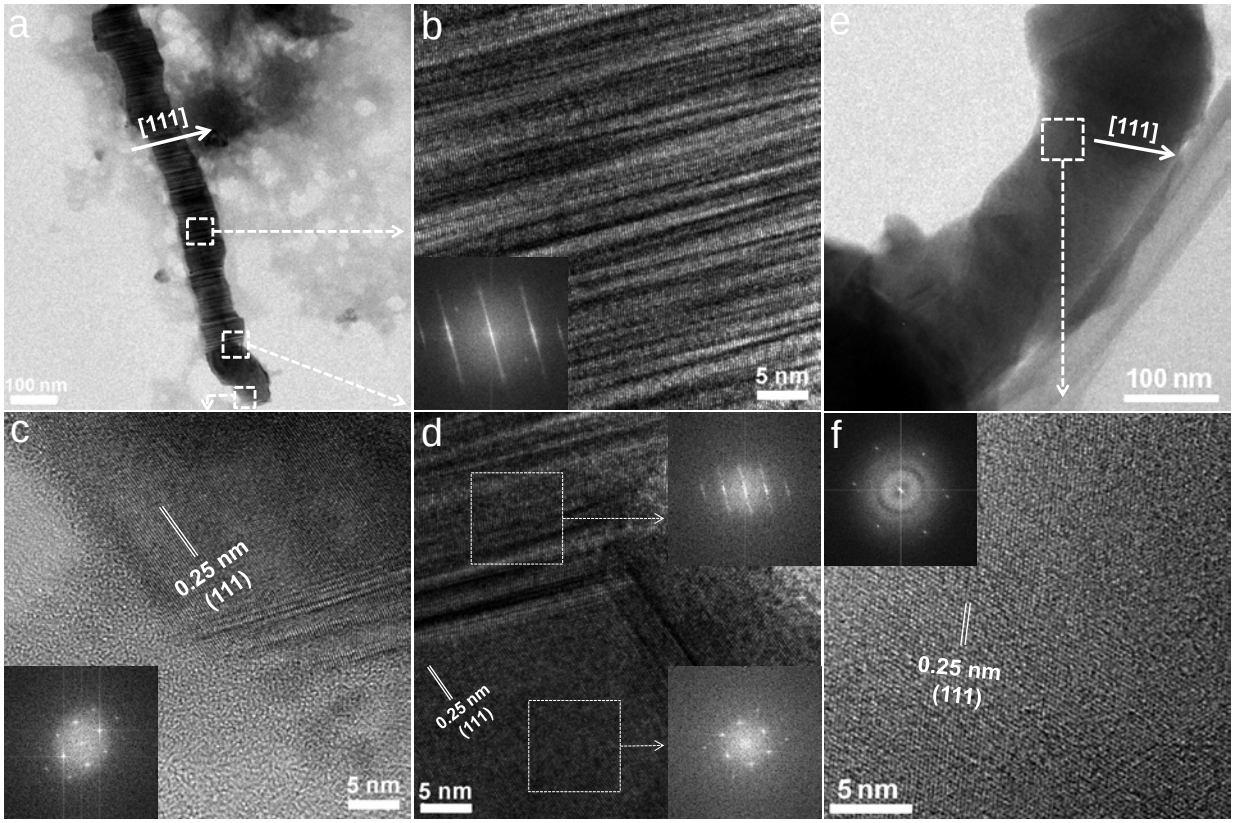

Figure 5-5. Structural analysis of different SiC nanorods. (a) TEM image of a long SiC nanorod with mostly stacking faults structure. (b, c, d) Corresponding HR-TEM images of the selected area of nanorod in (a). Insets depict the respective FFT diffraction patterns of each area. (e) TEM image of a short SiC nanorod with 3C-SiC structure. (f) HR-TEM image of the selected area in (e), inset depicts the FFT diffraction pattern of the image.

5.4.3 Synthesis of SiC Nanowires from the "Glassy Buckypaper".

Although the resulting SiC nanorods maintained the one-dimensional structure of SWNTs, the nanorods were shorter in length and larger in diameter, compared with the starting nanotube templates. Two possible reasons are proposed here to explain such a difference in the morphology. First, the SWNTs template existed as bundles in the network, with a diameter larger than the individual nanotube. Second, the aggregation of silicate precursors on the carbon nanotube started from a temperature (1200 °C, Figure 5-2c) lower than the reaction temperature (1300 °C) and could last during the long time of reaction (10 hr). It should also be noted that it took approximately 30 min for the furnace to heat to a temperature of 1200 °C or higher. Therefore, adsorbed silicate aggregated to form bigger particles along SWNTs before temperature became high enough for the formation of SiC. After the nanoparticles were formed and temperature reached 1300 °C, the reaction started from the interface between carbon nanotube bundles and silicate particles, with further material migration before the complete formation of SiC. As a result, shorter SiC nanorods with larger diameters were formed. In order to minimize silicate aggregation and obtain one-dimensional SiC nanostructures with higher length to diameter ratio (ideally to be similar to the starting carbon nanotubes), another fast calcination strategy was employed. In this alternative method, the furnace containing the SWNT-silicate composite film was heated to a temperature higher than 1300 °C (typically 1400 °C), and the heating was stopped immediately after the furnace reached the desired temperature. As shown in Figure 5-6 (method 2), the furnace temperature reached a peak value and then started to drop instantly. With this specific heating strategy, the "glassy buckypaper" experienced a much shorter period of heating, and the aggregation of the silicate was minimized. On the other hand,

the high temperature region that might cause the volatilization and decomposition of SiC products was also limited. The comparison of detailed temperature profiles between these two methods is demonstrated in Figure 5-6. Overall, compared with the former increasing and constant “step shaped” heating, this alternative “peak shaped” heating method was expected to give a better length to diameter ratio of the final SiC nanostructures.

As shown in Figure 5-7a, this fast heating approach indeed generated a SiC nanowire product with longer length (several micronmeters) and smaller diameters (10 - 50 nm). Due to the shorter reaction times, these as-prepared SiC nanowires appeared to be amorphous in crystallinity (Figure 5-7b). We further noticed that due to the short period of calcination, there is an aggregation of metal species in the material network, which resulted in some metal nanoparticle impurities in the final products (data not shown here). These metal residues probably originated from the catalysts that were used to produce the SWNTs, as different metal nanoparticles were generated from different carbon nanotube sources (Ni nanoparticles from arc discharge, Carbon Solutions, Inc. and Fe nanoparticles from HiPCO, Carbon Nanotechnologies Inc.). These nanoparticles were not observed in the SiC nanorods samples, probably due to the long calcination time in the hydrogen gas environment. Therefore, further calcination and chemical treatments were required in order to produce highly crystalline and pure SiC nanowires.

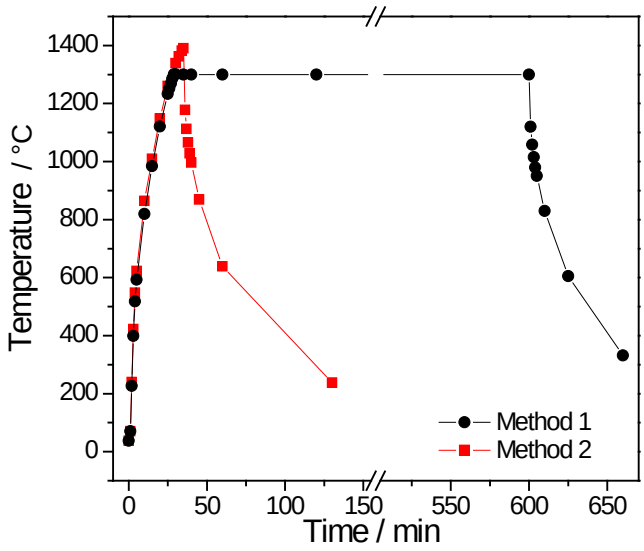

Figure 5-6. Temperature profiles of two different calcination approaches for the production of SiC nanostructures. Method 1 led to the formation of SiC nanorods whereas method 2 led to the formation of SiC nanowires.

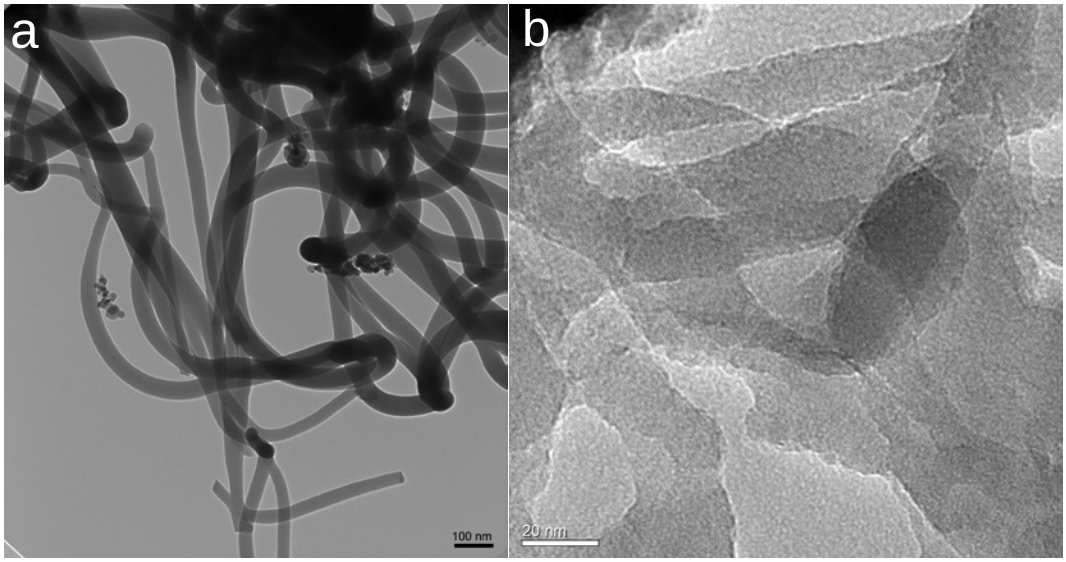

Figure 5-7. SiC nanowires synthesized from the "Glassy Buckypaper". (a) TEM and (b) HR-TEM images of SiC nanowires.

5.4.4 Growth Mechanisms of the SiC Nanostructures

As evidenced by the characterization results of “glassy buckypaper” before and after low temperature calcinations and final SiC products after the high temperature calcination, the mechanism for the formation of 1-D SiC nanostructures is summarized in Figure 5-8. A silicate containing layer was formed in the “glassy buckypaper”, as a result of the molecular adsorption on the sidewalls of SWNTs during the silicate washing of SWNTs network. This silicate coated SWNT architecture is an ideal structure that utilized the morphology of SWNTs as templates and created a maximum reaction interface for the production of SiC. Two processes occurred during the calcination of this “glassy buckypaper” network. At low temperature region (below 1200 °C), silicate coatings started to aggregate, while no reaction with SWNTs took place. When the temperature reached a relatively high value (above 1300 °C), SiC was gradually produced from the reaction between C and Si source. Since the reaction could only occur at the SWNT-silicate interface, the final morphology of the SiC product was therefore determined by the size of the Si containing particles. As a result of the competition between the silicate aggregation and C-Si reaction, control of the temperature profiles (most importantly, the rate of heating) could effectively alter the morphology of SiC nanostructures in this synthetic approach.

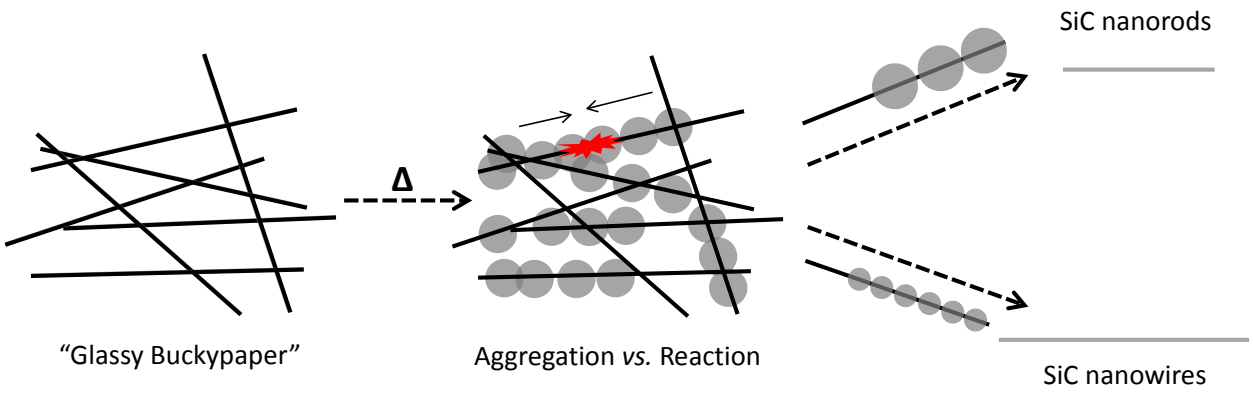

Figure 5-8. Proposed mechanism for the formation of one-dimensional (1-D) SiC nanostructures from "Glassy Buckypaper". During the high temperature calcination, the competition between silicate aggregation and C-Si reaction determines the final morphology of SiC nanostructures. Residual carbon is removed after calcination in air.

5.4.5 Electrical Properties of the SiC Nanorods

SiC based materials are particularly promising for applications in electrical devices that have to be operated in harsh conditions, such as high temperature, high pressure, and oxidizing environment. The one-dimensional morphology of the SiC nanorods or nanowires also made them an ideal candidate for the chemical sensing in extreme situations where carbon nanotubes or Si nanowires cannot be employed. Here we fabricated chemiresistive devices based on the one-dimensional SiC nanorods and tested their electrical properties at elevated temperatures, the device schematic is illustrated in Figure 5-9a. Such electrical devices could be potentially used for gas detection at high temperatures. As shown in Figure 5-9b and c, the conductivities of the SiC nanorod devices increased with the raising temperatures, however, the relationship between the device resistance and the temperature observed in this work differs from those reported for bulk SiC or SiC nanowires.[236-237] This result indicated that both charge carrier mobility and contact barriers play a role in the change of device performance with varying temperatures. It should also be noted that the average conductance of our SiC nanorods devices was five orders of magnitude lower than the reported conductance of single β-SiC nanowire devices.[236, 265] This could be rationalized by two possible reasons: i) the SiC nanorods prepared in this work were undoped, and ii) the devices were fabricated based on a film of numerous SiC nanorods. Compared with single SiC nanowire devices, a much longer charge carrier pathway and significant amount of nanorod-nanorod interconnections could both contribute to the much higher resistivity. The increased resistance was not a critical problem for the use of SiC nanorods in chemiresistor that has less strict requirement on device conductance, on the other hand, the abundance of rod to rod interconnections in the device could actually be beneficial for the

potential sensor applications, as it has been reported that resistance determined by interface between 1-D nanostructures could provide additional chemical sensitivity.[14] Moreover, a field-effect transistor was fabricated from the SiC nanorods, where the back gate of the device was attached through silver paint to a conducting alumina tape, and all the electrodes (source, drain and gate) were connected to a probe station micromanipulator (results are not shown here). Due to the low density of nanorods in the device, low source-drain current was observed during the scanning of gate voltage at room temperature. At elevated temperatures, p-type semiconductor characteristics were observed. This result was unexpected since no dopant was intentionally added during the synthetic process; moreover, unintentional doping usually resulted in n-type SiC nanostructures.[252, 266] The possible source of p-type unintentional doping could be either Al[267] from the alumina container or other metal residues[268] left from SWNTs, and further investigation will be required for clarification. Overall, the electrical measurements of SiC nanorods demonstrated their potential to be incorporated into electrical devices with promising future applications in high temperature chemiresistor for chemical sensing in the specific environment.

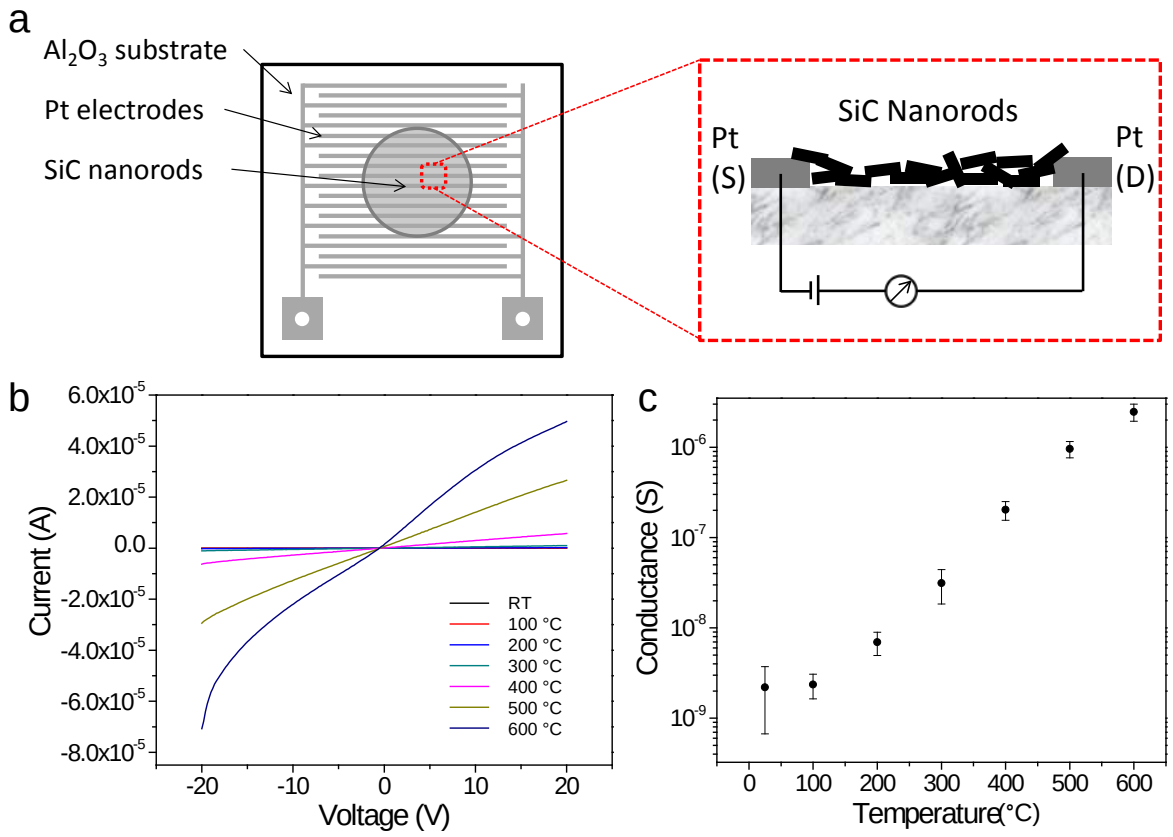

Figure 5-9. Electrical characterization of the SiC nanorods devices. (a) Schematic representation of the electrical device fabricated from SiC nanorods. (b) I-V characteristics of the SiC nanorods devices at different temperatures from room temperature to 600 °C. (c) Conductance of the SiC nanorods at different temperatures.

5.5 CONCLUSION

In summary, a simple, scalable and low-cost solid state approach was developed for the synthesis of one-dimensional SiC nanostructures using carbon nanotubes as templates. Compared with generally used vapor-liquid-solid (VLS) and vapor-solid (VS) reactions based on Si containing vapors, the employment of “glassy buckypaper” and the following solid state reaction will significantly simplify the material processing and reduce the production cost. EDX and XRD characterizations confirmed the successful synthesis of SiC material using this approach. SEM and TEM characterizations demonstrated their one-dimensional morphology and detailed crystal structure and orientation. The final morphology of the SiC nanomaterials was determined by programming of the heating procedure, and two 1-D nanostructures, SiC nanorods and SiC nanowires were obtained from two different heating profiles. Such correlation inspired a future direction where extreme heating profiles (such as fast laser heating) could be utilized for the fabrication of 1-D SiC nanomaterials from the “glassy buckypaper” with better controlled morphology. Although the quality of the SiC nanowires was limited due to the catalyst residues in the commercial SWNT samples, it could be expected that this approach will provide an innovative and practical way of producing SiC nanowires with similar quality to previously developed methods, once industrial production of SWNTs or “buckypaper” achieved better quality and purity. In addition, electrical devices that could operate at elevated temperatures were successfully fabricated from SiC nanorods, with future applications in chemical sensing at harsh conditions. This approach could therefore be viewed as an effective methodology to convert the hybrid nanomaterials (“Glassy Buckypaper” in this case) to the alternative high performance

nanomaterials that overcome certain limitations of the graphitic carbon nanomaterials for specific applications.

6.0 SUMMARY AND FUTURE OUTLOOK

My PhD research has focused on materials chemistry, physical chemistry and analytical chemistry of hybrid nanomaterials based on single-walled carbon nanotubes and graphene. I investigated their hybridization with polyaniline, gold, and titanium dioxide nanostructures, which are representative for a wide range of functional materials. The employed synthetic methods such as noncovalent modification, nanoscale coatings, in-plane diffusion/assembly, and nanowelding process provided a toolbox for the construction of complex nanoscale architectures. My strong interests in the exploration of novel hybrid nanomaterials, in addition to the fundamental investigations, originated from the practical objectives of developing better chemical sensors. From both fundamental and practical aspects, promising results have been accomplished. Improved gas sensory tools have been successfully developed, which could find applications in industrial monitoring, personal safety, and the medical field, while better understandings have been obtained on the electronic coupling and interfacial processes in the hybrid systems.

My research experience on the carbon-based hybrid nanostructures is a part of the ongoing research trend that has already led to significant success in the field of hybrid materials. However, for such a hybrid system composed of at least two types of nanostructures as building blocks, challenges remain in the development of synthetic methodology that allows manipulation and engineering with high level of precision (ideally, with atomic precision). I hope that the

results demonstrated in this document could offer some direction and methodology to achieve this ultimate goal. The importance of hybrid interfaces has also been gradually recognized in many recent studies and should be specifically emphasized in the future development of hybrid systems. Besides the techniques that have been employed in this study, better characterization, design and fabrication of controlled interfaces could become the new frontier in this research area. The desire of improved chemical sensing technology will keep growing, as any revolutionary progress in this field will dramatically impact various branches of industry and change the ways people practice medicine. While the successful development of several advanced chemical sensors during my PhD studies has provided some good examples on how to optimize the existing sensing motifs and create novel sensing schemes, continuous progress on the organic, inorganic and materials chemistry will be required to achieve these goals and further expand the toolbox of molecular recognition strategies.

Appendix A

LIST OF ABBREVIATIONS

Table 1. List of abbreviations.

Abbreviation		Abbreviation	
CNMs	Carbon Nanomaterials	XPS	X-ray Photoelectron Spectroscopy
CNTs	Carbon Nanotubes	CMOS	Complementary Metal Oxide Semiconductor
SWNTs	Single-Walled Carbon Nanotubes	R	Resistance
MWNTs	Multi-Walled Carbon Nanotubes	G	Conductance
0-D	Zero-dimensional	FET	Field-effect Transistor
1-D	One-dimensional	μ	Charge Carrier Mobility
2-D	Two-dimensional	PAni	Polyaniline
CVD	Chemical Vapor Deposition	PAni NFs	PAni Nanofibers
UV−vis−NIR	Ultraviolet-Visible-Near-infrared	PSA	Pyrenesulfonic Acid

DOS	Density of States	TGA	Thermogravimetric Analysis
CB	Conduction Band	CV	Cyclic Voltammetry
VB	Valence Band	AuNWs	Gold Nanowires
GO	Graphene Oxide	AuNPs	Gold Nanoparticles
CP	Conducting/Conjugated Polymer	EDS	Energy Dispersive X-ray Spectroscopy
ALD	Atomic Layer Deposition	SPR	Surface Plasmon Resonance
MNPs	Metal Nanoparticles	CCG	Chemically Converted Graphene
TEM	Transmission Electron Microscopy	DFT	Density Functional Theory
HR-TEM	High Resolution-TEM	REL	Recommended Exposure Limit
AC-HRTEM	Aberration-corrected HR-TEM	S/N	Signal to Noise Ratio
AFM	Atomic Force Microscopy	ED	Electron Diffraction
STM	Scanning Tunneling Microscopy	FFT	Fast Fourier Transform
FTIR	Fourier Transform Infrared Spectroscopy	SAED	Selected Area Electron Diffraction
XRD	X-ray Diffraction		

BIBLIOGRAPHY

1. Yan, H.; Choe, H. S.; Nam, S.; Hu, Y.; Das, S.; Klemic, J. F.; Ellenbogen, J. C.; Lieber, C. M., Programmable nanowire circuits for nanoprocessors. *Nature* **2011,** *470*, 240-244.

2. Siegwart, D. J.; Whitehead, K. A.; Nuhn, L.; Sahay, G.; Cheng, H.; Jiang, S.; Ma, M.; Lytton-Jean, A.; Vegas, A.; Fenton, P.; Levins, C. G.; Love, K. T.; Lee, H.; Cortez, C.; Collins, S. P.; Li, Y. F.; Jang, J.; Querbes, W.; Zurenko, C.; Novobrantseva, T.; Langer, R.; Anderson, D. G., Combinatorial synthesis of chemically diverse core-shell nanoparticles for intracellular delivery. *Proc. Nat. Acad. Sci.* **2011,** *108*, 12996-13001.

3. Ambrogio, M. W.; Thomas, C. R.; Zhao, Y.-L.; Zink, J. I.; Stoddart, J. F., Mechanized Silica Nanoparticles: A New Frontier in Theranostic Nanomedicine. *Acc. Chem. Res.* **2011,** *44*, 903-913.

4. Sailor, M. J.; Park, J.-H., Hybrid Nanoparticles for Detection and Treatment of Cancer. *Adv. Mater.* **2012,** *24*, 3779-3802.

5. Joo, S. H.; Park, J. Y.; Tsung, C.-K.; Yamada, Y.; Yang, P.; Somorjai, G. A., Thermally stable Pt/mesoporous silica core-shell nanocatalysts for high-temperature reactions. *Nat. Mater.* **2009,** *8*, 126-131.

6. Yamada, Y.; Tsung, C.-K.; Huang, W.; Huo, Z.; Habas, S. E.; Soejima, T.; Aliaga, C. E.; Somorjai, G. A.; Yang, P., Nanocrystal bilayer for tandem catalysis. *Nat. Chem.* **2011,** *3*, 372-376.

7. Dang, X.; Yi, H.; Ham, M.-H.; Qi, J.; Yun, D. S.; Ladewski, R.; Strano, M. S.; Hammond, P. T.; Belcher, A. M., Virus-templated self-assembled single-walled carbon nanotubes for highly efficient electron collection in photovoltaic devices. *Nat. Nanotech.* **2011,** *6*, 377-384.

8. Kempa, T. J.; Cahoon, J. F.; Kim, S.-K.; Day, R. W.; Bell, D. C.; Park, H.-G.; Lieber, C. M., Coaxial multishell nanowires with high-quality electronic interfaces and tunable optical cavities for ultrathin photovoltaics. *Proc. Nat. Acad. Sci.* **2012,** *109*, 1407-1412.

9. Reddy, A. L. M.; Gowda, S. R.; Shaijumon, M. M.; Ajayan, P. M., Hybrid Nanostructures for Energy Storage Applications. *Adv. Mater.* **2012,** *24*, 5045-5064.

10. Wang, H.; Dai, H., Strongly coupled inorganic-nano-carbon hybrid materials for energy storage. *Chem. Soc. Rev.* **2013,** *42*, 3088-3113.

11. Rosi, N. L.; Mirkin, C. A., Nanostructures in Biodiagnostics. *Chem. Rev.* **2005,** *105*, 1547-1562.

12. Kauffman, D. R.; Shade, C. M.; Uh, H.; Petoud, S.; Star, A., Decorated carbon nanotubes with unique oxygen sensitivity. *Nat. Chem.* **2009,** *1*, 500-506.

13. Ding, M.; Tang, Y.; Gou, P.; Reber, M. J.; Star, A., Chemical Sensing with Polyaniline Coated Single-Walled Carbon Nanotubes. *Adv. Mater.* **2011,** *23*, 536-540.

14. Ding, M.; Sorescu, D. C.; Kotchey, G. P.; Star, A., Welding of Gold Nanoparticles on Graphitic Templates for Chemical Sensing. *J. Am. Chem. Soc.* **2012,** *134*, 3472-3479.

15. Wight, A. P.; Davis, M. E., Design and Preparation of Organic−Inorganic Hybrid Catalysts. *Chem. Rev.* **2002,** *102*, 3589-3614.

16. Ortiz, R. P.; Facchetti, A.; Marks, T. J., High-k Organic, Inorganic, and Hybrid Dielectrics for Low-Voltage Organic Field-Effect Transistors. *Chem. Rev.* **2009,** *110*, 205-239.

17. Agranovich, V. M.; Gartstein, Y. N.; Litinskaya, M., Hybrid Resonant Organic–Inorganic Nanostructures for Optoelectronic Applications. *Chem. Rev.* **2011,** *111*, 5179-5214.

18. Pulickel M. Ajayan, L. S. S., Paul V. Braun, Nanocomposite Science and Technology. In *Nanocomposite Science and Technology*, Wiley-VCH Verlag GmbH & Co. KGaA: 2004.

19. Meldrum, A.; Haglund, R. F., Jr.; Boatner, L. A.; White, C. W., Nanocomposite Materials Formed by Ion Implantation. *Adv. Mater.* **2001,** *13*, 1431-1444.

20. Pyun, J.; Matyjaszewski, K., Synthesis of Nanocomposite Organic/Inorganic Hybrid Materials Using Controlled/"Living" Radical Polymerization. *Chem. Mater.* **2001,** *13*, 3436-3448.

21. Balazs, A. C.; Emrick, T.; Russell, T. P., Nanoparticle Polymer Composites: Where Two Small Worlds Meet. *Science* **2006,** *314*, 1107-1110.

22. Pandey, G.; Thostenson, E. T., Carbon Nanotube-Based Multifunctional Polymer Nanocomposites. *Polym. Rev.* **2012,** *52*, 355-416.

23. Ionescu, E.; Kleebe, H.-J.; Riedel, R., Silicon-containing polymer-derived ceramic nanocomposites (PDC-NCs): preparative approaches and properties. *Chem. Soc. Rev.* **2012,** *41*, 5032-5052.

24. Lee, J. E.; Lee, N.; Kim, T.; Kim, J.; Hyeon, T., Multifunctional Mesoporous Silica Nanocomposite Nanoparticles for Theranostic Applications. *Acc. Chem. Res.* **2011,** *44*, 893-902.

25. Leung, K. C.-F.; Xuan, S.; Zhu, X.; Wang, D.; Chak, C.-P.; Lee, S.-F.; Ho, W. K. W.; Chung, B. C. T., Gold and iron oxide hybrid nanocomposite materials. *Chem. Soc. Rev.* **2012,** *41*, 1911-1928.

26. Shi, J., On the Synergetic Catalytic Effect in Heterogeneous Nanocomposite Catalysts. *Chem. Rev.* **2012,** *113*, 2139-2181.

27. Lauhon, L. J.; Gudiksen, M. S.; Lieber, C. M., Semiconductor nanowire heterostructures. *Phil. Trans. R. Soc. Lond. A* **2004,** *362*, 1247-1260.

28. Lauhon, L. J.; Gudiksen, M. S.; Wang, D.; Lieber, C. M., Epitaxial core-shell and core-multishell nanowire heterostructures. *Nature* **2002,** *420*, 57-61.

29. Selinsky, R. S.; Ding, Q.; Faber, M. S.; Wright, J. C.; Jin, S., Quantum dot nanoscale heterostructures for solar energy conversion. *Chem. Soc. Rev.* **2013,** *42*, 2963-2985.

30. Ding, M.; Tang, Y.; Star, A., Understanding Interfaces in Metal–Graphitic Hybrid Nanostructures. *J. Phys. Chem. Lett.* **2012,** *4*, 147-160.

31. Moniruzzaman, M.; Winey, K. I., Polymer Nanocomposites Containing Carbon Nanotubes. *Macromolecules* **2006,** *39*, 5194-5205.

32. Coleman, J. N.; Khan, U.; Gun'ko, Y. K., Mechanical Reinforcement of Polymers Using Carbon Nanotubes. *Adv. Mater.* **2006,** *18*, 689-706.

33. Hasan, T.; Sun, Z.; Wang, F.; Bonaccorso, F.; Tan, P. H.; Rozhin, A. G.; Ferrari, A. C., Nanotube–Polymer Composites for Ultrafast Photonics. *Adv. Mater.* **2009,** *21*, 3874-3899.

34. Kroto, H. W.; Heath, J. R.; O'Brien, S. C.; Curl, R. F.; Smalley, R. E., C60: Buckminsterfullerene. *Nature* **1985,** *318*, 162-163.

35. Iijima, S., Helical microtubules of graphitic carbon. *Nature* **1991,** *354*, 56-58.

36. Iijima, S.; Ichihashi, T., Single-shell carbon nanotubes of 1-nm diameter. *Nature* **1993,** *363*, 603-605.

37. Bethune, D. S.; Klang, C. H.; de Vries, M. S.; Gorman, G.; Savoy, R.; Vazquez, J.; Beyers, R., Cobalt-catalysed growth of carbon nanotubes with single-atomic-layer walls. *Nature* **1993,** *363*, 605-607.

38. Novoselov, K. S.; Geim, A. K.; Morozov, S. V.; Jiang, D.; Zhang, Y.; Dubonos, S. V.; Grigorieva, I. V.; Firsov, A. A., Electric Field Effect in Atomically Thin Carbon Films. *Science* **2004,** *306*, 666-669.

39. Novoselov, K. S.; Jiang, D.; Schedin, F.; Booth, T. J.; Khotkevich, V. V.; Morozov, S. V.; Geim, A. K., Two-dimensional atomic crystals. *Proc. Nat. Acad. Sci.* **2005,** *102*, 10451-10453.

40. Geim, A. K.; Novoselov, K. S., The rise of graphene. *Nat. Mater.* **2007,** *6*, 183-191.

41. Ajayan, P. M., Nanotubes from Carbon. *Chem. Rev.* **1999,** *99*, 1787-1800.

42. Hamada, N.; Sawada, S.-i.; Oshiyama, A., New one-dimensional conductors: Graphitic microtubules. *Phys. Rev. Lett.* **1992,** *68*, 1579-1581.

43. Odom, T. W.; Huang, J.-L.; Kim, P.; Lieber, C. M., Structure and Electronic Properties of Carbon Nanotubes. *J. Phys. Chem. B* **2000,** *104*, 2794-2809.

44. Kim, S. N.; Rusling, J. F.; Papadimitrakopoulos, F., Carbon Nanotubes for Electronic and Electrochemical Detection of Biomolecules. *Adv. Mater.* **2007,** *19*, 3214-3228.

45. Saito, R.; Dresselhaus, G.; Dresselhaus, M. S., Trigonal warping effect of carbon nanotubes. *Phys. Rev. B* **2000,** *61*, 2981-2990.

46. Saito, R.; Fujita, M.; Dresselhaus, G.; Dresselhaus, M. S., Electronic structure of chiral graphene tubules. *Appl. Phys. Lett.* **1992,** *60*, 2204.

47. Kauffman, D. R.; Star, A., Single-Walled Carbon-Nanotube Spectroscopic and Electronic Field-Effect Transistor Measurements: A Combined Approach. *Small* **2007,** *3*, 1324-1329.

48. Kataura, H.; Kumazawa, Y.; Maniwa, Y.; Umezu, I.; Suzuki, S.; Ohtsuka, Y.; Achiba, Y., Optical properties of single-wall carbon nanotubes. *Synth. Met.* **1999,** *103*, 2555-2558.

49. Wallace, P. R., The Band Theory of Graphite. *Phys. Rev.* **1947,** *71*, 622-634.

50. Slonczewski, J. C.; Weiss, P. R., Band Structure of Graphite. *Phys. Rev.* **1958,** *109*, 272-279.

51. Eizenberg, M.; Blakely, J. M., Carbon interaction with nickel surfaces: Monolayer formation and structural stability. *J. Chem. Phys.* **1979,** *71*, 3467-3477.

52. Xuekun, L.; Minfeng, Y.; Hui, H.; Rodney, S. R., Tailoring graphite with the goal of achieving single sheets. *Nanotechnology* **1999,** *10*, 269.

53. Berger, C.; Song, Z.; Li, T.; Li, X.; Ogbazghi, A. Y.; Feng, R.; Dai, Z.; Marchenkov, A. N.; Conrad, E. H.; First, P. N.; de Heer, W. A., Ultrathin Epitaxial Graphite: 2D Electron Gas Properties and a Route toward Graphene-based Nanoelectronics. *J. Phys. Chem. B* **2004,** *108*, 19912-19916.

54. Emtsev, K. V.; Bostwick, A.; Horn, K.; Jobst, J.; Kellogg, G. L.; Ley, L.; McChesney, J. L.; Ohta, T.; Reshanov, S. A.; Rohrl, J.; Rotenberg, E.; Schmid, A. K.; Waldmann, D.; Weber, H. B.; Seyller, T., Towards wafer-size graphene layers by atmospheric pressure graphitization of silicon carbide. *Nat. Mater.* **2009,** *8*, 203-207.

55. Seyller, T.; Bostwick, A.; Emtsev, K. V.; Horn, K.; Ley, L.; McChesney, J. L.; Ohta, T.; Riley, J. D.; Rotenberg, E.; Speck, F., Epitaxial graphene: a new material. *Phys. Status Solidi B* **2008,** *245*, 1436-1446.

56. Land, T. A.; Michely, T.; Behm, R. J.; Hemminger, J. C.; Comsa, G., STM investigation of single layer graphite structures produced on Pt(111) by hydrocarbon decomposition. *Surf. Sci.* **1992,** *264*, 261-270.

57. Kim, K. S.; Zhao, Y.; Jang, H.; Lee, S. Y.; Kim, J. M.; Kim, K. S.; Ahn, J.-H.; Kim, P.; Choi, J.-Y.; Hong, B. H., Large-scale pattern growth of graphene films for stretchable transparent electrodes. *Nature* **2009,** *457*, 706-710.

58. Li, X.; Cai, W.; An, J.; Kim, S.; Nah, J.; Yang, D.; Piner, R.; Velamakanni, A.; Jung, I.; Tutuc, E.; Banerjee, S. K.; Colombo, L.; Ruoff, R. S., Large-Area Synthesis of High-Quality and Uniform Graphene Films on Copper Foils. *Science* **2009,** *324*, 1312-1314.

59. Wei, D.; Wu, B.; Guo, Y.; Yu, G.; Liu, Y., Controllable Chemical Vapor Deposition Growth of Few Layer Graphene for Electronic Devices. *Acc. Chem. Res.* **2012,** *46*, 106-115.

60. Edwards, R. S.; Coleman, K. S., Graphene Film Growth on Polycrystalline Metals. *Acc. Chem. Res.* **2012,** *46*, 23-30.

61. Dreyer, D. R.; Park, S.; Bielawski, C. W.; Ruoff, R. S., The chemistry of graphene oxide. *Chem. Soc. Rev.* **2010,** *39*, 228-240.

62. Allen, M. J.; Tung, V. C.; Kaner, R. B., Honeycomb Carbon: A Review of Graphene. *Chem. Rev.* **2009,** *110*, 132-145.

63. Coleman, J. N., Liquid Exfoliation of Defect-Free Graphene. *Acc. Chem. Res.* **2012,** *46*, 14-22.

64. Kelly, K. F.; Billups, W. E., Synthesis of Soluble Graphite and Graphene. *Acc. Chem. Res.* **2012,** *46*, 4-13.

65. Avouris, P.; Chen, Z.; Perebeinos, V., Carbon-based electronics. *Nat. Nanotech.* **2007,** *2*, 605-615.

66. Young, A. F.; Kim, P., Electronic Transport in Graphene Heterostructures. *Annu. Rev. Cond. Mat. Phys.* **2011,** *2*, 101-120.

67. Bonaccorso, F.; Sun, Z.; Hasan, T.; Ferrari, A. C., Graphene photonics and optoelectronics. *Nat. Photon.* **2010,** *4*, 611-622.

68. Grigorenko, A. N.; Polini, M.; Novoselov, K. S., Graphene plasmonics. *Nat. Photon.* **2012,** *6*, 749-758.

69. Sarkar, S.; Bekyarova, E.; Haddon, R. C., Chemistry at the Dirac Point: Diels–Alder Reactivity of Graphene. *Acc. Chem. Res.* **2012,** *45*, 673-682.

70. Yan, L.; Zheng, Y. B.; Zhao, F.; Li, S.; Gao, X.; Xu, B.; Weiss, P. S.; Zhao, Y., Chemistry and physics of a single atomic layer: strategies and challenges for functionalization of graphene and graphene-based materials. *Chem. Soc. Rev.* **2012,** *41*, 97-114.

71. Bekyarova, E.; Sarkar, S.; Wang, F.; Itkis, M. E.; Kalinina, I.; Tian, X.; Haddon, R. C., Effect of Covalent Chemistry on the Electronic Structure and Properties of Carbon Nanotubes and Graphene. *Acc. Chem. Res.* **2012,** *46*, 65-76.

72. Paulus, G. L. C.; Wang, Q. H.; Strano, M. S., Covalent Electron Transfer Chemistry of Graphene with Diazonium Salts. *Acc. Chem. Res.* **2012,** *46*, 160-170.

73. Ajayan, P. M.; Stephan, O.; Colliex, C.; Trauth, D., Aligned Carbon Nanotube Arrays Formed by Cutting a Polymer Resin—Nanotube Composite. *Science* **1994,** *265*, 1212-1214.

74. Dai, L.; Mau, A. W. H., Controlled Synthesis and Modification of Carbon Nanotubes and C60: Carbon Nanostructures for Advanced Polymeric Composite Materials. *Adv. Mater.* **2001,** *13*, 899-913.

75. Tasis, D.; Tagmatarchis, N.; Bianco, A.; Prato, M., Chemistry of Carbon Nanotubes. *Chem. Rev.* **2006,** *106*, 1105-1136.

76. Star, A.; Han, T. R.; Joshi, V.; Gabriel, J. C. P.; Grüner, G., Nanoelectronic Carbon Dioxide Sensors. *Adv. Mater.* **2004,** *16*, 2049-2052.

77. Zhao, Y.-L.; Stoddart, J. F., Noncovalent Functionalization of Single-Walled Carbon Nanotubes. *Acc. Chem. Res.* **2009,** *42*, 1161-1171.

78. Downs, C.; Nugent, J.; Ajayan, P. M.; Duquette, D. J.; Santhanam, K. S. V., Efficient Polymerization of Aniline at Carbon Nanotube Electrodes. *Adv. Mater.* **1999,** *11*, 1028-1031.

79. Gao, M.; Huang, S.; Dai, L.; Wallace, G.; Gao, R.; Wang, Z., Aligned Coaxial Nanowires of Carbon Nanotubes Sheathed with Conducting Polymers. *Angew. Chem. Int. Ed.* **2000,** *39*, 3664-3667.

80. Cochet, M.; Maser, W. K.; Benito, A. M.; Callejas, M. A.; Martinez, M. T.; Benoit, J.-M.; Schreiber, J.; Chauvet, O., Synthesis of a new polyaniline/nanotube composite: "in situ" polymerisation and charge transfer through site-selective interaction. *Chem. Commun.* **2001,** *0*, 1450-1451.

81. Zhang, X.; Lü, Z.; Wen, M.; Liang, H.; Zhang, J.; Liu, Z., Single-Walled Carbon Nanotube-Based Coaxial Nanowires: Synthesis, Characterization, and Electrical Properties. *J. Phys. Chem. B* **2004,** *109*, 1101-1107.

82. Star, A.; Stoddart, J. F.; Steuerman, D.; Diehl, M.; Boukai, A.; Wong, E. W.; Yang, X.; Chung, S.-W.; Choi, H.; Heath, J. R., Preparation and Properties of Polymer-Wrapped Single-Walled Carbon Nanotubes. *Angew. Chem. Int. Ed.* **2001,** *40*, 1721-1725.

83. Steuerman, D. W.; Star, A.; Narizzano, R.; Choi, H.; Ries, R. S.; Nicolini, C.; Stoddart, J. F.; Heath, J. R., Interactions between Conjugated Polymers and Single-Walled Carbon Nanotubes. *J. Phys. Chem. B* **2002,** *106*, 3124-3130.

84. Star, A.; Liu, Y.; Grant, K.; Ridvan, L.; Stoddart, J. F.; Steuerman, D. W.; Diehl, M. R.; Boukai, A.; Heath, J. R., Noncovalent Side-Wall Functionalization of Single-Walled Carbon Nanotubes. *Macromolecules* **2003,** *36*, 553-560.

85. Huang, X.; Qi, X.; Boey, F.; Zhang, H., Graphene-based composites. *Chem. Soc. Rev.* **2012,** *41*, 666-686.

86. Planeix, J. M.; Coustel, N.; Coq, B.; Brotons, V.; Kumbhar, P. S.; Dutartre, R.; Geneste, P.; Bernier, P.; Ajayan, P. M., Application of Carbon Nanotubes as Supports in Heterogeneous Catalysis. *J. Am. Chem. Soc.* **1994,** *116*, 7935-7936.

87. Ebbesen, T. W.; Hiura, H.; Bisher, M. E.; Treacy, M. M. J.; Shreeve-Keyer, J. L.; Haushalter, R. C., Decoration of carbon nanotubes. *Adv. Mater.* **1996,** *8*, 155-157.

88. Wildgoose, G. G.; Banks, C. E.; Compton, R. G., Metal Nanoparticles and Related Materials Supported on Carbon Nanotubes: Methods and Applications. *Small* **2006,** *2*, 182-193.

89. Peng, X.; Chen, J.; Misewich, J. A.; Wong, S. S., Carbon nanotube-nanocrystal heterostructures. *Chem. Soc. Rev.* **2009,** *38*, 1076-1098.

90. Wu, B.; Kuang, Y.; Zhang, X.; Chen, J., Noble metal nanoparticles/carbon nanotubes nanohybrids: Synthesis and applications. *Nano Today* **2011,** *6*, 75-90.

91. Li, X.; Qin, Y.; Picraux, S. T.; Guo, Z.-X., Noncovalent assembly of carbon nanotube-inorganic hybrids. *J. Mater. Chem.* **2011,** *21*, 7527-7547.

92. Eder, D., Carbon Nanotube−Inorganic Hybrids. *Chem. Rev.* **2010,** *110*, 1348-1385.

93. Bai, S.; Shen, X., Graphene-inorganic nanocomposites. *RSC Adv.* **2012,** *2*, 64-98.

94. Kamat, P. V., Graphene-Based Nanoassemblies for Energy Conversion. *J. Phys. Chem. Lett.* **2011,** *2*, 242-251.

95. Liang, Y.; Li, Y.; Wang, H.; Dai, H., Strongly Coupled Inorganic/Nanocarbon Hybrid Materials for Advanced Electrocatalysis. *J. Am. Chem. Soc.* **2013,** *135*, 2013-2036.

96. Woan, K.; Pyrgiotakis, G.; Sigmund, W., Photocatalytic Carbon-Nanotube–TiO2 Composites. *Adv. Mater.* **2009,** *21*, 2233-2239.

97. Qu, Y.; Duan, X., Progress, challenge and perspective of heterogeneous photocatalysts. *Chem. Soc. Rev.* **2013,** *42*, 2568-2580.

98. Ding, M.; Sorescu, D. C.; Star, A., Photoinduced Charge Transfer and Acetone Sensitivity of Single-Walled Carbon Nanotube-Titanium Dioxide Hybrids. *J. Am. Chem. Soc.* **2013**.

99. Ebbesen, T. W.; Lezec, H. J.; Hiura, H.; Bennett, J. W.; Ghaemi, H. F.; Thio, T., Electrical conductivity of individual carbon nanotubes. *Nature* **1996,** *382*, 54-56.

100. Tans, S. J.; Verschueren, A. R. M.; Dekker, C., Room-temperature transistor based on a single carbon nanotube. *Nature* **1998,** *393*, 49-52.

101. Tans, S. J.; Devoret, M. H.; Dai, H.; Thess, A.; Smalley, R. E.; Geerligs, L. J.; Dekker, C., Individual single-wall carbon nanotubes as quantum wires. *Nature* **1997,** *386*, 474-477.

102. Fuhrer, M. S.; Nygård, J.; Shih, L.; Forero, M.; Yoon, Y.-G.; Mazzoni, M. S. C.; Choi, H. J.; Ihm, J.; Louie, S. G.; Zettl, A.; McEuen, P. L., Crossed Nanotube Junctions. *Science* **2000,** *288*, 494-497.

103. Avouris, P., Molecular Electronics with Carbon Nanotubes. *Acc. Chem. Res.* **2002,** *35*, 1026-1034.

104. Dai, H., Carbon Nanotubes: Synthesis, Integration, and Properties. *Acc. Chem. Res.* **2002,** *35*, 1035-1044.

105. Ouyang, M.; Huang, J.-L.; Lieber, C. M., Fundamental Electronic Properties and Applications of Single-Walled Carbon Nanotubes. *Acc. Chem. Res.* **2002,** *35*, 1018-1025.

106. Chen, R. J.; Franklin, N. R.; Kong, J.; Cao, J.; Tombler, T. W.; Zhang, Y.; Dai, H., Molecular photodesorption from single-walled carbon nanotubes. *Appl. Phys. Lett.* **2001,** *79*, 2258-2260.

107. Kong, J.; Franklin, N. R.; Zhou, C.; Chapline, M. G.; Peng, S.; Cho, K.; Dai, H., Nanotube Molecular Wires as Chemical Sensors. *Science* **2000,** *287*, 622-625.

108. Hersam, M. C., Progress towards monodisperse single-walled carbon nanotubes. *Nat. Nanotech.* **2008,** *3*, 387-394.

109. Zhang, H.; Wu, B.; Hu, W.; Liu, Y., Separation and/or selective enrichment of single-walled carbon nanotubes based on their electronic properties. *Chem. Soc. Rev.* **2011,** *40*, 1324-1336.

110. Park, H.; Afzali, A.; Han, S.-J.; Tulevski, G. S.; Franklin, A. D.; Tersoff, J.; Hannon, J. B.; Haensch, W., High-density integration of carbon nanotubes via chemical self-assembly. *Nat. Nanotech.* **2012,** *7*, 787-791.

111. Snow, E. S.; Novak, J. P.; Campbell, P. M.; Park, D., Random networks of carbon nanotubes as an electronic material. *Appl. Phys. Lett.* **2003,** *82*, 2145-2147.

112. Snow, E. S.; Novak, J. P.; Lay, M. D.; Perkins, F. K., 1/f noise in single-walled carbon nanotube devices. *Appl. Phys. Lett.* **2004,** *85*, 4172-4174.

113. Wang, C.; Takei, K.; Takahashi, T.; Javey, A., Carbon nanotube electronics - moving forward. *Chem. Soc. Rev.* **2013,** *42*, 2592-2609.

114. Snow, E. S.; Perkins, F. K.; Robinson, J. A., Chemical vapor detection using single-walled carbon nanotubes. *Chem. Soc. Rev.* **2006,** *35*, 790-798.

115. Allen, B. L.; Kichambare, P. D.; Star, A., Carbon Nanotube Field-Effect-Transistor-Based Biosensors. *Adv. Mater.* **2007,** *19*, 1439-1451.

116. Zhou, C.; Kong, J.; Dai, H., Electrical measurements of individual semiconducting single-walled carbon nanotubes of various diameters. *Appl. Phys. Lett.* **2000,** *76*, 1597-1599.

117. Heinze, S.; Tersoff, J.; Martel, R.; Derycke, V.; Appenzeller, J.; Avouris, P., Carbon Nanotubes as Schottky Barrier Transistors. *Phys. Rev. Lett.* **2002,** *89*, 106801.

118. Suzuki, S.; Bower, C.; Watanabe, Y.; Zhou, O., Work functions and valence band states of pristine and Cs-intercalated single-walled carbon nanotube bundles. *Appl. Phys. Lett.* **2000,** *76*, 4007-4009.

119. Zhao, J.; Han, J.; Lu, J. P., Work functions of pristine and alkali-metal intercalated carbon nanotubes and bundles. *Phys. Rev. B* **2002,** *65*, 193401.

120. Potje-Kamloth, K., Semiconductor Junction Gas Sensors. *Chem. Rev.* **2008,** *108*, 367-399.

121. Kauffman, D. R.; Star, A., Chemically Induced Potential Barriers at the Carbon Nanotube−Metal Nanoparticle Interface. *Nano Lett.* **2007,** *7*, 1863-1868.

122. Martel, R.; Schmidt, T.; Shea, H. R.; Hertel, T.; Avouris, P., Single- and multi-wall carbon nanotube field-effect transistors. *Appl. Phys. Lett.* **1998,** *73*, 2447-2449.

123. Castro Neto, A. H.; Guinea, F.; Peres, N. M. R.; Novoselov, K. S.; Geim, A. K., The electronic properties of graphene. *Rev. Mod. Phys.* **2009,** *81*, 109-162.

124. Schwierz, F., Graphene transistors. *Nat. Nanotech.* **2010,** *5*, 487-496.

125. Han, M. Y.; Özyilmaz, B.; Zhang, Y.; Kim, P., Energy Band-Gap Engineering of Graphene Nanoribbons. *Phys. Rev. Lett.* **2007,** *98*, 206805.

126. Li, X.; Wang, X.; Zhang, L.; Lee, S.; Dai, H., Chemically Derived, Ultrasmooth Graphene Nanoribbon Semiconductors. *Science* **2008,** *319*, 1229-1232.

127. Bai, J.; Zhong, X.; Jiang, S.; Huang, Y.; Duan, X., Graphene nanomesh. *Nat. Nanotech.* **2010,** *5*, 190-194.

128. Vedala, H.; Sorescu, D. C.; Kotchey, G. P.; Star, A., Chemical Sensitivity of Graphene Edges Decorated with Metal Nanoparticles. *Nano Lett.* **2011,** *11*, 2342-2347.

129. Ting, Z.; Syed, M.; Nosang, V. M.; Marc, A. D., Recent progress in carbon nanotube-based gas sensors. *Nanotechnology* **2008,** *19*, 332001.

130. Kauffman, D. R.; Star, A., Carbon Nanotube Gas and Vapor Sensors. *Angew. Chem. Int. Ed.* **2008,** *47*, 6550-6570.

131. Collins, P. G.; Bradley, K.; Ishigami, M.; Zettl, A., Extreme Oxygen Sensitivity of Electronic Properties of Carbon Nanotubes. *Science* **2000,** *287*, 1801-1804.

132. Jariwala, D.; Sangwan, V. K.; Lauhon, L. J.; Marks, T. J.; Hersam, M. C., Carbon nanomaterials for electronics, optoelectronics, photovoltaics, and sensing. *Chem. Soc. Rev.* **2013,** *42*, 2824-2860.

133. Schedin, F.; Geim, A. K.; Morozov, S. V.; Hill, E. W.; Blake, P.; Katsnelson, M. I.; Novoselov, K. S., Detection of individual gas molecules adsorbed on graphene. *Nat. Mater.* **2007,** *6*, 652-655.

134. Kauffman, D. R.; Star, A., Graphene versus carbon nanotubes for chemical sensor and fuel cell applications. *Analyst* **2010,** *135*, 2790-2797.

135. He, Q.; Wu, S.; Yin, Z.; Zhang, H., Graphene-based electronic sensors. *Chem. Sci.* **2012,** *3*, 1764-1772.

136. Kolmakov, A.; Moskovits, M., CHEMICAL SENSING AND CATALYSIS BY ONE-DIMENSIONAL METAL-OXIDE NANOSTRUCTURES. *Annu. Rev. Mater. Res.* **2004,** *34*, 151-180.

137. Johnson, J. L.; Behnam, A.; Pearton, S. J.; Ural, A., Hydrogen Sensing Using Pd-Functionalized Multi-Layer Graphene Nanoribbon Networks. *Adv. Mater.* **2010,** *22*, 4877-4880.

138. Ding, M.; Star, A., Synthesis and Morphology Control of Carbon Nanotube/Polyaniline Composite for Chemical Sensing. *MRS Proceedings* **2012,** *1408*.

139. McQuade, D. T.; Pullen, A. E.; Swager, T. M., Conjugated Polymer-Based Chemical Sensors. *Chem. Rev.* **2000,** *100*, 2537-2574.

140. Huang, J.; Virji, S.; Weiller, B. H.; Kaner, R. B., Polyaniline Nanofibers: Facile Synthesis and Chemical Sensors. *J. Am. Chem. Soc.* **2002,** *125*, 314-315.

141. Virji, S.; Huang, J.; Kaner, R. B.; Weiller, B. H., Polyaniline Nanofiber Gas Sensors: Examination of Response Mechanisms. *Nano Lett.* **2004,** *4*, 491-496.

142. Tran, H. D.; Li, D.; Kaner, R. B., One-Dimensional Conducting Polymer Nanostructures: Bulk Synthesis and Applications. *Adv. Mater.* **2009,** *21*, 1487-1499.

143. He, L.; Jia, Y.; Meng, F.; Li, M.; Liu, J., Gas sensors for ammonia detection based on polyaniline-coated multi-wall carbon nanotubes. *Mat. Sci. Eng. B* **2009,** *163*, 76-81.

144. Ben-Valid, S.; Dumortier, H.; Decossas, M.; Sfez, R.; Meneghetti, M.; Bianco, A.; Yitzchaik, S., Polyaniline-coated single-walled carbon nanotubes: synthesis, characterization and impact on primary immune cells. *J. Mater. Chem.* **2010,** *20*, 2408-2417.

145. Liao, Y.; Zhang, C.; Zhang, Y.; Strong, V.; Tang, J.; Li, X.-G.; Kalantar-zadeh, K.; Hoek, E. M. V.; Wang, K. L.; Kaner, R. B., Carbon Nanotube/Polyaniline Composite Nanofibers: Facile Synthesis and Chemosensors. *Nano Lett.* **2011,** *11*, 954-959.

146. Zhang, T.; Nix, M. B.; Yoo, B.-Y.; Deshusses, M. A.; Myung, N. V., Electrochemically Functionalized Single-Walled Carbon Nanotube Gas Sensor. *Electroanalysis* **2006,** *18*, 1153-1158.

147. Liu, J.; Rinzler, A. G.; Dai, H.; Hafner, J. H.; Bradley, R. K.; Boul, P. J.; Lu, A.; Iverson, T.; Shelimov, K.; Huffman, C. B.; Rodriguez-Macias, F.; Shon, Y.-S.; Lee, T. R.; Colbert, D. T.; Smalley, R. E., Fullerene Pipes. *Science* **1998,** *280*, 1253-1256.

148. Simmons, T. J.; Bult, J.; Hashim, D. P.; Linhardt, R. J.; Ajayan, P. M., Noncovalent Functionalization as an Alternative to Oxidative Acid Treatment of Single Wall Carbon Nanotubes with Applications for Polymer Composites. *ACS Nano* **2009,** *3*, 865-870.

149. Sahoo, N. G.; Jung, Y. C.; So, H. H.; Cho, J. W., Polypyrrole coated carbon nanotubes: Synthesis, characterization, and enhanced electrical properties. *Synth. Met.* **2007,** *157*, 374-379.

150. Robinson, J. A.; Snow, E. S.; Bădescu, Ş. C.; Reinecke, T. L.; Perkins, F. K., Role of Defects in Single-Walled Carbon Nanotube Chemical Sensors. *Nano Lett.* **2006,** *6*, 1747-1751.

151. Klinke, C.; Chen, J.; Afzali, A.; Avouris, P., Charge Transfer Induced Polarity Switching in Carbon Nanotube Transistors. *Nano Lett.* **2005,** *5*, 555-558.

152. Virji, S.; Fowler, J. D.; Baker, C. O.; Huang, J.; Kaner, R. B.; Weiller, B. H., Polyaniline Nanofiber Composites with Metal Salts: Chemical Sensors for Hydrogen Sulfide. *Small* **2005,** *1*, 624-627.

153. Shanmugam, S.; Gedanken, A., Electrochemical properties of bamboo-shaped multiwalled carbon nanotubes generated by solid state pyrolysis. *Electrochem. Commun.* **2006,** *8*, 1099-1105.

154. Wang, Y. G.; Li, H. Q.; Xia, Y. Y., Ordered Whiskerlike Polyaniline Grown on the Surface of Mesoporous Carbon and Its Electrochemical Capacitance Performance. *Adv. Mater.* **2006,** *18*, 2619-2623.

155. Zhang, K.; Zhang, L. L.; Zhao, X. S.; Wu, J., Graphene/Polyaniline Nanofiber Composites as Supercapacitor Electrodes. *Chem. Mater.* **2010,** *22*, 1392-1401.

156. Zheng, M.; Diner, B. A., Solution Redox Chemistry of Carbon Nanotubes. *J. Am. Chem. Soc.* **2004,** *126*, 15490-15494.

157. Bekyarova, E.; Kalinina, I.; Itkis, M. E.; Beer, L.; Cabrera, N.; Haddon, R. C., Mechanism of Ammonia Detection by Chemically Functionalized Single-Walled Carbon Nanotubes: In Situ Electrical and Optical Study of Gas Analyte Detection. *J. Am. Chem. Soc.* **2007,** *129*, 10700-10706.

158. Redl, F. X.; Cho, K. S.; Murray, C. B.; O'Brien, S., Three-dimensional binary superlattices of magnetic nanocrystals and semiconductor quantum dots. *Nature* **2003,** *423*, 968-971.

159. Lu, W.; Lieber, C. M., Nanoelectronics from the bottom up. *Nat. Mater.* **2007,** *6*, 841-850.

160. Mann, S., Self-assembly and transformation of hybrid nano-objects and nanostructures under equilibrium and non-equilibrium conditions. *Nat. Mater.* **2009,** *8*, 781-792.

161. Wang, C.; Hu, Y.; Lieber, C. M.; Sun, S., Ultrathin Au Nanowires and Their Transport Properties. *J. Am. Chem. Soc.* **2008,** *130*, 8902-8903.

162. Xiang, C.; Kim, J. Y.; Penner, R. M., Reconnectable Sub-5 nm Nanogaps in Ultralong Gold Nanowires. *Nano Lett.* **2009,** *9*, 2133-2138.

163. Zhang, X.; Sun, B.; Hodgkiss, J. M.; Friend, R. H., Tunable Ultrafast Optical Switching via Waveguided Gold Nanowires. *Adv. Mater.* **2008,** *20*, 4455-4459.

164. Zhang, X.; Li, D.; Bourgeois, L.; Wang, H.; Webley, P. A., Direct Electrodeposition of Porous Gold Nanowire Arrays for Biosensing Applications. *ChemPhysChem* **2009,** *10*, 436-441.

165. Ofir, Y.; Samanta, B.; Rotello, V. M., Polymer and biopolymer mediated self-assembly of gold nanoparticles. *Chem. Soc. Rev.* **2008,** *37*, 1814-1825.

166. Chen, C.-L.; Rosi, N. L., Peptide-Based Methods for the Preparation of Nanostructured Inorganic Materials. *Angew. Chem. Int. Ed.* **2010,** *49*, 1924-1942.

167. Halder, A.; Ravishankar, N., Ultrafine Single-Crystalline Gold Nanowire Arrays by Oriented Attachment. *Adv. Mater.* **2007,** *19*, 1854-1858.

168. Kundu, P.; Halder, A.; Viswanath, B.; Kundu, D.; Ramanath, G.; Ravishankar, N., Nanoscale Heterostructures with Molecular-Scale Single-Crystal Metal Wires. *J. Am. Chem. Soc.* **2009,** *132*, 20-21.

169. Feng, H.; Yang, Y.; You, Y.; Li, G.; Guo, J.; Yu, T.; Shen, Z.; Wu, T.; Xing, B., Simple and rapid synthesis of ultrathin gold nanowires, their self-assembly and application in surface-enhanced Raman scattering. *Chem. Commun.* **2009,** *0*, 1984-1986.

170. Tang, Z.; Kotov, N. A.; Giersig, M., Spontaneous Organization of Single CdTe Nanoparticles into Luminescent Nanowires. *Science* **2002,** *297*, 237-240.

171. Koh, W.-k.; Bartnik, A. C.; Wise, F. W.; Murray, C. B., Synthesis of Monodisperse PbSe Nanorods: A Case for Oriented Attachment. *J. Am. Chem. Soc.* **2010,** *132*, 3909-3913.

172. Kim, S. J.; Jang, D.-J., Laser-induced nanowelding of gold nanoparticles. *Appl. Phys. Lett.* **2005,** *86*, 033112-3.

173. Peng, Y.; Cullis, T.; Inkson, B., Bottom-up Nanoconstruction by the Welding of Individual Metallic Nanoobjects Using Nanoscale Solder. *Nano Lett.* **2009,** *9*, 91-96.

174. Lu, Y.; Huang, J. Y.; Wang, C.; Sun, S.; Lou, J., Cold welding of ultrathin gold nanowires. *Nat. Nanotech.* **2010,** *5*, 218-224.

175. Huang, Y.; Chiang, C.-Y.; Lee, S. K.; Gao, Y.; Hu, E. L.; Yoreo, J. D.; Belcher, A. M., Programmable Assembly of Nanoarchitectures Using Genetically Engineered Viruses. *Nano Lett.* **2005,** *5*, 1429-1434.

176. McNerney, J. J.; Buseck, P. R.; Hanson, R. C., Mercury Detection by Means of Thin Gold Films. *Science* **1972,** *178*, 611-612.

177. Yoo, K. S.; Sorensen, I. W.; Glaunsinger, W. S., Adhesion, surface morphology, and gas sensing characteristics of thin-gold-film chemical sensors. *J. Vac. Sci. Technol. A* **1994,** *12*, 192-198.

178. Geng, J.; Thomas, M. D. R.; Shephard, D. S.; Johnson, B. F. G., Suppressed electron hopping in a Au nanoparticle/H2S system: development towards a H2S nanosensor. *Chem. Commun.* **2005,** *0*, 1895-1897.

179. Mubeen, S.; Zhang, T.; Chartuprayoon, N.; Rheem, Y.; Mulchandani, A.; Myung, N. V.; Deshusses, M. A., Sensitive Detection of H2S Using Gold Nanoparticle Decorated Single-Walled Carbon Nanotubes. *Anal. Chem.* **2009,** *82*, 250-257.

180. Si, Y.; Samulski, E. T., Synthesis of Water Soluble Graphene. *Nano Lett.* **2008,** *8*, 1679-1682.

181. Kovtyukhova, N. I.; Ollivier, P. J.; Martin, B. R.; Mallouk, T. E.; Chizhik, S. A.; Buzaneva, E. V.; Gorchinskiy, A. D., Layer-by-Layer Assembly of Ultrathin Composite

Films from Micron-Sized Graphite Oxide Sheets and Polycations. *Chem. Mater.* **1999,** *11*, 771-778.

182. Wu, Y.; Yang, P., Melting and Welding Semiconductor Nanowires in Nanotubes. *Adv. Mater.* **2001,** *13*, 520-523.

183. Sainsbury, T.; Stolarczyk, J.; Fitzmaurice, D., An Experimental and Theoretical Study of the Self-Assembly of Gold Nanoparticles at the Surface of Functionalized Multiwalled Carbon Nanotubes. *J. Phys. Chem. B* **2005,** *109*, 16310-16325.

184. Rance, G. A.; Marsh, D. H.; Bourne, S. J.; Reade, T. J.; Khlobystov, A. N., van der Waals Interactions between Nanotubes and Nanoparticles for Controlled Assembly of Composite Nanostructures. *ACS Nano* **2010,** *4*, 4920-4928.

185. Diamanti, S.; Elsen, A.; Naik, R.; Vaia, R., Relative Functionality of Buffer and Peptide in Gold Nanoparticle Formation. *J. Phys. Chem. C* **2009,** *113*, 9993-9997.

186. Heinz, H.; Farmer, B. L.; Pandey, R. B.; Slocik, J. M.; Patnaik, S. S.; Pachter, R.; Naik, R. R., Nature of Molecular Interactions of Peptides with Gold, Palladium, and Pd−Au Bimetal Surfaces in Aqueous Solution. *J. Am. Chem. Soc.* **2009,** *131*, 9704-9714.

187. Sato, M.; Kaieda, T.; Ohmukai, K.; Kawazumi, H.; Ogawa, T., Surface Density of Pyrenesulfonic Acid at the Air-Water Interface as Determined by Laser Two-Photon Ionization: Effect of pH and Salt. *Analyt. Sci.* **1998,** *14*, 855-856.

188. Zelent, B.; Vanderkooi, J. M.; Coleman, R. G.; Gryczynski, I.; Gryczynski, Z., Protonation of Excited State Pyrene-1-Carboxylate by Phosphate and Organic Acids in Aqueous Solution Studied by Fluorescence Spectroscopy. *Biophys. J.* **2006,** *91*, 3864-3871.

189. Ferguson, G. S.; Chaudhury, M. K.; Sigal, G. B.; Whitesides, G. M., Contact Adhesion of Thin Gold Films on Elastomeric Supports: Cold Welding Under Ambient Conditions. *Science* **1991,** *253*, 776-778.

190. Kauffman, D. R.; Sorescu, D. C.; Schofield, D. P.; Allen, B. L.; Jordan, K. D.; Star, A., Understanding the Sensor Response of Metal-Decorated Carbon Nanotubes. *Nano Lett.* **2010,** *10*, 958-963.

191. Suarez, F. L.; Furne, J. K.; Springfield, J.; Levitt, M. D., Morning Breath Odor: Influence of Treatments on Sulfur Gases. *J. Dent. Res.* **2000,** *79*, 1773-1777.

192. Tangerman, A.; Winkel, E. G., Extra-oral halitosis: an overview. *J. Breath Res.* **2010,** *4*, 017003.

193. Mubeen, S.; Lim, J.-H.; Srirangarajan, A.; Mulchandani, A.; Deshusses, M. A.; Myung, N. V., Gas Sensing Mechanism of Gold Nanoparticles Decorated Single-Walled Carbon Nanotubes. *Electroanalysis* **2011,** *23*, 2687-2692.

194. Jain, P.; Huang, X.; El-Sayed, I.; El-Sayed, M., Review of Some Interesting Surface Plasmon Resonance-enhanced Properties of Noble Metal Nanoparticles and Their Applications to Biosystems. *Plasmonics* **2007,** *2*, 107-118.

195. Lustemberg, P. G.; Vericat, C.; Benitez, G. A.; Vela, M. E.; Tognalli, N.; Fainstein, A.; Martiarena, M. L.; Salvarezza, R. C., Spontaneously Formed Sulfur Adlayers on Gold in Electrolyte Solutions: Adsorbed Sulfur or Gold Sulfide? *J. Phys. Chem. C* **2008,** *112*, 11394-11402.

196. Heller, I.; Janssens, A. M.; Mannik, J.; Minot, E. D.; Lemay, S. G.; Dekker, C., Identifying the Mechanism of Biosensing with Carbon Nanotube Transistors. *Nano Lett.* **2007,** *8*, 591-595.

197. Woan, K.; Pyrgiotakis, G.; Sigmund, W., Photocatalytic carbon-nanotube-TiO_2 composites. *Adv. Mater.* **2009,** *21*, 2233-2239.

198. Kongkanand, A.; Martínez Domínguez, R.; Kamat, P. V., Single wall carbon nanotube scaffolds for photoelectrochemical solar cells. capture and transport of photogenerated electrons. *Nano Lett.* **2007,** *7*, 676-680.

199. Yao, Y.; Li, G.; Ciston, S.; Lueptow, R. M.; Gray, K. A., Photoreactive TiO_2/carbon nanotube composites: synthesis and reactivity. *Environ. Sci. Technol.* **2008,** *42*, 4952-4957.

200. Hsu, C.-Y.; Lien, D.-H.; Lu, S.-Y.; Chen, C.-Y.; Kang, C.-F.; Chueh, Y.-L.; Hsu, W.-K.; He, J.-H., Supersensitive, ultrafast, and broad-band light-harvesting scheme employing carbon nanotube/TiO_2 core–shell nanowire geometry. *ACS Nano* **2012,** *6*, 6687-6692.

201. Cargnello, M.; Grzelczak, M.; Rodríguez-González, B.; Syrgiannis, Z.; Bakhmutsky, K.; La Parola, V.; Liz-Marzán, L. M.; Gorte, R. J.; Prato, M.; Fornasiero, P., Multiwalled carbon nanotubes drive the activity of metal@oxide core–shell catalysts in modular nanocomposites. *J. Am. Chem. Soc.* **2012,** *134*, 11760-11766.

202. Law, M.; Greene, L. E.; Johnson, J. C.; Saykally, R.; Yang, P., Nanowire dye-sensitized solar cells. *Nat. Mater.* **2005,** *4*, 455-459.

203. Hochbaum, A. I.; Yang, P., Semiconductor nanowires for energy conversion. *Chem. Rev.* **2009,** *110*, 527-546.

204. Hoang, S.; Guo, S.; Hahn, N. T.; Bard, A. J.; Mullins, C. B., Visible light driven photoelectrochemical water oxidation on nitrogen-modified TiO_2 nanowires. *Nano Lett.* **2011,** *12*, 26-32.

205. Hu, A.; Liu, S.; Lin, W., Immobilization of chiral catalysts on magnetite nanoparticles for highly enantioselective asymmetric hydrogenation of aromatic ketones. *RSC Advances* **2012,** *2*, 2576-2580.

206. Hoang, S.; Berglund, S. P.; Hahn, N. T.; Bard, A. J.; Mullins, C. B., Enhancing visible light photo-oxidation of water with TiO_2 nanowire arrays via cotreatment with H_2 and NH_3: synergistic effects between Ti^{3+} and N. *J. Am. Chem. Soc.* **2012,** *134*, 3659-3662.

207. Feng, X.; Zhu, K.; Frank, A. J.; Grimes, C. A.; Mallouk, T. E., Rapid charge transport in dye-sensitized solar cells made from vertically aligned single-crystal rutile TiO_2 nanowires. *Angew. Chem. Int. Ed.* **2012,** *51*, 2727-30.

208. Hwang, Y. J.; Boukai, A.; Yang, P., High density n-Si/n-TiO_2 core/shell nanowire arrays with enhanced photoactivity. *Nano Lett.* **2008,** *9*, 410-415.

209. Xu, C.; Wu, J.; Desai, U. V.; Gao, D., High-efficiency solid-state dye-sensitized solar cells based on TiO_2-coated ZnO nanowire arrays. *Nano Lett.* **2012,** *12*, 2420-2424.

210. D'Souza, F.; Chitta, R.; Sandanayaka, A. S. D.; Subbaiyan, N. K.; D'Souza, L.; Araki, Y.; Ito, O., Supramolecular Carbon Nanotube-Fullerene Donor−Acceptor Hybrids for Photoinduced Electron Transfer. *J. Am. Chem. Soc.* **2007,** *129*, 15865-15871.

211. Ehli, C.; Oelsner, C.; Guldi, D. M.; Mateo-Alonso, A.; Prato, M.; Schmidt, C.; Backes, C.; Hauke, F.; Hirsch, A., Manipulating single-wall carbon nanotubes by chemical doping and charge transfer with perylene dyes. *Nat. Chem.* **2009,** *1*, 243-249.

212. Oelsner, C.; Herrero, M. A.; Ehli, C.; Prato, M.; Guldi, D. M., Charge Transfer Events in Semiconducting Single-Wall Carbon Nanotubes. *J. Am. Chem. Soc.* **2011,** *133*, 18696-18706.

213. Oelsner, C.; Schmidt, C.; Hauke, F.; Prato, M.; Hirsch, A.; Guldi, D. M., Interfacing Strong Electron Acceptors with Single Wall Carbon Nanotubes. *J. Am. Chem. Soc.* **2011,** *133*, 4580-4586.

214. Ding, M.; Tang, Y.; Gou, P.; Reber, M. J.; Star, A., Chemical sensing with polyaniline coated single-walled carbon nanotubes. *Adv. Mater.* **2011,** *23*, 536-540.

215. Hu, L.; Zhao, Y. L.; Ryu, K.; Zhou, C.; Stoddart, J. F.; Grüner, G., Light-induced charge transfer in pyrene/CdSe-SWNT hybrids. *Adv. Mater.* **2008,** *20*, 939-946.

216. Liu, S.; Li, J.; Shen, Q.; Cao, Y.; Guo, X.; Zhang, G.; Feng, C.; Zhang, J.; Liu, Z.; Steigerwald, M. L.; Xu, D.; Nuckolls, C., Mirror-image photoswitching of individual single-walled carbon nanotube transistors coated with titanium dioxide. *Angew. Chem. Int. Ed.* **2009,** *48*, 4759-4762.

217. Laffel, L., Ketone bodies: a review of physiology, pathophysiology and application of monitoring to diabetes. *Diabetes Metab Res Rev* **1999,** *15*, 412-426.

218. Cao, W.; Duan, Y., Breath Analysis: Potential for Clinical Diagnosis and Exposure Assessment. *Clin. Chem.* **2006,** *52*, 800-811.

219. Itkis, M. E.; Perea, D. E.; Niyogi, S.; Rickard, S. M.; Hamon, M. A.; Hu, H.; Zhao, B.; Haddon, R. C., Purity evaluation of as-prepared single-walled carbon nanotube soot by use of solution-phase Near-IR spectroscopy. *Nano Lett.* **2003,** *3*, 309-314.

220. Snow, E. S.; Perkins, F. K., Capacitance and conductance of single-walled carbon nanotubes in the presence of chemical vapors. *Nano Lett.* **2005,** *5*, 2414-2417.

221. Thompson, T. L.; Yates, J. T., Surface science studies of the photoactivation of TiO_2 new photochemical processes. *Chem. Rev.* **2006,** *106*, 4428-4453.

222. Bahnemann, D. W.; Hilgendorff, M.; Memming, R., Charge carrier dynamics at TiO_2 particles: reactivity of free and trapped holes. *J. Phys. Chem. B* **1997,** *101*, 4265-4275.

223. Thompson, T. L.; Yates, J. T., Surface Science Studies of the Photoactivation of TiO2New Photochemical Processes. *Chem. Rev.* **2006,** *106*, 4428-4453.

224. Snow, E. S.; Perkins, F. K.; Houser, E. J.; Badescu, S. C.; Reinecke, T. L., Chemical detection with a single-walled carbon nanotube capacitor. *Science* **2005,** *307*, 1942-1945.

225. Robinson, J. T.; Perkins, F. K.; Snow, E. S.; Wei, Z.; Sheehan, P. E., Reduced graphene oxide molecular sensors. *Nano Lett.* **2008,** *8*, 3137-3140.

226. Chakrapani, N.; Zhang, Y. M.; Nayak, S. K.; Moore, J. A.; Carroll, D. L.; Choi, Y. Y.; Ajayan, P. M., Chemisorption of acetone on carbon nanotubes. *J. Phys. Chem. B* **2003,** *107*, 9308-9311.

227. Collins, P. G., Extreme oxygen sensitivity of electronic properties of carbon nanotubes. *Science* **2000,** *287*, 1801-1804.

228. Chen, G.; Paronyan, T. M.; Pigos, E. M.; Harutyunyan, A. R., Enhanced gas sensing in pristine carbon nanotubes under continuous ultraviolet light illumination. *Sci. Rep.* **2012,** *2*, 343.

229. Guirado-López, R. A.; Sánchez, M.; Rincón, M. E., Interaction of acetone molecules with carbon-nanotube-supported TiO_2 nanoparticles: possible applications as room temperature molecular sensitive coatings. *J. Phys. Chem. C* **2006,** *111*, 57-65.

230. Kharitonov, S. A.; Barnes, P. J., Biomarkers of some pulmonary diseases in exhaled breath. *Biomarkers* **2002,** *7*, 1-32.

231. Wang, C.; Sahay, P., Breath Analysis Using Laser Spectroscopic Techniques: Breath Biomarkers, Spectral Fingerprints, and Detection Limits. *Sensors* **2009,** *9*, 8230-8262.

232. Lee, J.; Sorescu, D. C.; Deng, X., Electron-induced dissociation of CO_2 on TiO_2(110). *J. Am. Chem. Soc.* **2011,** *133*, 10066-10069.

233. Ding, M.; Star, A., Synthesis of One-Dimensional SiC Nanostructures from a Glassy Buckypaper. *ACS Appl. Mater. Interfaces* **2013,** *5*, 1928-1936.

234. Wright, N. G.; Horsfall, A. B.; Vassilevski, K., Prospects for SiC electronics and sensors. *Mater. Today* **2008,** *11*, 16-21.

235. Wei, L.; Charles, M. L., Semiconductor nanowires. *J. Phys. D: Appl. Phys.* **2006,** *39*, R387.

236. Zekentes, K.; Rogdakis, K., SiC nanowires: material and devices. *J. Phys. D: Appl. Phys.* **2011,** *44*, 133001.

237. Zhou, W. M.; Fang, F.; Hou, Z. Y.; Yan, L. J.; Zhang, Y. F., Field-effect transistor based on β-SiC nanowire. *IEEE Electron Device Lett.* **2006,** *27*, 463-465.

238. Li, G.-Y.; Li, X.-D.; Wang, H.; Liu, L., Long SiC nanowires synthesized from off-gases of the polycarbosilane-derived SiC preparation. *Appl. Phys. A* **2010,** *98*, 293-298.

239. Li, Z.; Zhang, J.; Meng, A.; Guo, J., Large-Area Highly-Oriented SiC Nanowire Arrays: Synthesis, Raman, and Photoluminescence Properties. *J. Phys. Chem. B* **2006,** *110*, 22382-22386.

240. Niu, J. J.; Wang, J. N.; Xu, Q. F., Aligned Silicon Carbide Nanowire Crossed Nets with High Superhydrophobicity. *Langmuir* **2008,** *24*, 6918-6923.

241. Xie, Z.; Tao, D.; Wang, J., Synthesis of Silicon Carbide Nanotubes by Chemical Vapor Deposition. *J. Nanosci. Nanotechnol.* **2007,** *7*, 647-652.

242. Young Kim, H.; Park, J.; Yang, H., Direct synthesis of aligned silicon carbide nanowires from the silicon substrates. *Chem. Commun.* **2003,** *0*, 256-257.

243. Li, Y. B.; Xie, S. S.; Zou, X. P.; Tang, D. S.; Liu, Z. Q.; Zhou, W. Y.; Wang, G., Large-scale synthesis of β-SiC nanorods in the arc-discharge. *J. Cryst. Growth* **2001,** *223*, 125-128.

244. Seeger, T.; Kohler-Redlich, P.; Rühle, M., Synthesis of Nanometer-Sized SiC Whiskers in the Arc-Discharge. *Adv. Mater.* **2000,** *12*, 279-282.

245. Zhang, X.; Chen, Y.; Xie, Z.; Yang, W., Shape and Doping Enhanced Field Emission Properties of Quasialigned 3C-SiC Nanowires. *J. Phys. Chem. C* **2010,** *114*, 8251-8255.

246. Wang, H.; Lin, L.; Yang, W.; Xie, Z.; An, L., Preferred Orientation of SiC Nanowires Induced by Substrates. *J. Phys. Chem. C* **2010,** *114*, 2591-2594.

247. Wu, R.; Yang, G.; Gao, M.; Li, B.; Chen, J.; Zhai, R.; Pan, Y., Growth of SiC Nanowires from NiSi Solution. *Cryst. Growth Des.* **2008,** *9*, 100-104.

248. Gundiah, G.; Madhav, G. V.; Govindaraj, A.; Seikh, M. M.; Rao, C. N. R., Synthesis and characterization of silicon carbide, silicon oxynitride and silicon nitride nanowires. *J. Mater. Chem.* **2002,** *12*, 1606-1611.

249. Yang, Z.; Xia, Y.; Mokaya, R., High Surface Area Silicon Carbide Whiskers and Nanotubes Nanocast Using Mesoporous Silica. *Chem. Mater.* **2004,** *16*, 3877-3884.

250. Yang, Y.; Meng, G.; Liu, X.; Zhang, L.; Hu, Z.; He, C.; Hu, Y., Aligned SiC Porous Nanowire Arrays with Excellent Field Emission Properties Converted from Si Nanowires on Silicon Wafer. *J. Phys. Chem. C* **2008,** *112*, 20126-20130.

251. Ye, H.; Titchenal, N.; Gogotsi, Y.; Ko, F., SiC Nanowires Synthesized from Electrospun Nanofiber Templates. *Adv. Mater.* **2005,** *17*, 1531-1535.

252. Zhou, W.; Liu, X.; Zhang, Y., Simple approach to beta-SiC nanowires: Synthesis, optical, and electrical properties. *Appl. Phys. Lett.* **2006,** *89*, 223124-3.

253. Zhou, W.; Yan, L.; Wang, Y.; Zhang, Y., SiC nanowires: A photocatalytic nanomaterial. *Appl. Phys. Lett.* **2006,** *89*, 013105-3.

254. Dai, H.; Wong, E. W.; Lu, Y. Z.; Fan, S.; Lieber, C. M., Synthesis and characterization of carbide nanorods. *Nature* **1995,** *375*, 769-772.

255. Liu, J. W.; Zhong, D. Y.; Xie, F. Q.; Sun, M.; Wang, E. G.; Liu, W. X., Synthesis of SiC nanofibers by annealing carbon nanotubes covered with Si. *Chem. Phys. Lett.* **2001,** *348*, 357-360.

256. Pan, Z.; Lai, H. L.; Au, F. C. K.; Duan, X.; Zhou, W.; Shi, W.; Wang, N.; Lee, C. S.; Wong, N. B.; Lee, S. T.; Xie, S., Oriented Silicon Carbide Nanowires: Synthesis and Field Emission Properties. *Adv. Mater.* **2000,** *12*, 1186-1190.

257. Pham-Huu, C.; Keller, N.; Ehret, G.; Ledoux, M. J., The First Preparation of Silicon Carbide Nanotubes by Shape Memory Synthesis and Their Catalytic Potential. *J. Catal.* **2001,** *200*, 400-410.

258. Sun, X.-H.; Li, C.-P.; Wong, W.-K.; Wong, N.-B.; Lee, C.-S.; Lee, S.-T.; Teo, B.-K., Formation of Silicon Carbide Nanotubes and Nanowires via Reaction of Silicon (from Disproportionation of Silicon Monoxide) with Carbon Nanotubes. *J. Am. Chem. Soc.* **2002,** *124*, 14464-14471.

259. Taguchi, T.; Igawa, N.; Yamamoto, H.; Jitsukawa, S., Synthesis of Silicon Carbide Nanotubes. *J. Am. Ceram. Soc.* **2005,** *88*, 459-461.

260. Mendybaev, R. A.; Beckett, J. R.; Grossman, L.; Stolper, E.; Cooper, R. F.; Bradley, J. P., Volatilization kinetics of silicon carbide in reducing gases: an experimental study with applications to the survival of presolar grains in the solar nebula. *Geochim. Cosmochim. Acta* **2002,** *66*, 661-682.

261. Chen, J.; Tang, W.; Xin, L.; Shi, Q., Band gap characterization and photoluminescence properties of SiC nanowires. *Appl. Phys. A* **2011,** *102*, 213-217.

262. Bechelany, M.; Brioude, A.; Cornu, D.; Ferro, G.; Miele, P., A Raman Spectroscopy Study of Individual SiC Nanowires. *Adv. Funct. Mater.* **2007,** *17*, 939-943.

263. Zhang, Y.; Han, X.; Zheng, K.; Zhang, Z.; Zhang, X.; Fu, J.; Ji, Y.; Hao, Y.; Guo, X.; Wang, Z. L., Direct Observation of Super-Plasticity of Beta-SiC Nanowires at Low Temperature. *Adv. Funct. Mater.* **2007,** *17*, 3435-3440.

264. Li, G.-y.; Li, X.-d.; Chen, Z.-d.; Wang, J.; Wang, H.; Che, R.-c., Large Areas of Centimeters-Long SiC Nanowires Synthesized by Pyrolysis of a Polymer Precursor by a CVD Route. *J. Phys. Chem. C* **2009,** *113*, 17655-17660.

265. Lee, K. M.; Choi, T. Y.; Lee, S. K.; Poulikakos, D., Focused ion beam-assisted manipulation of single and double β-SiC nanowires and their thermal conductivity measurements by the four-point-probe 3-ω method. *Nanotechnology* **2010,** *21*, 125301.

266. Seong, H.-K.; Choi, H.-J.; Lee, S.-K.; Lee, J.-I.; Choi, D.-J., Optical and electrical transport properties in silicon carbide nanowires. *Appl. Phys. Lett.* **2004,** *85*, 1256-1258.

267. Chen, Y.; Zhang, X.; Zhao, Q.; He, L.; Huang, C.; Xie, Z., P-type 3C-SiC nanowires and their optical and electrical transport properties. *Chem. Commun.* **2011,** *47*, 6398-6400.

268. Song, B.; Chen, X. L.; Han, J. C.; Jian, J. K.; Bao, H. Q.; Li, H.; Zhu, K. X.; Wang, W. Y.; Wang, G.; Zuo, H. B.; Zhang, X. H.; Meng, S. H., Structural and magnetic properties of (Al, Fe)-codoped SiC. *J. Phys. D: Appl. Phys.* **2010,** *43*, 415002.